

EXPERIMENTAL STUDY OF MICRO-VORTEX GENERATORS
AT MACH 2.5

by
ADAM J PIERCE

Presented to the Faculty of the Graduate School of
The University of Texas at Arlington in Partial Fulfillment
of the Requirements
for the Degree of

MASTER OF SCIENCE IN AEROSPACE ENGINEERING

THE UNIVERSITY OF TEXAS AT ARLINGTON

December 2010

Copyright © by ADAM J PIERCE 2010

All Rights Reserved

ACKNOWLEDGEMENTS

For the time that I have spent working at the ARC I have had the pleasure of meeting and working with many respectable individuals and have come to appreciate the necessity for conducting experimental research. I will first like to thank Dr. Frank Lu for giving me the opportunity to expand my knowledge and my abilities as an aerospace engineer. I would also like to thank Dr. Don Wilson for sharing his vast practical experiences. I would like to thank Richard Mitchell, Daniel Bryant, Yusi Shih, Jeiny Gutierrez, David Whaley, and Perla Gonzalez for their help in assisting me in completing the task required for this project. I would like to thank Rod Duke for showing me that conducting aerodynamic research is not just about understanding aerodynamics, but includes the understanding of materials and practical design. Finally, I would like to thank my family and to the Lord for giving me the support as I pursue a level of understanding that only few in my family have ever achieved. They have never failed me even during my most difficult times. Thank you. Thank you all.

November 19, 2010

ABSTRACT

EXPERIMENTAL STUDY OF MICRO-VORTEX GENERATORS AT MACH 2.5

ADAM J PIERCE, M.S.

The University of Texas at Arlington, 2010

Supervising Professor: Frank K Lu

Vortex generators are geometrical shapes that produce trailing vortices and are widely used for their ability to improve the flow quality over areas where flow separation may occur. Current topics involve utilizing the performance capabilities of vortex generators to influence the boundary layer under supersonic conditions. Such influence may provide an alternative means of reducing boundary layer flow separation and improving the overall quality of the flow in the boundary layer. It would also maintain low drag in supersonic inlets and reduce the need for mechanical equipment used for boundary layer bleed leading to a reduction in aircraft weight and an overall increase in aircraft performance.

This study reports the results of experimental tests conducted using of micro-vortex generators on a flat plate at Mach 2.5. Qualitative analysis was performed using surface flow test and schlieren imagery. These results were compared with LES [1] results produced by the Department of Mathematics for code verification. Quantitative boundary layer analysis was conducted using particle image velocimetry

and the results agree well with theory. The results of this study conclude that micro-vortex generators influence the boundary in both thickness and overall flow structure.

The work conducted in this study was funded by AFOSR Grant No. FA9550-08-1-0201.

TABLE OF CONTENTS

ACKNOWLEDGEMENTS	iii
ABSTRACT	iv
LIST OF FIGURES	ix
LIST OF TABLES	xii
Chapter	Page
1. INTRODUCTION	1
2. LITERATURE REVIEW	4
3. EXPERIMENTAL SETUP	9
3.1 Supersonic Wind Tunnel	10
3.1.1 SSWT Pressure Monitoring	10
3.1.2 Temperature Device	12
3.1.3 Dewpoint Meter	14
3.1.4 Fisher Control Valve	15
3.1.5 Test Section	16
3.1.6 Labview SSWT Controller	18
3.2 Micro Vortex Generator Design	18
3.3 Surface Flow Visualization	19
3.3.1 Equipment	20
3.3.2 Surface Flow Paint	20
3.3.3 Application	22
3.3.4 Preparations	23
3.4 Particle Image Velocimetry	25

3.4.1	Equipment	25
3.4.2	PIV Calibration	27
3.4.3	Seeding	30
3.4.4	Seeding Apparatus	32
3.4.5	Boundary Layer Seeding	35
3.4.6	Surface Reflection	36
3.4.7	Preparations	38
3.5	Boundary Layer Analysis	38
3.5.1	PIV Vector Pre-Processing	39
3.5.2	PIV Post-Vector Processing	40
3.5.3	Turbulent Compressible Boundary Layer Calculations	41
3.6	Schlieren Imaging	48
3.6.1	System Setup	48
3.6.2	Preparations	51
4.	RESULTS AND DISCUSSION	53
4.1	Surface Flow Visualization	53
4.1.1	Qualitative Results	54
4.2	Particle Image Velocimetry	72
4.2.1	Acetone Seeding	72
4.2.2	Flat Plate	73
4.3	5 Degree Ramp	75
4.4	Schlieren Imaging	80
4.4.1	Flat Plate	83
4.4.2	5 Degree Ramp	84
5.	CONCLUSION	86

Appendix

A. PIV AND SCHLIEREN RESULTS	88
B. VALVE CONTROLLER PROGRAM	101
REFERENCES	123
BIOGRAPHICAL STATEMENT	130

LIST OF FIGURES

Figure	Page
1.1 Trailing vortex generated by the aircrafts wingtips [2]	2
2.1 Vortex generator profile described by Holden and Babinsky [3]	5
2.2 Surface contour lines of MVG45 [1]	7
2.3 3-D LES results revealing vortex ring structures	8
3.1 Supersonic Windtunnel (SSWT) at the ARC	11
3.2 260 Ω resistor used for thermocouple transmitter	13
3.3 SSWT dewpoint meter	14
3.4 SSWT control valve	15
3.5 SSWT Test section design:(a)Pro-Engineering mode (b) Completed test section	17
3.6 Micro-Vortex Generator design (a)MVG45 (b) MVG70	19
3.7 CAD MVG plate section model (a) MVG45 (b) MVG70	20
3.8 Surface flow paint applicator for surface flow testing	23
3.9 Photograph of test section results with mounted UV lights	23
3.10 Typical PIV setup configuration[4]	25
3.11 PIV setup for study	26
3.12 Type 20 Calibration plate for PIV	28
3.13 Dot search results for PIV calibration (a) Camera1 (b) Camera 2 (c) Calibrated	29
3.14 Calibration data for (a) camera 1 (b) and camera 2	30
3.15 Pro-E drawing of SSWT Seeder apparatus.	33
3.16 Seeder delivery system located inside plenum chamber	34

3.17	Seeder modification for LabVIEW control (a) Seeder solenoid valve (b) Seeder solid-state relay	35
3.18	The turbulent boundary layer in law-of-the-wall coordinates	42
3.19	Example graph of test data.	43
4.1	Surface streamlines of MVG45 from LES (a) Angled view (b) Vertical view	54
4.2	Surface flow results of <i>Flat Plate No MVG</i> taken from (a) Canon (b) Nikon	55
4.3	Surface flow results of <i>Flat Plate MVG 45</i> (a) Close view (b) Downstream view	56
4.4	Surface flow results of <i>Flat Plate MVG 70</i> (a)Close view (b) Downstream view	58
4.5	Surface flow characteristics results (a) LES, (b) Experimental	59
4.6	Surface Flow test results of <i>5 Degree No MVG</i> (a) Ramp view (b) Plate view	60
4.7	Surface flow test results of <i>5 Degree 45 MVG</i> (a) Near view (b) Downstream view	61
4.8	Surface flow test results of <i>5 Degree 70 MVG</i> (a) Near view (b) Downstream view	62
4.9	Surface flow test results of <i>25 Degree No MVG</i> (a) Top view (b) Side view	63
4.10	Surface flow test results of <i>25 Degree 45 MVG</i> (a) Near view (b) Downstream view	64
4.11	Surface flow test results of <i>Cyl No MVG</i> (a) Top view (b) Downstream view	65
4.12	Surface flow test results of <i>Cyl 45 MVG</i> (a) Near view (b) Downstream view	66
4.13	Surface flow test results of <i>Cyl 70 MVG</i> (a) Near view (b) Downstream view	67
4.14	MVG 70 surface flow results (a) LES (b) Experimental	68
4.15	MVG70 Top Comparision results (a) LES (b) Experimental	68

4.16	Image result after manipulation by the DaVis software (a) Raw image (b) Manipulated	69
4.17	Top view comparison of MVG45 (a) LES (b) Raw (c) Manipulated . .	70
4.18	Complete top view of manipulated image for MVG45	70
4.19	Top view comparison of (a) LES (b) Raw (c) Manipulated	71
4.20	Complete top view of manipulated image for MVG70	71
4.21	Boundary layer visualization with (a) Calcium carbonate, (b) Acetone	73
4.22	Turbulent boundary layer profile for <i>No Ramp No MVG</i> configuration	74
4.23	Turbulent boundary layer profile for <i>No Ramp MVG 45</i> configuration	76
4.24	Turbulent boundary layer profile for <i>No Ramp 70 MVG</i> configuration	76
4.25	Turbulent boundary layer profile for <i>5 Degree Ramp No MVG</i> configuration	77
4.26	Turbulent boundary layer profile for the <i>5 Degree Ramp 45 MVG</i> configuration	78
4.27	Turbulent boundary layer profile for the <i>5 Degree Ramp 70 MVG</i> configuration	79
4.28	Typical results for image subtraction using DaVis 7.1 (a) Schlieren (b) Image subtraction	82
4.29	Results of the measure Mach angle	83

LIST OF TABLES

Table	Page
3.1 Pressure transducer data voltage-to-pressure calibrations	12
3.2 Steel mesh screen data	21
3.3 Density of some common seed materials used for seeding	31
3.4 Particle relaxation time of some commonly used seed particles	32
4.1 Surface Flow Test Schedule	53
4.2 PIV Test Schedule	72
4.3 Calculation Results for <i>Flat Plate No MVG</i>	75
4.4 Calculation Results for <i>Flat Plate 45 MVG</i>	75
4.5 Calculation Results for <i>Flat Plate 70 MVG</i>	77
4.6 Calculation Results for <i>5 Deg No MVG</i>	78
4.7 Calculation Results for the <i>5 Deg 45 MVG</i> configuration.	79
4.8 Calculation Results for the <i>5 Deg 70 MVG</i> configuration.	79
4.9 Schlieren Test Schedule	81

CHAPTER 1

INTRODUCTION

A vortex is defined as a region within a body of fluid in which the fluid elements have an angular velocity[5]. The most commonly recognized example of vortex flow is a tornado. The air moves with an angular velocity about a center. In aviation, a vortex is commonly recognized by the conditions that are produced by the wingtips of an aircraft. Aircraft wingtip vortices are considered the most dangerous component of the wake turbulence. Wingtip vortices are produced due to the pressure differential needed to create lift. At the wing tip, the high pressure air underneath the wing spills over the wing tip and to the area of low pressure on top of the wing. Because the aircraft is in motion, a trailing vortex is produced. If the trailing vortex is strong enough, the effects on for following aircraft can be catastrophic. Fig. 1.1 shows the trailing vortices produced by an aircraft's wingtips.

In some cases a trailing vortex is generated on purpose. Geometrical shapes that produce these trailing vortices are called vortex generators. The most common type of vortex generators are those mounted on wings to improve the flow quality. Many designs of vortex generators exist and their concept is simple; extract high momentum flow from the freestream and energize the low-momentum flow near the surface. Vortex generators have been used to enhance wing lift on aircraft, reducing drag on aircraft fuselage, delay or avoid flow separations in subsonic diffuser, and eliminate or reduce boundary layer flow separation [1].

The boundary layer is a region close to the surface where the viscous forces become important [6]. Flow separation that occurs within the boundary layer can



Figure 1.1. Trailing vortex generated by the aircrafts wingtips [2].

increase the drag and reduce the overall quality of the flow. Conventional vortex generators are typically designed with a height that extends just beyond the boundary layer thickness and are positioned at a small angle with respect to the direction of travel in order to divert the higher momentum flow. A drag penalty is a consequence of using vortex generators. However, the overall drag penalty is not enough to offset the performance gained using vortex generators. By applying conventional techniques and understanding, there may exist a solution of reducing the drag penalty while maintaining the increase in overall performance. This understanding has led to the development of sub-boundary layer vortex generators (SBVG) also commonly known as micro-vortex generators (MVGs).

The present study focuses on the use of MVGs and on the effectiveness of the production of trailing vortices at a freestream Mach number of 2.5. Like regular vortex generators, MVGs have many designs. Some common designs of MVGs are vane-type, active, passive, and ramp-type just to name a few. The current study focus on two vortex generators designed by Dr. Qin Li from the Mathematics Department at the University of Texas at Arlington. The research conducted here is part of a jointed project between the Mathematics and the Mechanical and Aerospace Departments

and is sponsored by the Air Force Office of Science Research (AFOSR). This project is two fold. First, large eddy simulation (LES) of using one MVG is conducted by the Mathematics Department and studied. Second, experiments are performed by the Mechanical and Aerospace Department to verify and study the effects of MVGs. The LES results are used here as part of the qualitative analysis. Experimental testing and analysis for this study involve qualitative surface visualization, boundary layer analysis using particle image velocimetry, and qualitative verification using schlieren imagery. Before details of the test and results are given, a review on the subject of MVGs and previous research conducted is performed.

CHAPTER 2

LITERATURE REVIEW

To gain a better understanding of the effects and application of MVGs in supersonic flow as well as the basic method for turbulent boundary layer analysis, a brief literature review was performed. Understanding experiments previously conducted will help to provide information on what results and characteristics that can be expected from using MVGs.

The most influential literature involving turbulent boundary layer analysis was a report by the NATO Advisory Group for Aerospace Research and Development (AGARD) Report Number 335 [7]. This report is an in-depth review of turbulent boundary layers analysis for subsonic and supersonic flows.

A report conducted by Mabey [8] include data and results needed to verify calculations and the boundary layer analysis code developed for this study.

The current literature generally involves studying MVG effects on shock boundary layer interaction (SBLI). One such investigation conducted by Holden and Babin-sky involved the effects of MVGs on a normal shock boundary layer interaction [3]. Holden investigated two MVGs designed by Ashill to determine whether wedge-shaped MVGs or vane-type MVGs induce a shock weakening effect. Fig. 2.1 shows the vortex generators tested along the depicted vortex structure for each case. The experiments were conducted in a wind tunnel at a freestream Mach number of 1.5. The normal shock boundary layer interaction was investigated at $x = 0$ mm and $x = -36$ mm with $x = 0$ mm defined as the center in streamwise direction. The incoming boundary layer was 5.7 mm.

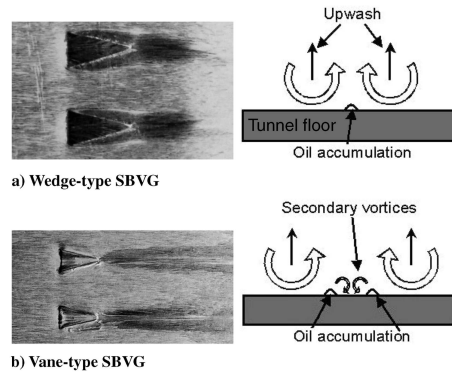


Figure 2.1. Vortex generator profile described by Holden and Babinsky [3].

These authors concluded that the MVGs have no effect when located directly under the normal shock. When the normal shocks travel downstream of the MVGs, a shock-reexpansion-shock developed over the devices indicating an increase in wave drag [3]. The results also concluded that vane-type MVGs performed better than the wedge-type MVGs. The vane-type MVGs appear to eliminate shock-induced separation while the wedge-type only reduce it. This could indicate that the shape of the MVG can influence the strength of the vortex being generated.

The study by Valdivia examined the effects of Wheeler doublets, vortex generator Jets (VGJ), and the combination of both on inlet unstart condition at Mach 5 [9]. The height of the VGJ devices was approximately 2.54 mm and were tested in both passive and active modes using compressed air. The boundary layer thickness was measured to be 19.3 mm. The doublets and vortex generators were mounted in a two row configuration on the side wall of the test inlet located 83.9 mm and 92 mm from the leading edge of the test nozzle. Under the active mode, the VGJs injected air in order to energize the boundary layer with the intention of reducing or preventing unstart conditions.

To induce unstart conditions an adjustable ramp was mounted at the exit. The position of the ramp at different angles either reduced or increased the mass flow

through the inlet test nozzle. Upon reaching a certain angle an unstart condition was initiated. A baseline test without using Wheeler doublets or VGJ's was performed indicating a ramp angle of 49.6° initiated unstart conditions.

The results the study concluded that neither the Wheeler doublets, VFJs, or the combination of the two was able to prevent an unstart from occurring emphasizing the intense strength of the unstart condition. This also reveals the overall weak effect of vortex generators when compared to this condition. Theirs result found that when VGJs where in active mode the back pressure increased by 17.8% with a lower ramp angle of 48.3° . The study also found that the combination of Wheeler doublets and VGJs yielded a total backpressure increase of 31.5% at a ramp angle of 48.3° indicating that the ramjet mode can be sustained under the same ramp angle as the baseline, but with a higher back pressure. Once the vortex jets were turned off, the inlet became unstarted. This would support the conclusion that vortex generators have a significant influence on the flow properties in the boundary layer. Whether these are a direct result of the generated vortex or the injection of mass flow is unclear.

Having the ability to optimize MVGs under different design conditions is very important. A study by Anderson et al develops a methodology for optimization of micro ramp arrays. The objective of the study was to determine the optimal micro-ramp design for controlling SBLI in supersonic inlets and compare the results to conventional bleeding methods. A CFD analysis involving three different types of MVGs was performed. The three types of MVGs include micro-ramps, tapered micro-vanes, and micro-vane with no taper. The analysis was performed at a freestream Mach number of 2.0.

The study concluded that MVGs are capable of managing the SBLI within an inlet and determined design parameters based on the boundary layer thickness and the shock wave impingement point. The design optimization include the micro-actuator

chord length, spacing distance between MVGs, and MVG height. The MVGs led to a 10% reduction in inlet size and reducing the overall inlet drag. However, the effects of the MVG on the boundary layer thickness would require an internal enlargement of the inlet to compensate for the increase in boundary layer thickness. Anderson et al results also concluded the MVGs dramatically affected the properties within the boundary layer under supersonic conditions.

For the present study, the paper by Dr Qin Li [1] is the most important. The conditions of the simulations conducted represent near similar conditions as the present experiments with a few exceptions. For LES, higher Reynolds number requires large computing resources. Therefore the LES results will somewhat differ due to the lower $Re_\theta = 1440$ compare to the experimental values of 8000–10000.

The LES found that MVGs significantly reduced the separation zone located at the ramp. Surface streamlines reveal flow characteristics such as leading edge separation, horseshoe vortices, possible vortex filaments, and vortex rings. The of leading edge separation and the horseshoe vortices are structures that have been repeated elsewhere. Flow characteristics that have not been reported include the possible existence of vortex filaments indicated by the swirl marks located on the

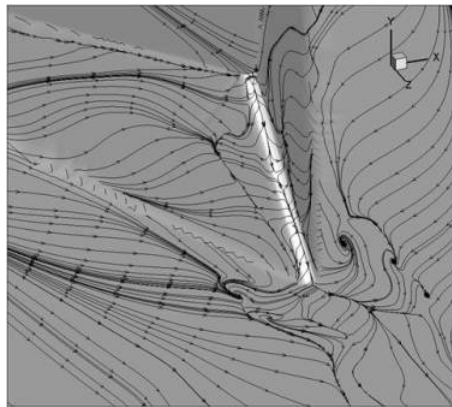


Figure 2.2. Surface contour lines of MVG45 [1].

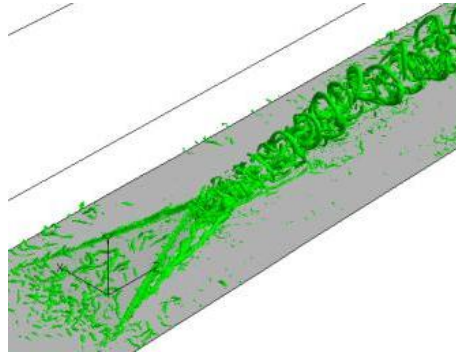


Figure 2.3. 3-D LES results revealing vortex ring structures.

each side of the ramp seen in Fig. 2.2. The existence of vortex rings is also previously reported.

The vortex rings seen in Fig. 2.3 appear to be stable structures starting at approximately one MVG downstream. Experimentally, it may be difficult to capture these rings without the use of high-speed cameras, but capturing or identifying the existence of these vortex ring structures would be significant in understanding the flow characteristics of MVGs.

CHAPTER 3

EXPERIMENTAL SETUP

This experimental study was conducted at the Aerodynamics Research Center (ARC) at the University of Texas at Arlington. The ARC houses a low-speed, a transonic, a supersonic and a hypersonic wind tunnel, as well as an arc heater. The facility was constructed in 1986. The ARC's primary purpose is to conduct experimental research and education in aerodynamics and propulsion. To support the test facilities, the ARC has a 5-stage Clark Model No. CMB-6 compressor capable of compressing air to 20.6 MPa (3000 psig) but was derated to 13.8 MPa (2000 psig) to match the rating of the storage tanks. Compressed air from the compressor can be directed to all of the facilities in the ARC.

Three different types of tests were performed in this study. These tests include surface flow visualization, PIV, and schlieren imagery. Each test was applied to six configurations. The configurations include a flat plate with MVG45, flat plate with MVG70, flat plate without vortex generators, 5-deg ramp with MVG45, 5-deg ramp with MVG70, and 5-deg ramp without MVG.¹ Two additional configurations were tested using the surface flow technique, namely, a 25-deg ramp with and without micro vortex generators, and a cylinder with and without micro vortex generators. The results of these configurations are given in Chapter 4.

¹The notation MVG45 and MVG70 stands for micro vortex generators with a 45 or a 70 deg trailing edge.

3.1 Supersonic Wind Tunnel

The supersonic wind tunnel (SSWT) is a blowdown-type wind tunnel capable of testing from Mach 1.5 to Mach 4, a Reynolds number of approximately 50–100 million/m [10] and is capable of run times in excess of 1 minute at a maximum storage pressure of 5.17 MPa (750 psig). The SSWT includes a steel pipe with a diameter of 292 mm (11.5 in) and a length of 26.8 m (88 ft). This pipe connects the wind tunnel to two supply tanks that hold approximately 24.45 m³ (863.44 ft³) of compressed air. This large storage capacity gives the operator the option to perform multiple short runs or one long run on a given charge. Due to safety considerations and the desired experimental run times for this study, it was not recommended to operate at the maximum allowable pressure unless the long-duration run time was required. Connected downstream of the supply tanks and the pipe is a 152 mm (6 in.) diameter Velan Model F2064C02Ty-600RF manual gate valve and a Fisher V200-DVC5020 ball-type pneumatic control valve. The manual gate valve is normally closed when wind tunnel operations are not being performed. The Fisher V200 pneumatic control valve is the primary valve for regulating air flow from the supply tanks to the plenum chamber. Downstream of the pneumatic control valve is a 610 mm (24 in.) diameter plenum chamber, the wind tunnel nozzle, test section, and diffuser which are shown in Fig. 3.1. The SSWT is controlled remotely by computer located in the control room.

3.1.1 SSWT Pressure Monitoring

The SSWT is monitored by three pressure transducers. Each pressure transducer is assigned a designated name according to its location on the wind tunnel. The first pressure transducer is an Omega model PX613-1KG5V pressure transducer capable of measuring pressures up to 6.9 MPa (1000 psig). It is located upstream from



Figure 3.1. Supersonic Windtunnel (SSWT) at the ARC.

the pneumatic control valve on the supply side and is designated as P_1 . The second pressure transducer is an Omega model PX613-500G5V and is rated for pressures up to 2 MPa (300 psig). This pressure transducer is mounted on the plenum chamber downstream from the pneumatic control valve and just upstream of the throat and is designated as P_2 . The plenum pressure is the most important parameter for controlling the wind tunnel during operation. The Valve Controller program monitors the readings from P_2 and adjusts the valve angle on the pneumatic valve in order to maintain the desired plenum chamber pressure. Good performance of the P_2 transducer is necessary to ensure that the wind tunnel performance is satisfactorily and safe. The third pressure transducer is an Omega model PX613-100G5V is located at the entrance of the test section which is also the exit of the nozzle and is designated as P_3 . This pressure transducer is necessary for verifying wind tunnel conditions as well as for verifying nozzle exit conditions. Each pressure transducer generates a voltage signal and sends this signal to the Valve Controller program. The incoming

Table 3.1. Pressure transducer data voltage-to-pressure calibrations

Model	Usage	Pressure Range	Output Range	Linearity	Zero Offset	Accuracy	\pm Error
PX-613 1KG	P_1	0–6.994MPa (0–1000 psig)	1–5 V	1.0008	–26.951 kPa (–3.9094 psi)	0.31%	42.81 kPa (6.21 psi)
PX-613 300G	P_2	0–2.169 MPa (0–300 psig)	1–5 V	1.0014	–8.0881 kPa (–1.1735 psi)	0.23%	1.76 kPa (0.25 psi)
PX-613 100G	P_3	0–790.6 kPa (0–100 psig)	1–5 V	1.0015	–2.2091 kPa (–0.3206 psi)	0.13%	0.71 kPa (0.10 psi)

voltage signal is then converted into a pressure using a voltage-to-pressure equation. This equation is normally derived by the manufacturer and is presented to the user in the form of a certificate. The original certificates have, unfortunately, been misplaced. However, these pressure transducers are the same pressure transducers used previously [10]. Therefore, these voltage-to-pressure equations can be utilized for the current study. The general equation for converting voltage to pressure is given by Eq.(3.1). The data required is listed in Table 3.1.

$$\text{Calibrated Pressure} = (\text{Linearity}) \cdot \frac{\text{Pressure Range}}{\text{Output Range}} \cdot (\text{Output}) + \text{Zero Offset} \quad (3.1)$$

3.1.2 Temperature Device

An Omega type T thermocouple, with a temperature range of -160 to $400 \pm 0.5^\circ\text{C}$ is mounted in the plenum chamber near the P_2 pressure transducer. The thermocouple monitors the air temperature in the plenum chamber. For data analysis this value can be considered as the total temperature. A recent upgrade to the thermocouple's configuration allows the device to transmit a signal to the control room over a distance of approximately 30.5 m (100 ft). The previous configuration used two 9 V batteries to boost the thermocouple signal. This configuration is not reliable for long term usage as the batteries needed constant replacement. An Omega

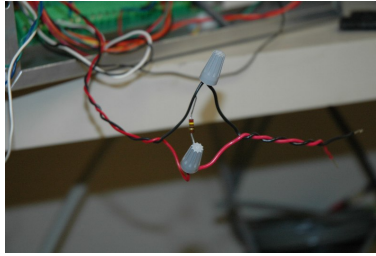


Figure 3.2. 260 Ω resistor used for thermocouple transmitter.

model TX250 transmitter was purchased to improve long-term functional capabilities. The transmitter converts the voltage signal from the thermocouple and sends out a 4-20 mA dc signal. This signal is then transmitted to the Valve Controller program. The data acquisition (DAQ) card located on the computer is incapable of reading a 4-20 mA dc signal. The operating manual suggests that the signal be converted back to voltage by using a resistor. Therefore, a 260 Ω resistor was mounted in parallel with the data acquisition system to convert the 4–20 mA dc signal to a voltage signal in the range of 0.1 to 5.2 V, shown in Fig. 3.2.

Like the pressure transducers, the thermocouple transmitter requires calibration and conversion from voltage to temperature. While the facility is capable of performing such a calibration, it was decided that it would be both efficient and reliable to have the manufacturer calibrate the transmitter for a small fee. The transmitter was calibrated for a temperature range of -100 to 100 $^{\circ}\text{C}$. With the known voltage signal, a simple linear equation can be produced to convert the voltage to temperature and can be confirmed using multiple known reference temperatures. The results of the calibration led to Eqs.(3.2).

$$T_2 = 39.216V - 103.92 \quad (3.2)$$



Figure 3.3. SSWT dewpoint meter.

A simple experiment was performed where the room temperature was measured using a mercury-in-glass thermometer. For a room temperature of 16.7°C (62°F), the transmitter with a $250\ \Omega$ resistor produced a reading of $3.1\ \text{V}$. Using Eqs.(3.2) the resulting temperature is $17.65\ ^{\circ}\text{C}$ ($63\ ^{\circ}\text{F}$). This was considered to be within an expected range of error.

3.1.3 Dewpoint Meter

The SSWT uses a Vaisala DRYCAP Model DMT142 dewpoint transmitter to measure the dewpoint of the air supply. The dewpoint transmitter is located near the P_1 pressure transducer as seen in Fig. 3.3. It is connected to a $24\ \text{V}$ power supply and is turned off and on by a conventional relay switch. The dewpoint meter measures the dewpoint temperature and produces a $0\text{--}5\ \text{V}$ or a $2\text{--}20\ \text{mA}$ signal depending on the users desired wiring configuration. This particular dewpoint meter is wired to produce $0\text{--}5\ \text{V}$ and is calibrated for a dewpoint temperature range of -60 to 40°C . This voltage output is then transferred to the Valve Controller program which

converts it to a dewpoint temperature. According to the the data certificate supplied by the manufacturer, the voltage output is linear with the dewpoint temperature according to Eqs.(3.3).

$$T_d = 20V - 60 \quad (3.3)$$

Typical dewpoint readings were approximately $-30\text{ }^\circ\text{C}$ (-22°F), which is acceptable for supersonic wind tunnel testing. The dewpoint value depends on how long the air has remained in the storage tanks. It is noted that the dewpoint never reached a level that would result in excessive humidity for testing. Typical dewpoint measurements showed a rise by about $5\text{ }^\circ\text{C}$ (9°F) over 24–48 hours.

3.1.4 Fisher Control Valve

The SSWT utilizes a Fisher V200 ball valve mounted to a Fisher type 1052 actuator to regulate the pressure in the plenum chamber as seen in Fig. 3.4. The actuator is connected to a Fieldvue Type DVC 5020 controller. The controller controls



Figure 3.4. SSWT control valve.

the amount of air that is delivered to the diaphragm located on top of the valve. The diaphragm provides the means of converting a pressure force into a mechanical force which is used to rotate the ball valve. The Fieldvue controller is an independent Valve Controller with its own internal gain settings. The gain settings for the Fieldvue controller are not to be confused with gains that the operator inputs in the LabVIEW Valve Controller program. The control gains on the Fieldvue controller are adjusted using the Fieldvue software and a usb modem.

Using only the Fieldvue Controller was determined to be insufficient to control the air supplied to the diaphragm for the required response time needed for testing. Therefore a Fairchild Model 20 pneumatic high capacity volume booster was added to improve control valve response. The booster is configured for a 1:1 pressure ratio and receives a pneumatic pressure signal from the Fieldvue controller. The booster then delivers a larger volume of air to the diaphragm which rotated the ball valve at a faster rate.

3.1.5 Test Section

The SSWT test section is made of aluminum and designed by Richard Mitchell, a former UTA graduate student. A flat plate at zero angle of attack can be placed in the test section, see Fig. 3.5. The test section allowed windows to be mounted on three sides for optical access. The conceptual design of the test section was developed and modeled in Pro-Engineer. The test section was simulated in Fluent to ensure starting conditions with a flat plate and with a 5-deg ramp. The 25-deg ramp was not modeled at the time of development. The inside width and height of the test section is 152 mm \times 254 mm (6 in. \times 12 in.). The nozzle exit, i.e., entrance to the test section is 152 mm \times 152 mm (6 in. \times 6 in.).

The flat plate is mounted in the test section such that its leading edge sits in the middle of the nozzle exit. This leaves an area above the flat plate that is 76.2 mm

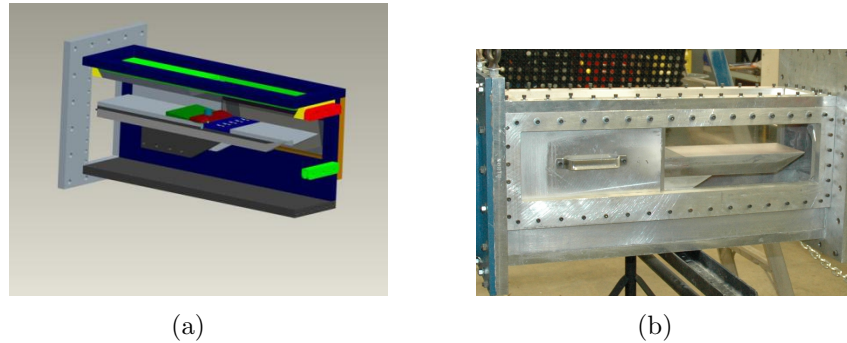


Figure 3.5. SSWT Test section design:(a)Pro-Engineering (b) Completed test section.

high by 152 mm wide (3 in. \times 6 in.). The alignment of the flat plate was set with respect to the nozzle using a digital angle. The flat plate is designed to be modular which allowed the different configurations to be tested in this study. Depending on the test and configuration, typical turnaround time for preparing the flat plate for the next test was approximately six hours.

A preparation cycle for the flat plate was developed. A typical test cycle began with dismantling of the SSWT test section. The first step was to remove the north side wall. The side walls held the optical and aluminum components shown in Fig. 3.5(b). The next step was to detach the diffuser from the test section by removing 18 nuts and bolts connecting the test section and the diffuser. Before the flat plate can be removed, steel tubing must be removed from the side wall entrance. Mounted with four bolts underneath and center of the flat plate is a thin piece of aluminum that covers the tubing. After removing the thin piece of aluminum, small steel tubing were exposed. On the south side of the test section, there is a port where a small steel tubing entered the test section. After removing the four bolts holding and the rubber adapter from its location, the steel tubes were removed from the rubber adapter. Once the steel tubes and the rubber adapter were separated, the steel tubes were pushed inside the test section. The flat plate was then removed from the test section.

To loosen the flat plate from the test section, eight 3/8–28 bolts located on the ramps legs had to be removed. Two pieces of 2×4 studs were placed under the flat plate legs to provide support and maintain stability. Once the eight bolts were removed, the plate was removed from the test section. To install the flat plate, the procedures just described were performed in reverse order.

3.1.6 Labview SSWT Controller

It is necessary for the wind tunnel to be precisely controlled. As is typical with blowdown tunnels, the control parameter for proper operation is the total pressure measured in the plenum chamber. Initially, the SSWT had a small storage capacity and a controller was purchase to be able to open the valve rapidly but without excessive oscillations [10]. In late 2005, with added capacity, a new LabVIEW-based controller was developed [11]. Unfortunately, the first version of the program proved not to be reliable for this study. This lead for a newly redesigned controller. A detailed description of the redesigned controller can be found in Appendix B.

3.2 Micro Vortex Generator Design

Two micro vortex generator (MVG) designed by Dr Li from the Mathematics Department were tested[1]. The first vortex generator design is designated as the MVG45. This design has a triangular platform with a leading-edge ramp angle of 8.6° and a height of 2 mm (0.079 in.). The designation MVG45 refers to the trailing angle which is inclined at 45° with respect to the horizontal surface. Fig. 3.6(a) is a Pro-Engineering image of MVG45.

The second vortex generator design is designated MVG70. MVG70 is identical in shape and configuration to the MVG45 with the exception of the trailing angle being 70° instead of 45° with respect to the horizontal surface. The leading-edge

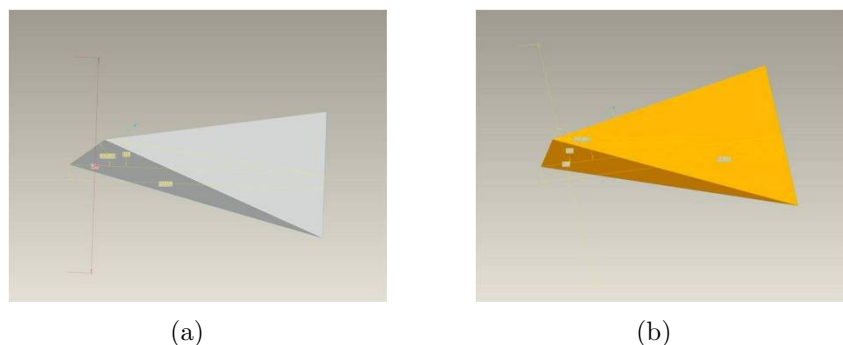


Figure 3.6. Micro-Vortex Generator design (a)MVG45 (b) MVG70.

ramp angle is also 8.6° with a height of 2 mm (0.079 in.) high. Fig. 3.6(b) shows a Pro-Engineering image of the MVG70.

Manufacturing individual MVG elements and then mounting them to the flat plate were determined to be unreliable due to concerns about the accuracy to properly mounting them in a given location and whether the MVGs could survive testing. The solution was to fabricate a flat plate insert with an MVG array. To ensure durability of the MVGs for multiple test, A-6 heat treated steel was used and a grinding techniques was applied. Other metals, such as aluminum, were considered to be too soft for this application. The spacing between the MVGs was limited by the thickness of the grinding wheel. The resulting MVG plate was an integral piece of heat treated A-6 steel 101.6 mm (l) \times 152 mm (w) \times 12.7 mm (t) (4 in. \times 6 in. \times 0.5 in.). A total of 5 vortex generators were placed equally spaced approximately 30.4 mm (1.2 in.) with respect to their center. The primary vortex was mounted 76.2 mm (3 in.) from the edge. CAD renditions of the MVG45 and MVG70 inserts are shown in Fig. 3.7.

3.3 Surface Flow Visualization

For supersonic testing, revealing complex flow features at the surface is extremely useful in providing guidance for subsequent detailed measurements. In order to collect such information, surface flow visualization tests must be performed. More-

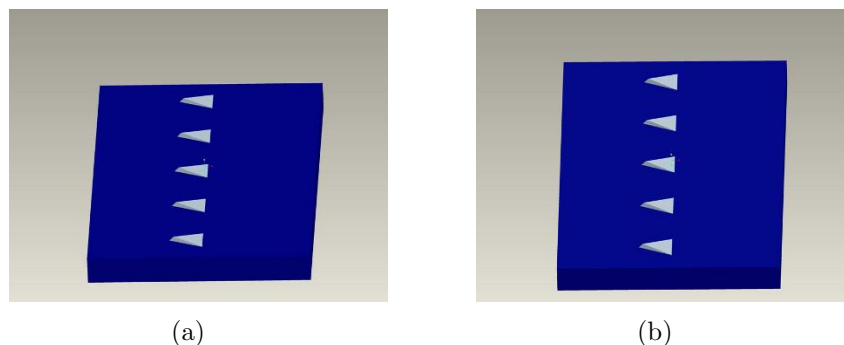


Figure 3.7. CAD MVG plate section model (a) MVG45 (b) MVG70.

over, the ability to identify surface features is in itself extremely valuable in developing and verifying CFD models of complex flows.

3.3.1 *Equipment*

A combination of still images and video data were taken using a Nikon D300s and a Canon Vixia HS-10 camera. Still images and video were captured using a Nikon D300s with a 12.1 Megapixel image capability and a video capability of 720p at 29 fps. For still images the Nikon D300S produce superior image quality compared to the Canon Vixia HS-10 HD and was used to focus on small features in specific areas. For a more general field of view, the Canon Vixia video camera was used. The Canon video camera has the capability to capture 1080i HD video at 29 fps at a lower 6 Megapixel. Both these cameras were mounted vertically looking down onto the surface of the flat plate.

3.3.2 *Surface Flow Paint*

To capture the surface flow with the greatest possible detail, specific requirements in paint characteristic were needed. One requirement is for the paint to perform well under supersonic conditions. The greatest concern is the paint's viscosity. If the viscosity is too low, the paint would simply be blown downstream. If the viscosity is too high, the paint will take a long time to attain the desired pattern which, in fact,

Table 3.2. Steel mesh screen data

Manufacturer	Model	Screen Size (in.)	Screen size (μm)
Tyler	3"-FH-SS-SS-US-40	0.0165	425
Tyler	3"-FH-SS-SS-US-70	0.0083	212
Tyler	3"-FH-SS-SS-US-140	0.0043	106

may not even form. Smearing can also be a problem during the shutdown process if the viscosity is too high. A second requirement for this study is the ability for the paint to be illuminated by UV lighting. The UV lighting would effectively produce greater detail about the surface flow. The final requirement is for the paint to be available in different colors. For most surface flow visualizations, one color may be sufficient. However, multiple colors have the advantage of revealing certain flow characteristics such as mixing and flow separations that may be difficult to view with one color.

The solution to the requirements of paint characteristics resulted in mixture of fluorescent chalk, kerosene and silicone oil [12]. Each of the ingredients serves a specific purpose. The fluorescent chalk fulfilled the requirement to be available in multiple colors and reveal surface flow characteristics with greater detail using UV lighting. In order to provide the greatest surface flow detail, the chalk was ground using a mortar and pestle. The resulting powder then was reduce to a particle size of $106 \mu\text{m}$ (0.0043 in.) using a series of small steel mesh filters listed in Table 3.2.

With the UV characteristics and fine particle size, the fluorescent chalk made an excellent choice for surface flow testing. The finely powdered fluorescent chalk was then mixed with small amounts of kerosene. The kerosene was mainly needed for its evaporation characteristics. During wind tunnel operations, the temperature in the test section decreased to approximately $-135 \text{ }^\circ\text{C}$ which slowed the evaporation of

the kerosene. However, the rate of evaporation appeared to increase rapidly when the wind tunnel was in the process of shutting down. The combination of the mixture and rapid increase of evaporation of the kerosene during shutdown left a paint solution sufficiently thin enough so as not to smear during shut down, thereby leaving an imprint of the surface flow under test conditions. However, it was found that the kerosene and chalk mixture alone was too thin for testing and the mixture would be completely evaporated after five seconds. If the chalk dried too quickly it would break off the surface before the tunnel could fully shut down. Silicone oil was added to the mixture to thicken the solution. Silicone oil does not evaporate as readily as kerosene. This addition ensured that the paint would not dry and break off during SSWT operation. Initial testing revealed that too much silicone oil would cause the mixture to smear when the wind tunnel was shutting down, giving a false impression of mixing and poor flow quality. It was later determined that the optimal consistency of the mixture closely resembled to the consistency of pancake syrup.

3.3.3 Application

Once the mixture and consistency were determined, combinations of blue, orange, yellow, green and red colors were determined to be the best selection for the testing. Blue and orange were chosen as the main colors because there was a large quantity of each readily available. Yellow and green were used for targeted areas of interest such as flow separation zones and corners. To apply the paint to the surface of the flat plate in a uniform fashion, an applicator made out of wooden stick, silicone tubing, and Teflon tubes was constructed, see Fig. 3.8. The device was designed such that rows would alternate in color. To further increase the color contrast of the fluorescent paint, the surface of the flat plate was painted matte black.

The test section required some minor modifications in order to install the required UV lights. Two Utilitech Model GU9721P-T8-BKI UV lights were mounted on

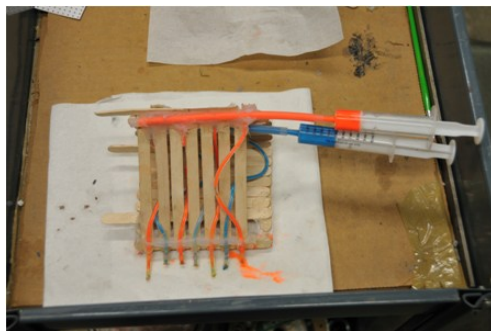


Figure 3.8. Surface flow paint applicator for surface flow testing.

each side of the test section, angle at 45° with respect to the surface of the flat plate. This provided maximum illumination with minimal direct exposure to the cameras, see Fig. 3.9. Mounting lights on both sides of the test section also prevented any shadows from occurring as a direct result of the MVGs that would otherwise occur from using only one light.

3.3.4 Preparations

With the flat plate removed from the test section, the plate was configured for the next test according to the test schedule. Reconfiguring the flat plate involved removing the 1/4–28 bolts located underneath the plate which released a particular section of the flat plate. The section plate was then removed and replaced with the new desired section.

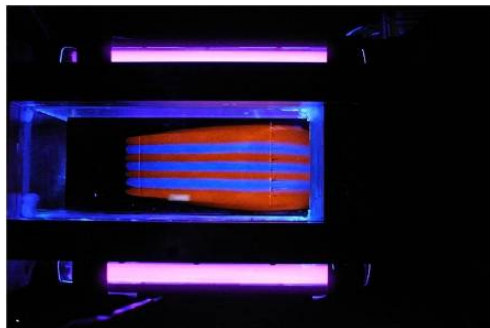


Figure 3.9. Photograph of test section results with mounted UV lights.

Surface preparation began with sanding the flat plate with 80 grit sand paper to remove any surface imperfections. The surface was then cleaned using window cleaner to remove any small particles. A thin layer of Bondo was applied to the surface to fill the cracks and areas between the plates. Approximately three hours was needed to allow the Bondo to harden. The surface was then sanded using multiple grit size sand paper starting from 80 grit to 100 or 150 grit and finally 220 grit. The surface was then cleaned using a paint brush and window cleaner. Two coats of matte black paint were applied to the surface. Once the paint dried, the flat plate was then ready to be reassembled back into the test section.

The plate was mounted into the test section in the reversed order in which it was disassembled. After the flat plate was securely mounted, the diffuser was reattached to the test section. The wind tunnel was prepared for operation according to the the SSWT operational procedures listed in Appendix B.3. A thin coat of blue and orange fluorescent paint was applied to the surface using the paint surface applicator described in Section 3.3. Once applied the side of the test section was reassembled and the SSWT was operated within 10 minutes of paint application. After completion of the test, the flat plate was once again removed from the test section and set aside where detailed images using the Nikon D300S could be collected. Upon collecting the surface flow images, the flat plate was reconfigured and prepared for the next test according to the test schedule. Total time of preparation, modification, testing and data collection for each configuration took approximately six hours.

After each test the image, video wind tunnel data, was collected cataloged and stored on an external hard drive. Each test generated approximately 2 Gb worth of data which include video, pictures, and SSWT data files.

3.4 Particle Image Velocimetry

The second type of test was conducted using is particle image velocimetry (PIV). PIV is a quantitative technique which uses a combination of a high intensive light source, digital cameras, and seed particles commonly known as tracers, to provide accurate velocity measurements of the flow being studied. The fluid being studied is ideally seeded with neutrally buoyant particles. Choosing the proper seed particle which closely represents the fluid is important. The seed particle is then illuminated with a high-intensity light source, usually a high-powered laser. A digital camera is then used to collect two images separated by a short time interval. The collected images are then correlated and the resulting calculations yield velocity vectors [4]. While the method is fairly sound for subsonic flow, for supersonic flow there are some concerns that require attention.

3.4.1 Equipment

The PIV system utilized in this study includes a New Wave Research Solo Model 120 double-pulsed Nd:YAG laser, two LaVision Image Intensive 3S cameras, and LaVision DaVis 7.1 software installed in a computer that houses the Programmable Timing Unit V8, as shown in Fig. 3.11. As with most PIV setups, the present system is positioned such that the laser sheet and the cameras are perpendicular with

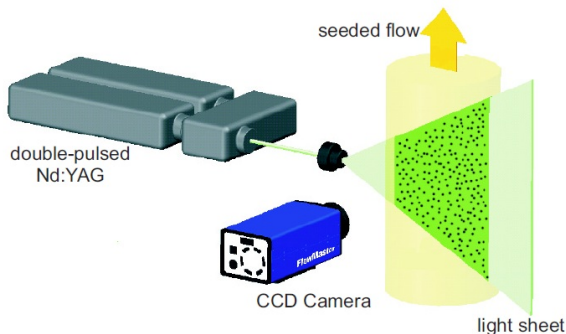


Figure 3.10. Typical PIV setup configuration[4].



Figure 3.11. PIV setup for study.

respect to each other. The laser and camera system are mounted on a custom-built 90° structure attached to a Lift Genie model 150 lift. This system allows for maintaining accurate alignment. If a different plane are desired for study, the entire system could be moved to the new plane while keeping the laser and cameras aligned with respect to one another, thus eliminating the need for calibration. The PIV system is equipped with two diverging lenses, with focal lengths of $f = -10$ mm and $f = -24$ mm.

The FlowMaster 3s Imager Intense cameras capture the images on a CCD chip with 1376×1040 pixels, each with a pixel diameter size of $6.45 \mu\text{m}$. The scanning rate of the cameras is 16 MHz and the maximum readout frequency is 10 fps. For stereo PIV, two cameras are needed and must satisfy the Scheimpflug criterion which states that the image plane, lens plane, and the object plane must be along a desired focal plane [4]. In order to accomplish this the cameras are adapted with a special adapter to allow the camera lens to be adjusted. For the stereo configuration, the Scheimpflug criterion also states that the angle between the two cameras must be at least 10° .

The manufacturer recommends a viewing angle of 30° – 45° . Synchronization between the cameras and the laser is handled by the Programmable Timing Unit (PTU) V8. The PTU and the DaVis software controls the firing of the laser, capturing the image, and image transfer between the camera and the computer. The user have the ability to modify the PTU settings; however, it is recommended by manufacture to leave the settings at their default values.

3.4.2 PIV Calibration

Calibrating the PIV system is important to ensure spatial accuracy. There are several requirements that need to be fulfilled in order to perform proper PIV calibration. Once calibration has been completed, the cameras and laser must maintain their position with respect to each other. If a different plane of interest or configuration is desired and the laser or cameras needs to be repositioned, the system will need to be re-calibrated. If their position with respect to each other can be maintained during relocation, then there will not be a need for recalibration. The PIV support system designed and built by Eric Braun and Rod Duke fulfills this requirement of maintain proper alignment when relocation is required.

Typical calibration procedures include the use of a calibration plate with known points as shown in Fig. 3.10. This calibration plate (LaVision type 20), is a three-dimensional plate for calibrating PIV systems in stereo configuration. The first task in calibrating a PIV system is to align the calibration plate to the desired plane of interests. The surface used for calibration faces the cameras. The second task is to align the laser with the surface of the calibration plate facing the cameras. Once the laser is aligned, it is turned off and neither the plate or the laser should be moved. The operator should take note that the computer uses the intensity value of each pixel to determine the location of each dot on the calibration plate. If the laser is turned on during calibration, the surface of the plate will become saturated with light

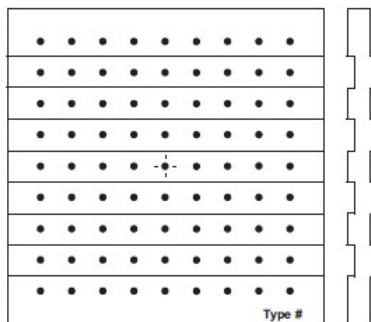


Figure 3.12. Type 20 Calibration plate for PIV.

and the computer will be unable to locate the predetermined dots resulting in poor calibration results.

The third task for proper calibration is to align the camera or cameras. The configuration of the system in either 2-D or stereo will determine technique required. For 2-D calibration, the single camera is set perpendicular to the plate as shown in Fig. 3.10. The operator must adjust the focus to ensure the entire field of view is in focus. After focusing, the operator then captures an image on the computer screen. The operator follows the instructions given by the computer or follows what is listed in the user manual [4] to perform system calibration.

In stereo configuration, two cameras are set at a minimum angular separation of 10° with respect to the other and the plane of interest [4]. The procedure for performing stereo calibration is similar to that for 2D calibration. Once the calibration has been the completed the computer will display the results to the user. This includes necessary information ,such as focal lengths, pixel per millimeter conversion and the RMS accuracy of the configuration. The manufacturer recommends an RMS fit value of less than one as good, a value lower than 0.3 as excellent and a value greater than 2 is considered questionable. Examples of PIV image calibration results is given in Fig. 3.14.

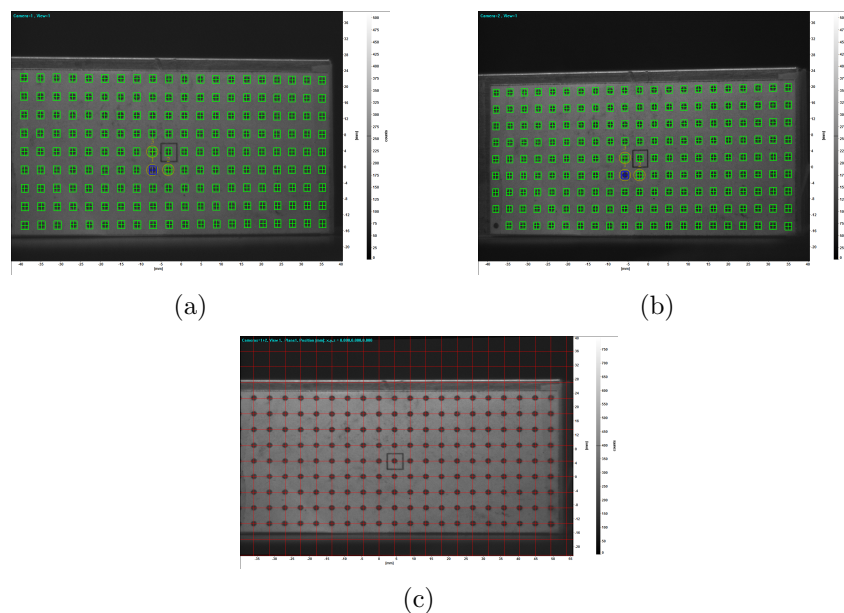


Figure 3.13. Dot search results for PIV calibration (a) Camera1 (b) Camera 2 (c) Calibrated.

For each image, the DaVis software searches for each dot on the calibration plate and warps the image so that the image from camera 1 and camera 2 equal one image viewed as if one camera was perpendicular to the area of interest.

Application of PIV calibration for the current study required minor modification. The original calibration plate purchased with the system was unable to fit inside the test section. The solution was to print out a configuration plate using Microsoft Excel. This printout was glued to a note card for stiffness and then attached to a rectangular aluminum block that was approximately 2 in. \times 4 in. (50.8 mm \times 101.6 mm). As required by the DaVis software, the diameter of the dots, the center-to-center distance in the horizontal and vertical directions were recorded. These values were entered in the computer's memory during the calibration process. Once the reference images were collected Fig. 3.13(a) and Fig. 3.13(b), the calibration was performed using the pin-hole fit model [4]. Examples of the rms values of cameras

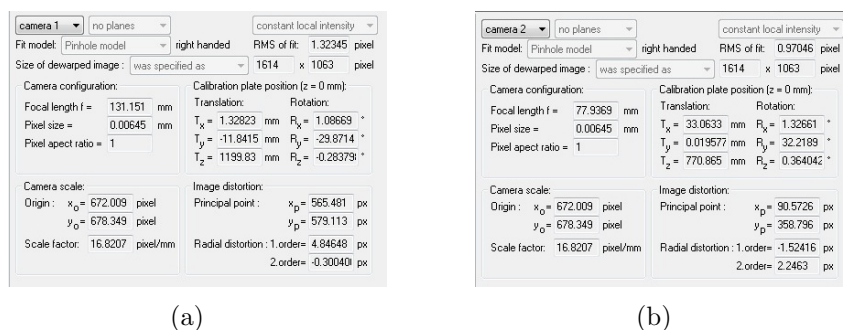


Figure 3.14. Calibration data for (a) camera 1 (b) and camera 2.

1 and 2 along with other calibration results such as pixel per mm, warpage in the (x, y, z) directions are given in Fig. 3.14(a) and Fig. 3.14(b).

3.4.3 Seeding

Proper seeding is crucial for collecting accurate and reliable data. In particular, the density and size of the seed particle need careful attention. Unlike the conditions under subsonic flow, seed particles in supersonic flows are exposed to high velocity and density gradients. This greatly affect the velocity of the seed particle and can bring into doubt the velocity data calculated by the correlation equations used in the software. One example of where such a concern is when a seed particle crosses a shock wave. Large velocity and density gradients can cause significant errors due to inertia of the particle when the flow is accelerating or decelerating [13]. The density gradients produced by shock waves also produce optical distortions. These distortions are due to nonuniform index refractions and can skew correlation peaks which can have a significant impact on velocity vector calculations [14]. With these concerns, a suitable seed particle needs to be chosen that will closely represent the density of air. The more closely the density of the particle is to the density of air, the more reliable the data becomes. Table 3.3 list some materials considered for use as a seed.

Table 3.3. Density of some common seed materials used for seeding

Seed	Density (kg/m ³)
Calcium carbonate	2830
Sodium biCarbonate	2173
Graphite	2267
Titanium dioxide	4230
Calcium sulfate	2320
Olive oil	914
Acetone	792.5

Given the results in Table 3.3, the density of the particle is very important. Other considerations such as water absorption and cost for $0.7 - 1\mu\text{m}$ size particles can greatly affect the decision for choosing a suitable seed. The seed particle initially chosen for this experiment was calcium carbonate. This particular material is widely available in small particle sizes on average of $0.7\ \mu\text{m}$. Calcium carbonate is hygroscopic. Therefore, it was first heated before use to evaporate the moisture. Calcium carbonate is also relatively inexpensive.

A closer study of seed particles characteristics indicated that it may be more beneficial to use a liquid particle as a seed instead of a solid particle. Liquid seeding particles such as acetone and ethyl alcohol are commonly used for flow visualization and as seed particles for filtered Rayleigh scattering. The diameters of common droplet of small particles in on the order of less than 100 nm [15]. Since the liquid droplets are small, it can be assumed that the shape of the particle is spherical. For the tests conducted in this study, a combination of calcium carbonate and acetone seeding was applied. The reason for this decision is given in Section 3.4.5. For the remainder of this section calcium carbonate will be used as an example.

Another important factor that needs consideration is the particle's relaxation time. The particle relaxation time (τ) is the time it takes for the particle to respond

to the change in conditions of the fluid. The particle relaxation time can be calculated using

$$\tau = d_p^2 \frac{\rho_p}{18\mu} \quad (3.4)$$

The smaller the particle's relaxation time the quicker the response to the change in momentum. For a detailed understanding on seed particles in supersonic flow, see reference [13]. Table 3.4 lists the particle relaxation time of the seeding material listed in Table 3.3. Each seed particle was assumed to have diameter of $0.7 \mu\text{m}$ and the viscosity of air is taken to be $1.6 \times 10^{-6} \text{ kg/m} \cdot \text{s}$.

Table 3.4. Particle relaxation time of some commonly used seed particles

Name	Relaxation Time, 10^{-6} s
Calcium Carbonate	4.809
Sodium BiCarbonate	3.697
Graphite	3.857
Titanium Dioxide	7.197
Calcium Sulfate	3.947
Olive oil	1.555
Acetone	1.347

3.4.4 Seeding Apparatus

It is important to ensure that the flow is seeded uniformly. Determining the location to introduce the seed particles as well as designing a proper delivery system needs special consideration. Since the test section involved supersonic flow, it was decided that the seed would be delivered into the plenum chamber where the flow was subsonic. An apparatus was designed by Richard Mitchell to deliver the calcium carbonate seed particles. The apparatus was designed to withstand a maximum

pressure of 250 psig. Preliminary test concluded that for good seeding, the seeder should be pressurized to 100 psi over plenum chamber pressure. Therefore the pressure delivered to the apparatus must be maintain at a minimum of 170 psig in order to supply sufficient seeding. The seeder apparatus is shown in Fig. 3.15.

The seeder used a cyclone design to mix the seed material with the air. The seeder was supplied with dry compressed air from a 175 psig compressor and entered the seeder through a pipe fitting located at the bottom of the seeder. Upon entry, the air was funneled into a 25.4 mm (1 in.) inner diameter union where it entered a cone-shaped funnel. This cone channeled the air and increased its velocity as it was directed to the main chamber. Once the air passed from the base housing, it entered the main housing and was split into two chambers. The outer chamber provided air to create the vortex while the inner chamber held the seed material. The area diverged in the inner chamber and encountered a filter not shown, with a porosity of $1\ \mu\text{m}$. This was small enough to prevent the majority of the seed from falling into the base housing while allowing air to travel through and mix with the seed material. As the air traveled upward with the seed, it passed through a second filter. This filter of $100\ \mu\text{m}$ was designed to break up any seed particles that might have clumped together.

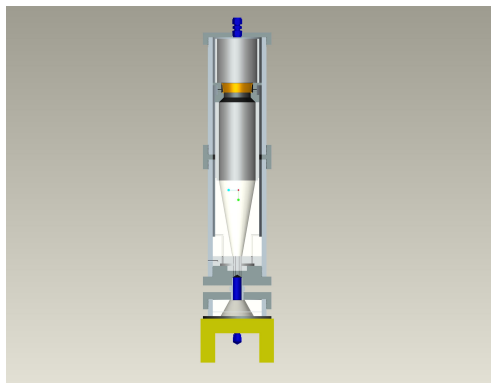


Figure 3.15. Pro-E drawing of SSWT Seeder apparatus..



Figure 3.16. Seeder delivery system located inside plenum chamber.

After the final filter, the inner and outer chambers were combined where the vortex flow was generated and then passed through the 12.7 mm (0.5 in.) exit port.

After leaving the seeder, the seed was delivered to the plenum chamber. The seed entered the plenum chamber from the upper right corner in Fig. 3.16. The seed is then injected into the freestream through several small holes located through the tubing. Before injection, most of the seed passed through a 4-way connector located in the center of the plenum chamber. Located at the center of this 4-way connector is a dowel pin. Previous tests showed that most of the seed passing through the center did not disperse through the holes and accumulated at the opposite end of the pipe. The dowel pin was effective in disrupting the flow. The results of the modification was a more even dispersion of seed particles. The white deposit seen in Fig. 3.16 are the results of a test conducted with 100 psig pressure using baking soda as a seed. Also, the white deposits shows that there is good dispersion of the seed.

Initially, the seeder was operated manually. It was soon realized that the high pressures entering the seeder quickly depleted all the seed supply before the wind tunnel was started. The solution was to install a McMaster-Carr No. 4738K502 Energy Efficient Buna-N Diaphragm brass solenoid valve that could be activated remotely. This 24 volt solenoid, Fig. 3.17(a) , valve was connected to a power supply through

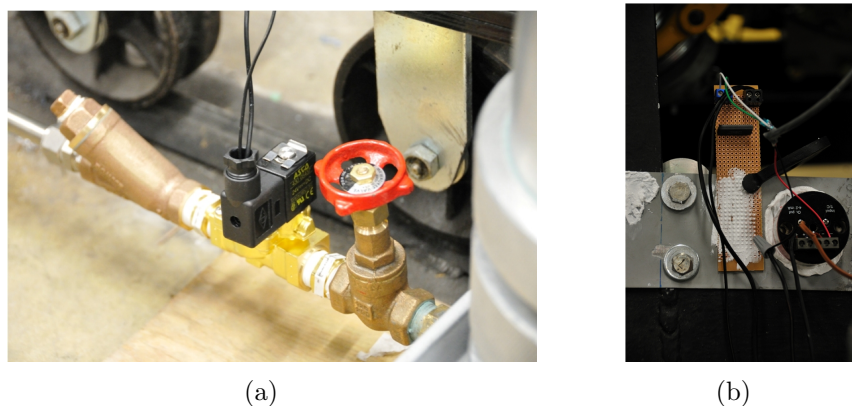


Figure 3.17. Seeder modification for LabVIEW control (a) Seeder solenoid valve (b) Seeder solid-state relay.

a solid-state relay. The solid-state relay, Fig. 3.17(b), is a Clare CLA209-ND relay configured to handle a 1.2 V trigger signal and is connected to a 0–100 Ω load with a maximum load current of 2.5 A. The 1.2 V signal is controlled by the Valve Controller which has the ability to produce a 1–10 V signal and is configured to activate the solenoid valve when the pressure in the plenum chamber reaches approximately 275 kPa (40 psig).

3.4.5 Boundary Layer Seeding

As discussed previously, the size of the particle is important in PIV testing. If the size of the particle is too large, the particle relaxation time of the seed may be too great and therefore not represent the flow. The test conducted with calcium carbonate showed that it is a good seed for collecting data, but the relaxation time is not low enough in keeping up with changing conditions within the boundary layer. Lower particle relaxation time means particles are more sensitive to changing conditions. It was decided that a more suitable seed particle was needed. Acetone has a lower density and particle relaxation time and was chosen as the boundary layer seed. Due to the sub-atmospheric conditions of the test section, the acetone entered the

test section naturally. The results of the seeding produced images with well defined structures of the turbulent boundary layer, see Fig. 4.21(b). These detailed images are a direct result of the condition of the acetone when it enters the test section. Using the Antoine Equation, the vapor pressure of the acetone can be determined [16].

$$V = 10^{A - \frac{B}{C_1 + T}} \quad (3.5)$$

where A , B and C_1 are functions of temperature. With a test section temperature of approximately 137 K (246 R) the results yielded a vapor pressure of 868 kPa (126 psia). Typical static pressures and temperatures were in the test section of 35 kPa (5.07 psia) and 137 K. It must be mentioned that while the conditions are such that the acetone is in a vapor state, the acetone enters the test section as a liquid. Taking into consideration the flow velocity of the test section and the rate of heat transfer of the acetone entering the test section, it can be concluded that the acetone itself is considered to be a wet vapor. As the acetone vaporizes, the droplet size become smaller and smaller. The result of the continually decrease in particle size results in a decrease in particle relaxation time.

3.4.6 Surface Reflection

Surface reflections are due to the high laser intensity reflecting off a surface causing unwanted glare. The severity of the reflection depends on the surface material, the power of the light source, the incidence and reflection angles. In order to obtain data near the surface, a solution is needed to reduce or eliminate the surface reflection. One possible solution is to use transparent polycarbonate sheets such as Lexan as the

surface. The Lexan polycarbonate allows the light source to pass through the surface which nearly eliminates all but a small fraction of surface reflection.

For the current study, a surface reflection reduction technique involving a combination of surface preparation, laser energy setting, and camera position is utilized. In order to prepare the flat plate for surface reflection reduction, surface cracks and imperfections must first be eliminated. This was accomplished by filling cracks and imperfections with Bondo. The Bondo is allowed to dry and is then sanded using an electric sander. A thin layer of matte black spray paint was then applied to the surface. In previous PIV tests conducted at the ARC, the matte black paint is well known to reduce the intensity of the surface reflection. The amount of reduction was not measured, but there was a qualitative difference between the painted and unpainted surfaces. A thin layer of rhodamine is applied next on top of the painted layer. Rhodamine absorbs light at around 530 nm. Since the wavelength of the laser is 532 nm, the layer of Rhodamine will strongly absorb the laser light.

Rhodamine is soluble in water or alcohol. But such a mixture does not attach itself well to metal surfaces. Instead, a similar liquid, Dykem Steel Red, was found to possess suitable absorption characteristics as well as attach itself to metal surfaces. This dye was applied to the local area of interest being studied. If applied properly, the surface reflection can be reduced drastically allowing data collection very close to the surface.

A high laser intensity setting can cause excessive reflection. The laser must be set to an energy state so as not to cause excessive reflection. At the same time, there must be a balance between the ability of the cameras to pick up reflection from the seed particles without saturation. The amount of surface reflection can also be reduced by the position of the cameras. LaVision recommends the Image Intense 3S cameras and the laser sheet to be perpendicular to each other. In the present

experiments, the cameras are set at approximately 10° with respect to the with the flat plate surface to reduce the amount of surface reflections. With the combination of surface preparation, laser intensity, and camera positioning, stray reflections into the cameras can be significantly reduced.

3.4.7 Preparations

A typical test preparation cycle for PIV testing is similar to the preparation cycle for surface flow visualization. The flat plate was first removed in the same manner as described in Section 3.3. The plate was then reconfigured and the surface was prepared in the same similar manner. After the application of the Dykem red, the flat plate was placed in a cabinet and allowed to dry for approximately 30 minutes. Once the surface was dried, the plate was reinserted into the test section and the wind tunnel was prepped for testing. Wind tunnel operation time was approximately 30 seconds and collected approximately 128 images per test configuration. The SSWT Controller was programed to control operation of the seeder as well as triggering the PIV system through a TTL signal. Triggering the PIV computer proved not to be entirely reliable. As a result the PIV system was triggered manually using Windows Remote Desktop. Upon completion of the test, the collected images were reviewed. Vector calculations were performed on approximately five images as part of the review. If the images had sufficient seeding of the boundary layer, proper light exposure, and decent vector results, then the test was considered satisfactory and the flat plate would be reconfigured for the next test. If the images were not considered satisfactory, the test was performed again.

3.5 Boundary Layer Analysis

The PIV data was analyzed to obtain the boundary layer velocity profiles which were subjected to further analysis. The analysis described below represents a set of

calculations for one configuration. Each configuration conducted during PIV testing was put through the same process. For results of each configuration, the reader is directed to section 4.2.

3.5.1 PIV Vector Pre-Processing

Before boundary layer analysis and velocity vectors could be calculated, image manipulation was required. This involved, first, the application of a mask to each image collected. The mask reduced the required area for computer analysis and was applied individually to each plate configuration. The boundaries of the mask included the area of flow considered to be just below the surface of the ramp to a general height of 8 mm.

The second step involved changing the intensity scales of the images. The two types of seed particles had noticeable different reflection characteristics. The settings of the laser and camera were adjusted so that the collected images would show both the acetone and the calcium carbonate. However, maximum intensity of the laser was limited to prevent over saturating the acetone very near the surface. If the acetone became saturated by the laser light, the data would be corrupted. The axis of the image was also manipulated so that a point of reference can be defined. The x -axis origin was set to be at the beginning of the MVG ramp, while the y -axis origin was the surface of the flat plate. The coordinate system follows the right hand rule and the direction of flow is from left to right in the x -axis and the vertical is the y -axis. The final pre-processing step was to normalize the intensity values. This process is a DaVis function which located the maximum and minimum intensity values defined by the scale length that is determined by the user. For this study, the scale length was ten. The software located the medium intensity value and rescaled the intensity values based on the maximum and minimum. This ensured that the majority of the particles contributed to the calculations.

The image pre-processing method ensured that the images were best suited for vector processing. In addition, for visual representation, further image manipulation was performed. The image intensity scale was redefined from a linear to a logarithmic scale. This reduced the separation range of each pixel and resulted in the acetone and calcium carbonate particles to become more visible. The effect of this close proximity resulted in images that were not suitable for vector calculations due to the intensity variation was considered to be too small.

Vector processing of the images were performed using the cross-correlation method. Vector iterations was performed with a multi pass of 16×16 pixel interrogation windows with an 87% overlap. The large overlap increased the number of vectors calculated as well as the accuracy of each interrogation window [4]. Because the boundary layer is focus of this study, the interrogation windows were further reduced during the second pass to a 4×4 pixel interrogation window. Several optional functions were required by the DaVis software when performing multipass calculations that could not be modified by the user. Upon completion of vector calculations, the resulting vector fields were then averaged and one vector field per test and per camera was the result. The average velocity vector fields produced an image with an average of over 220,000 vectors. This vector field was then exported into a .dat file format for further processing.

3.5.2 PIV Post-Vector Processing

The data files produce by the DaVis software produced text files in excess of 6 MB. Due to the excessive amount of data, individual files were imported into Microsoft Excel for reduction. The information in each data file generated by the DaVis software include the velocity data $(V_x(x, y), V_y(x, y))$. For the present study, only the streamwise velocity component V_x was used.

The velocity data was imported to one spreadsheet and organized from smallest to largest values in the x direction and then organized similarly in the y direction. Velocity profile locations upstream of the MVGs were chosen taken every 5 mm starting with -5 mm. The velocity profile that is actually presented consisted of an average of three profiles, namely, those at the location and at planes immediately upstream and immediately downstream from its location. The result was a more accurate profile. The separation between the three planes was 0.06 mm (0.0023 in). Due to the small change in vector position, the y -axis reference location was adjusted for the higher accuracy. The y -axis reference was taken to be where the first positive V_x value occurred. After applying these manipulations to each configuration, boundary layer analysis was performed.

3.5.3 *Turbulent Compressible Boundary Layer Calculations*

Turbulent compressible boundary layer analysis performed here followed AGARD 335 [7]. Only the essential equations and concepts that pertain to this study will be expressed here.

Supersonic turbulent boundary layer flow in this study is assumed to follow Morkovin's Hypothesis which states that, "the essential dynamics of compressible shear flows will follow the incompressible pattern" [17]. The objective of this analysis is to validate that the data collected during the test agree with theory. This is accomplished by calculating the velocity transformation, performing a non-linear curve fit to find u_τ , and plot the velocity profile in terms of the inner variables u^+ and y^+ . To verify the data collected the finished profile should look similar to Fig. 3.18. Considering Eqs.(3.6) and (3.7), u_τ is the only unknown variable and cannot

be determined directly through experimental measurements in this study.

$$u^+ = \frac{\bar{u}}{u_\tau} \quad (3.6)$$

$$y^+ = \frac{u_\tau y}{\nu_w} \quad (3.7)$$

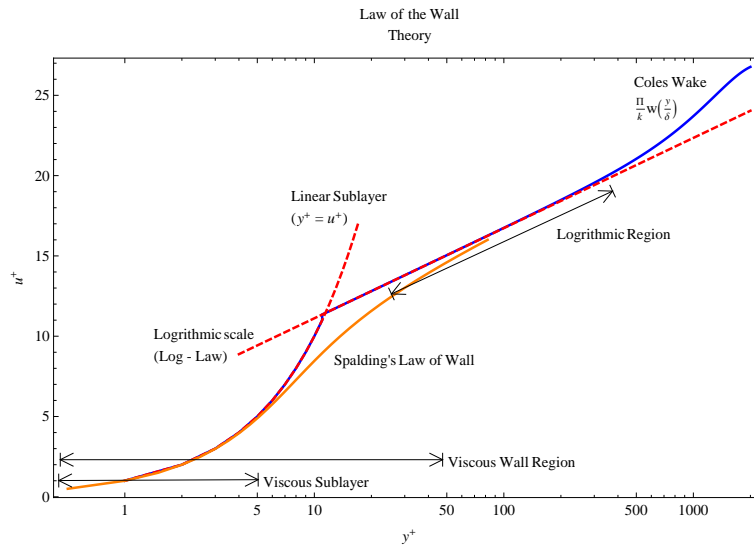


Figure 3.18. The turbulent boundary layer in law-of-the-wall coordinates.

With the imported data varying with time, the freestream condition values need to be defined. An example of the freestream data, in this case the Mach number, is shown in Fig. 3.19. To determine the freestream conditions, a function in Mathematica called the “commonest function” was applied. This function searches the selected set of data and determines which value is repeated the most and is returned as the solution. This commonest value for Mach number is plotted as a solid line in Fig. 3.19. This process provided sufficient verification of determining freestream conditions. This function was also applied to other sets of data including the total

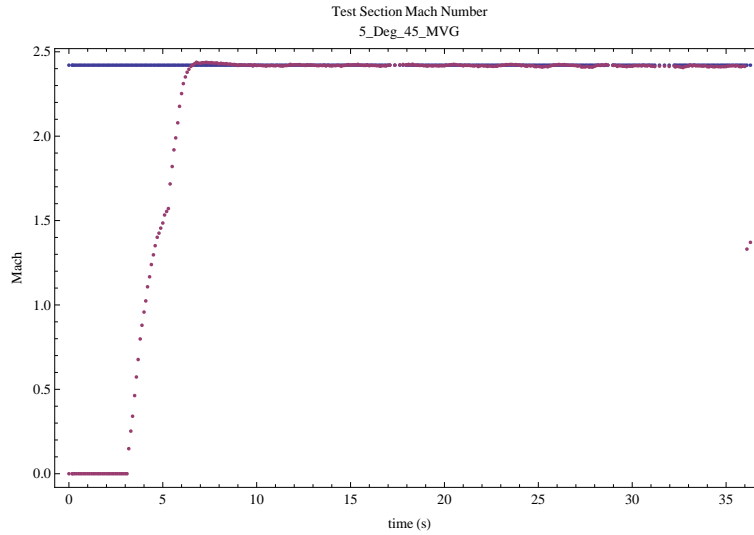


Figure 3.19. Example graph of test data..

pressure and total temperature taken from the plenum chamber, the static pressure taken at the entrance of the test section, test section Mach number, test section temperature, and test section static pressure ratio.

Certain properties at the wall must be known or assumed a priori. It is assumed that the wall temperature is

$$T_w = T_{aw} = 0.9T_o \quad (3.8)$$

Knowing the wall temperature, the wall viscosity can be calculated using Sutherland's formula for air

$$\mu_w = 1.45 \times 10^{-6} \left(\frac{T_w^{3/2}}{T_w + 110} \right) \quad (3.9)$$

For the flat plate at zero incidence, the static pressure is considered constant in the boundary layer. Thus, the wall pressure is equal to the freestream pressure.

Knowing the wall temperature and pressure, the perfect gas law allows the wall density to be obtained as

$$\rho_w = \frac{P_3}{RT_w} \quad (3.10)$$

from which the kinematic viscosity at the wall can now be obtained

$$\nu_w = \frac{\mu_w}{\rho_w} \quad (3.11)$$

The density at the edge of the boundary layer can be calculated using

$$\rho_e = \frac{P_3}{RT_e} \quad (3.12)$$

With the freestream and wall conditions known, the PIV data can be now be processed. Similar to the SSWT data, the velocity profile was plotted with respect to its location within the boundary layer. Depending on the accuracy of the data, applied method and velocity profile will reveal two distinct layers. The first layer is called the inner layer which is dominated by viscous forces [17]. Within this region the inner law variable become equal to each other and the calculations change to $u^+ = y^+$, see Fig. 3.18. The second layer is called the outer layer consisting of the logarithmic region and the wake region where Eqs.(3.17) applies. To accomplish this a second order polynomial was applied to the recorded velocity data. The results of this curve fit provided a smooth profile for Eqs. 3.17 and was plotted with the original outer layer profile to which an observation was made to determine the accuracy.

The velocity profile is then subjected to the van Driest II transformation. The Crocco–Busemann equation was used to relate the density and temperature profiles to the velocity profile [17]

$$\frac{\rho_w}{\rho} = \frac{T}{T_w} = 1 + \left(\frac{T_{aw}}{T_w} - 1 \right) \frac{u}{u_e} - \frac{r(\gamma - 1)}{2} M_e^2 \frac{T_e}{T_w} \left(\frac{u}{u_e} \right)^2 \quad (3.13)$$

The Van Driest Velocity

$$u^* = \frac{u_e}{B} \left(\arcsin \left[\frac{2B^2 \frac{u}{u_e} - A}{\sqrt{A^2 + 4B^2}} \right] + \arcsin \left[\frac{A}{\sqrt{A^2 + 4B^2}} \right] \right) \quad (3.14)$$

was then obtained, where

$$B = \sqrt{\frac{r(\gamma - 1)}{2} M_e^2 \frac{T_e}{T_w}} \quad (3.15)$$

$$A = \left(1 + \frac{r(\gamma - 1)}{2} M_e^2 \right) \frac{T}{T_e} - 1 \quad (3.16)$$

and $u_e = u_\infty$.

As shown in Fig. 3.18, the outer region of a turbulent boundary layer includes the Coles “law of wake.” Thus, a composite profile from the logarithmic region to the boundary layer edge, known as the wall-wake law, can be written as

$$\frac{u}{u_\tau} = \frac{1}{k} \ln \left(\frac{u_\tau y}{\nu_w} \right) + C + \frac{\Pi}{k} \left(1 - \cos \left(\frac{\pi y}{\delta} \right) \right) \quad (3.17)$$

where $k = 0.41$ and $C = 5.5$ which leaves three unknown parameters, u_τ , δ and Π . Although these three values are unknown, there is some insight as to what two of these values are expected to be. An estimate of δ can be obtained from the ensemble average velocity profile and confirmed by the schlieren images. The term Π is the Cole's wake parameter, which for a zero pressure gradient, equilibrium turbulent boundary layer, has a value of 0.55 ± 0.01 . The last variable u_τ has no known value or range of values. However, fitting the transformed velocity profile to Eqs.(3.17) allows these three parameters to be obtained. The value is determine by performing a non-linear curve fit. The results of the fit yields the values of u_τ , δ , and Π . Next, with u_τ calculated, the friction coefficient can be found using

$$C_f = 2 \left(\frac{u_\tau}{u_e} \right)^2 \quad (3.18)$$

Within the viscous sublayer the logarithmic curve fit does not apply below $y^+ = 10$, see Fig. 3.18. Below $y^+ = 10$ the boundary layer is purely dominated by the viscous shear forces and u^+ and y^+ become linear. From $y^+ = 10$ to $y^+ = 100$ this region is in transition and is neither linear nor logarithmic. This region is properly named the buffer layer.

$$u^+ = y^+ \quad (3.19)$$

In fitting the PIV data to the wallwake law, the data nearest the wall should be removed. This is necessary because the data may be in the viscous sublayer which should be discounted in performing the wallwake fit. Plotting the raw velocity profile in a log-linear plot should reveal the viscous sublayer region.

Integral parameters can be calculated from the boundary layer profile. The two most common profiles are the displacement and momentum thicknesses

$$\delta^* = \int_0^\infty \left(1 - \frac{\rho}{\rho_e} \frac{u}{u_e} \right) dy \quad (3.20)$$

$$\theta = \int_0^\infty \frac{\rho}{\rho_e} \frac{u}{u_e} \left(1 - \frac{u}{u_e} \right) dy \quad (3.21)$$

The displacement thickness is a measure the deficiency of the mass flow rate due to the existence of the boundary layer. The momentum thickness is a measure of the momentum-flux deficit caused by the existence of the boundary layer.

It is common to express the displacement and momentum thickness in terms of Reynolds number. The calculated Reynolds number for this study is given in Eqs. 3.22 and 3.23. Consideration must be taken in choosing the viscosity when calculating the momentum thickness Reynolds number. In supersonic flow there is a possibility that taking the viscosity based on freestream conditions, the Reynolds number would suggest the flow is turbulent. However, calculating the Reynolds number based on adiabatic wall conditions would suggest the flow is laminar. This is mainly due to the fluid property gradients and the increase in the viscous sublayer as the freestream Mach number increases. Based on these considerations, the preferred method of calculating momentum thickness Reynolds number for supersonic flow is given as 3.23 [7].

$$Re_{\delta^*} = \frac{\rho_e u_e \delta_e}{\mu_w} \quad (3.22)$$

$$Re_{\theta_{aw}} = \frac{\rho_e u_e \delta_e}{\mu_w} \quad (3.23)$$

3.6 Schlieren Imaging

Schlieren and shadowgraph are two well known techniques that are used to image compressible flow. The only difference between the basic shadowgraph setup, and a schlieren system configuration is the addition of a knife edge to block most of the source light. For this study, only the schlieren technique was performed. The schlieren technique involves the collecting images based on the first spatial derivative of the refractive index due to the changing in density [18].

3.6.1 System Setup

There are many different types of schlieren configurations. Some example configurations are the simple lens-type system, a combination of lens and mirror, and the Z-configuration. All schlieren systems follow the same basic technique which involves focusing light rays produced from a source light into a collimated beam. The rays then deflect off any density gradient according to

$$\epsilon_x = \frac{L}{n_0} \frac{\partial n}{\partial y} \quad (3.24)$$

Considerable note must be taken of Eqs.(3.24). The angular deflection ϵ_x is directly proportional to the length along the optical axis L , and the gradient $\partial n/\partial y$. These will become important in the experimental setup later. After the light rays have been deflected, they are collected by a video or still camera and recorded. The severity of the density gradients will produce a bright or dark image depending the orientation of the knife edge.

For this study, the Z-type configuration is utilized. The setup of Z-configuration system begins with the light source. The light rays emitted from the light source diverge with increasing distance. Therefore, a condenser lens is used to converge the

light rays to a single point. The light then passes through a source slit, also known as a spatial filter. The source slit gives the schlieren image definition in both size and shape. It is desirable to fill the source slit with most of the higher intensity light that is emitted from the light source. The source slit is located at the focal point of the first parabolic mirror. After the light rays are deflected off the first mirror, the light rays then pass through the test section where the density gradients impose their effect on the parallel rays. The rays are then collected by a second parabolic mirror and deflected toward the camera. At the focal point of the second parabolic mirror, the focal point itself resembles the shape of the source slit. A knife edge is positioned at this focal point and is designed to block out the majority of the source light. The light affected by the density gradient is not at the original location as its neighboring light rays. Thus, depending on the direction of deflection of the light rays, more or less light passes the knife edge and continues toward the camera, thereby providing the variation of light intensity that forms the schlieren image. The image is then focused and captured by digital cameras for further study.

While the Z-type configuration is simple to configure, the user must take note of the location and position of each component of the system. Precise location is needed in order to ensure a well-defined schlieren image. The location of each component begins with determining the location of the two parabolic mirrors. Each mirror is first placed at least two focal lengths apart. The source slit and the knife edge are to be placed at each focal length at the same offset angle with respect to each mirror. The offset angle of each mirror needs to be exactly the same in order to reduce coma [18]. The condenser lens and the light source are placed at their respective locations with the source slit being the reference point. If the lens and the light source are in their correct position, the diameter of the light that reflects off the first parabolic mirror will be the same diameter at the location of the second mirror; in other words, the

beam is collimated. If the diameter is not the same, then the light source location can be adjusted to ensure proper diameter. As stated previously, the knife edge is located at the focal length of the second mirror. After the knife edge, the distance between the focusing lens and the camera depends on the distance between the two mirrors. The reader is referred to [18] for detailed discussion. In order for the test object to be in focus, its location must be at a distance s between the focal points of the two mirrors. The distance from the test object and the second parabolic mirror is now $s + f$. The location of the camera and the image magnification is given by

$$e = m \left(f_2 - \frac{sg}{f_2} \right) \quad (3.25)$$

$$m = \frac{f_2}{s} \quad (3.26)$$

where e is the length from the focusing lens to the camera, and g is the distance from the focus lens to the knife edge. In some cases, the g and e are known and do not meet the requirements to properly focus the image or the area utilized for testing is not large enough to satisfy e . In order to compensate for the situation, Eqs.(3.25) can be rearranged with the help of Eqs.(3.26) to find the distance s with known values of $e + g$;

$$s = \frac{f_2^2}{e + g} \quad (3.27)$$

The Aerodynamics Research Center has designed and developed its own portable schlieren system. This system is designed for use with various facilities. The system

includes two Steel Sentry Rx Series 60 1.52×6.09×1.16 m (9× 24 × 46 in.) tables. The dimensions of the table were determined from the required location of each of the optical components of the schlieren system as well as the height of the SSWT test section. The light source is a Nasun WFL604MR161D3W 3 W white LED which produces approximately 150 lumens. The light passes through an Edmund Optics NT43-593 50 mm ϕ × 40 mm FL condenser lens with an effective focal length of 44 mm (1.73 in). After passing through the condenser lens, the light passes through a source slit that is 1 mm (0.039 in) in height and 2 mm (0.078 in) in width. The condenser lens and the light source are then adjusted to a position such that the light passing through the source slit with the greatest intensity fills its entire area. The light then diverges and is reflected by one of two Edmund Optics NT32-071-533 152.4 mm (6 in.) diameter parabolic mirrors with a 914.4 mm (36 in.) focal length. The collimated light is then collected by the second parabolic mirror where it then converges to a focal point. An ordinary razor blade is used as a knife edge. After passing the knife edge, the light then passes through a focusing lens where it is then captured by a Nikon D300S camera in shutter and video mode. This completes the configuration setup for the Z-type schlieren system.

3.6.2 Preparations

The preparation cycle for these tests is similar to those for surface flow visualization and PIV. The test cycle began with the desired configuration of the flat plate according to the test schedule, Table 4.9. The surface of the plate was prepared using Bondo to fill any cracks that could possibly produce shock waves and also to fill in imperfections, such scratches and divots on the surface. The Bondo was allowed to dry for approximately three hours and was then sanded in the same manner as per the surface flow visualization and PIV. Since surface contrast as for surface flow visualization or surface reflections as for PIV are not a concern for schlieren testing,

painting the surface was unnecessary. Upon completion of model preparation, the plate was then reinserted into the test section and the wind tunnel was prepped for operation. The plenum chamber pressure was approximately 448 kPa (65 psig) and run times were approximately 20 s.

Due to the characteristic setup of the schlieren system, two runs were needed for each configuration. The first test was conducted using the Nikon D300S. The video provided flow characteristics in real time. Video settings of the Nikon D300S were 24 fps with an image size of 1280×720 pixels. With the exception of the configuration *No Ramp No MVG*, all video data collected recorded the full operation of the wind tunnel. The second test conducted gathered still images with the same Nikon D300S with the camera shutter speed of $1/8000$ s. However, the image was collected under the same wind tunnel conditions as for the video. The high shutter speed was unable to eliminate the blurring, but these effects were reduced. Due to hardware limitation on the camera, only 11 to 12 images could be collected in one run.

CHAPTER 4

RESULTS AND DISCUSSION

The results of the different types of tests conducted in this study are organized into three sections. Each configuration of the flat plate was given a designated name. For example, the common flat plate configuration was designated as *No Ramp No MVG*. The 5 degree ramp with the 45° trailing edge micro-vortex generators was designated as *5 Deg 45 MVG*.

4.1 Surface Flow Visualization

Surface flow visualizations were conducted in this study to understand surface flow characteristics. The surface flow tests was conducted in accordance to the test schedule listed in Table 4.1.

Table 4.1. Surface Flow Test Schedule

Test	Configuration	MVG	Data to Collect
3	No	No	Video,Close up,Picture
6	No	45	Video,Close up,Picture
9	No	70	Video,Close up,Picture
15	5 Ramp	No	Video,Close up,Picture
18	5 Ramp	45	Video,Close up,Picture
21	5 Ramp	70	Video,Close up,Picture
27	25 Ramp	No	Video,Close up,Picture
30	25 Ramp	45	Video,Close up,Picture
33	25 Ramp	70	Video,Close up,Picture
39	Cyl.	No	Video,Close up,Picture
42	Cyl.	45	Video,Close up,Picture
45	Cyl.	70	VideoVideo,Close up,Picture

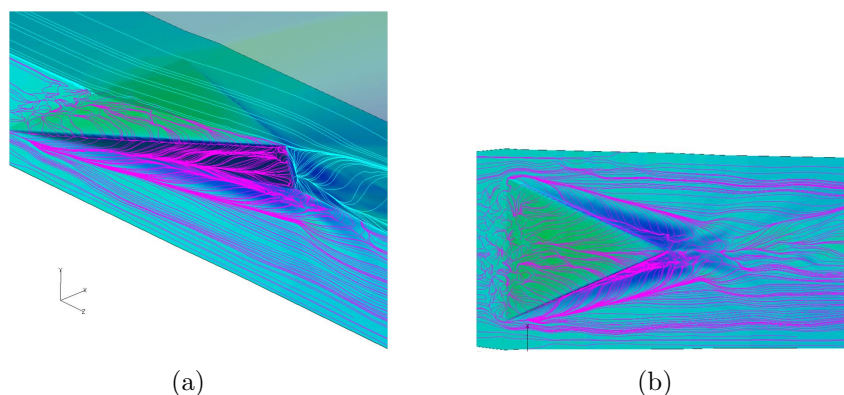


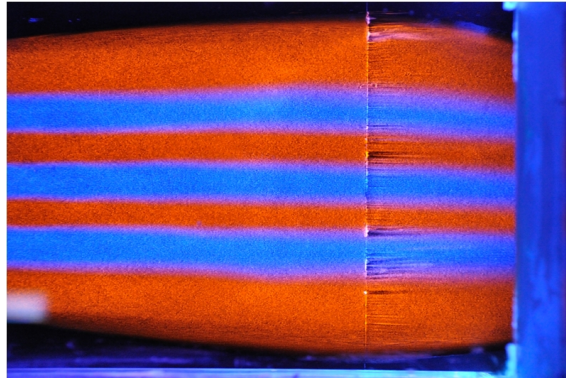
Figure 4.1. Surface streamlines of MVG45 from LES (a) Angled view (b) Vertical view.

4.1.1 Qualitative Results

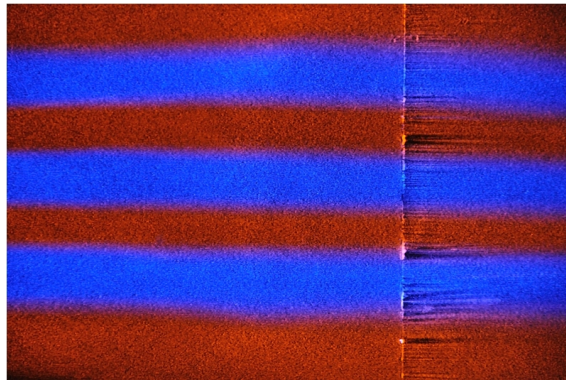
A qualitative analysis was performed for each flat plate configuration. The analysis involved a visual observation of the effects of the MVG and a comparison with LES results [1]. Fig. 4.1(a) and 4.1(b) represents two LES surface streamline results of the MVG45 configuration. Flow characteristics include leading edge separation, horseshoe vortex, and areas of high velocity flow.

4.1.1.1 Flat Plate

Surface flow visualization of a simple flat plate serves as a reference for flow quality verification. This configuration is given the designation *Flat Plate No MVG*. Fig. 4.2 shows the results of the flat plate configuration test. The flow direction is from left to right. The use of two colors is helpful in indicating whether mixing is occurring. Indication of mixing would show up as pink. Seen in Fig. 4.2 is an artifact in the form of a line perpendicular to the direction of flow just to the right of center. This is a direct result of the intersection of two individual plates. As explained in the experimental setup, Bondo was used as a filler between the intersecting plates. Unfortunately, it appears that the compression forces on the plate are greater than the



(a)



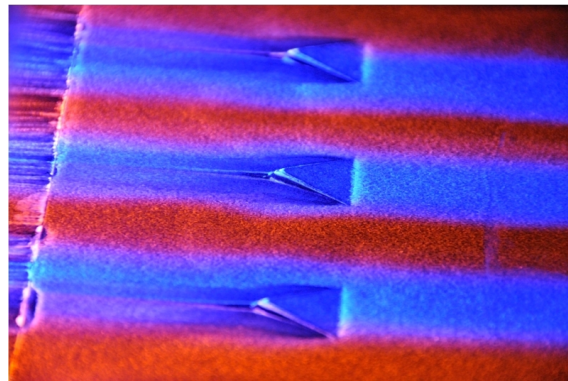
(b)

Figure 4.2. Surface flow results of *Flat Plate No MVG* taken from (a) Canon (b) Nikon.

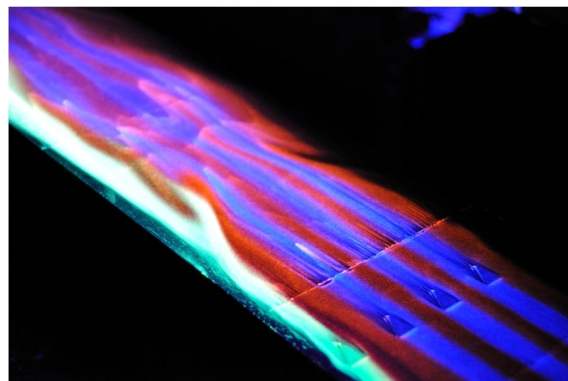
Bondo's maximum tensile strength. The failure of the Bondo was the only noticeable interference occurring during the tests. A secondary test was conducted using JB Weld compound and had the similar results. Future modification of the flat plate should include the surface as one piece to prevent such distortions from occurring.

Surface flow visualization was also performed separately on *Flat Plate MVG 45* and *Flat Plate MVG 70*. The visualizations appeared to be qualitatively similar, see Fig. 4.3 and Fig. 4.4 respectively. Referring to Fig. 4.3(b), a green mixture was added next to the original color scheme. This extra color was included to help reveal

details about wall boundary layer interference. The visualization showed an unusual hook pattern downstream of the MVGs. Further analysis concluded that this hook pattern was the disturbance caused by the intersection of the optical glass and the aluminum section located on the test section side wall. This wall boundary interference was noticed in all surface flow test conducted. However, since the disturbance was downstream of the desired test area, it did not pose any problems. While not in focus in Fig. 4.3(b), the pinkish area downstream of the vortex generators is a sign that some mixing occurred.



(a)



(b)

Figure 4.3. Surface flow results of *Flat Plate MVG 45* (a) Close view (b) Downstream view.

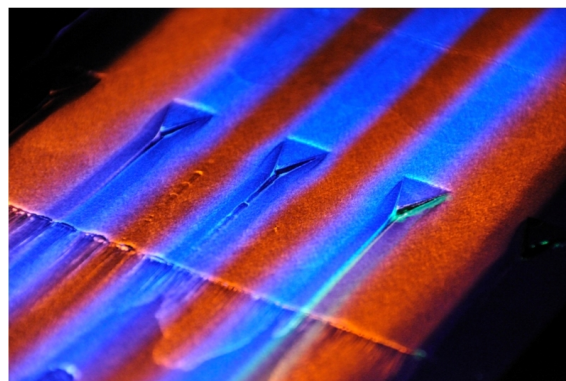
For the MVG70 configuration seen in Fig. 4.4(a), a small amount of the green paint was applied to the intersection between an MVG and the flat plate. This was done to examine the flow characteristics near the MVG, specifically to understand if there was flow separation around the MVG. The results showed a dark color, that is, more of the underlying black surface was revealed, indicating that the pigment was scoured away. This is considered to be evidence of an open separation. Further topological analysis of this and visualizations from other investigators suggest that this open separation consists of a large vortex trailing downstream that is different from the horseshoe vortex that is generated off the MVG leading edge.

A comparison of the experimental visualizations of both MVG configurations seen in Fig. 4.3(a) and Fig. 4.4(a) to the computational results seen in Fig. 4.1(a) reveals noticeable similarities. In the experimental visualizations, the black color represents areas of high momentum flow. This is also depicted in Fig. 4.1(a) by the herringbone pattern of the surface streamlines. Other similarities reveal leading edge separation at the edge of the ramp.

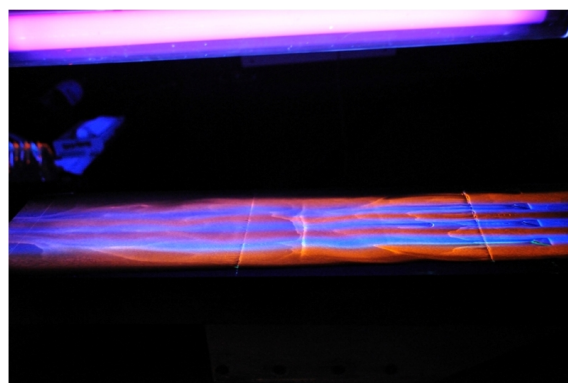
The tail view in Fig. 4.5 yields a distinct characteristic in both the experimental and numerical visualization. Near the trailing edge of the vortex generator in Fig. 4.5(a) there appear two swirl patterns indicating the possible existence of vortex filaments. Interestingly, there are areas of pigment accumulation in Fig. 4.5(b) at similar locations. The accumulation is a direct result of a vortex filament. Video results of later test confirm existence of such a vortex filament.

4.1.1.2 Five Degree Ramp

The next configuration to be tested was the 5 degree ramp. The designation for this configuration is *5 Deg No MVG*. The surface flow visualizations results appear similar to that of the flat plate configuration. Straight streamline patterns of the blue



(a)



(b)

Figure 4.4. Surface flow results of *Flat Plate MVG 70* (a)Close view (b) Downstream view.

and orange paint indicate minimal distortions and uniform flow. The only disruption noticeable was a disturbance near the top of the ramp in Fig. 4.6(b). This disturbance is due to wall interference which was also seen in Fig. 4.3(b).

Upon completion of the reference test, the 5 degree ramp was configured for the MVG45 and MVG70 tests. The MVG45 was designated as *5 Deg 45 MVG* and the MVG70 was designated as *5 Deg 70 MVG*. The surface visualization results of the MVG45 and MVG70 tests are given in Fig. 4.7 and Fig.4.8 respectively. Figures 4.7(a) and 4.8(b) reveal flow features similar to the MVG45 and the MVG70 flat plate

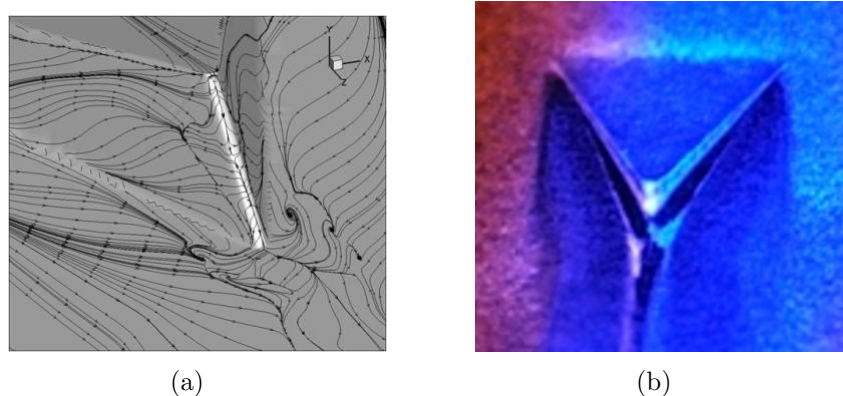
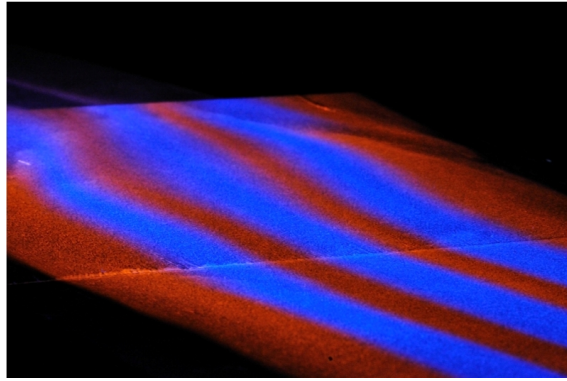


Figure 4.5. Surface flow characteristics results (a) LES, (b) Experimental.

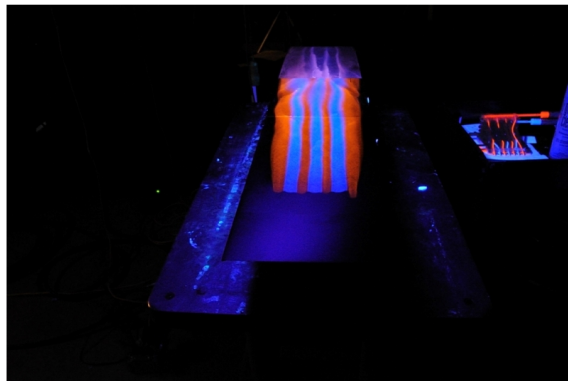
configuration. Flow separation can be seen at the leading edge of the MVG and high velocity flow is revealed by the dark areas along the side of the MVG.

Downstream of the MVG array and on the ramp itself in Fig. 4.7(b), the surface flow pattern is somewhat different than the *5 Deg No MVG* and the *5 Deg 70 MVG* configurations and similar to *No Ramp 45 MVG* configuration. The erratic pattern within the surface flow might suggest that the MVG's have affected.

After the 5 degree ramp and the flat plate test were conducted, two additional configurations were tested. The first additional configuration was the 25 degree ramp and was given the designations *25 Deg No MVG*, *25 Deg 45 MVG*, and *25 Deg 70 MVG*. The general purpose of testing the 25 degree ramp was to determine the MVG effects on severe flow separation at large ramp angles. Fig. 4.9 displays the results of the 25 degree reference configuration test. As indicated in both figures, the surface flow appears to be suddenly stopped. This sudden stop was later found to be due to an unstart condition. To confirm the results that an unstart condition exists and to investigate the effects of the MVGs, a second test was performed with MVG45. The results of the test were similar to the previous configuration. A green paint was added to the leading and trailing edges of the 25 degree ramp to improve contrast



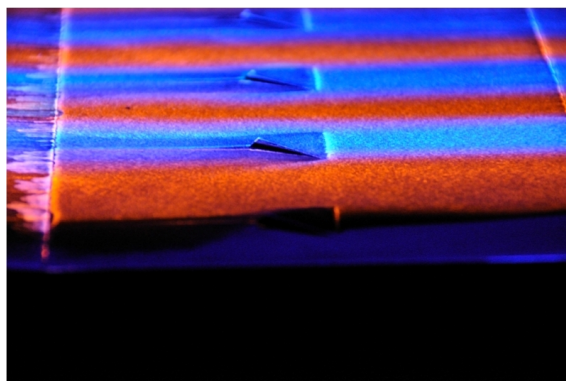
(a)



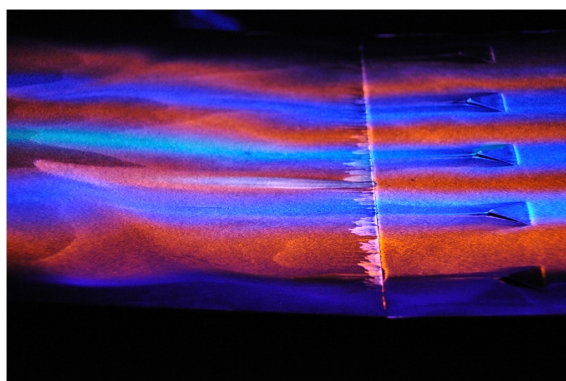
(b)

Figure 4.6. Surface Flow test results of *5 Degree No MVG* (a) Ramp view (b) Plate view.

within the surface flow colors. Flow separation is clearly indicated by the little to no mixing of the fluorescent paints. Several modifications were made to attempt to start the test section, including reducing the height of the ramp to 0.4 in. which is lower than the 5 degree ramp, rounding the top portion of the ramp, and shortening the overall length of the ramp. Unfortunately, the unstart condition still remained. Later study concluded that the unstart condition was likely caused by a Mach reflection off the test section ceiling [19].



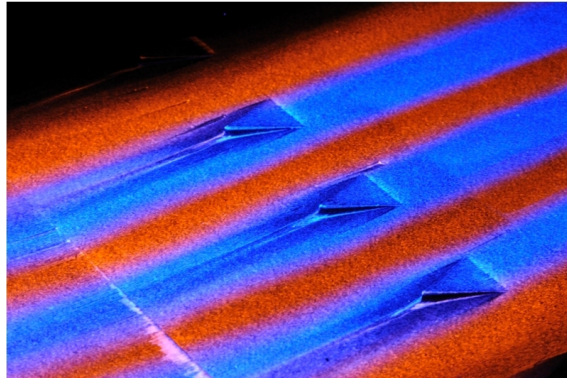
(a)



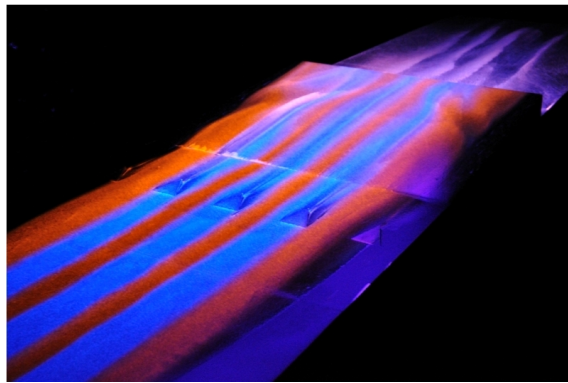
(b)

Figure 4.7. Surface flow test results of *5 Degree 45 MVG* (a) Near view (b) Downstream view.

While the unstart condition is unfortunate for the desired study, the results of these tests provide useful information about the effects of MVGs on such conditions. The effects of MVG45 on an unstart condition can be seen in Fig. 4.10(a). The surface patterns indicate that vortices were generated as seen with the 5 degree ramp and flat plate configurations. Upon intersecting the region of severe flow separation the vortices appear to have little effect in reducing this region. The results in Fig. 4.10(b) indicate that the vortices generated by the ramps are not strong enough to



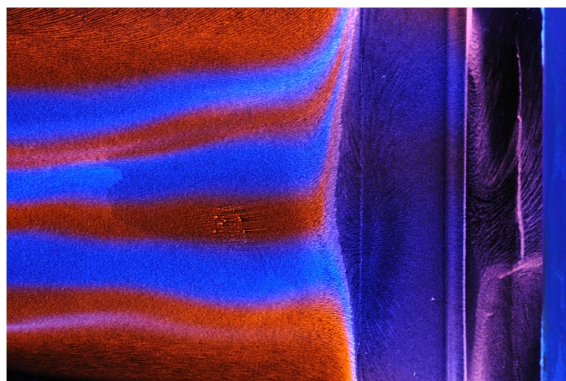
(a)



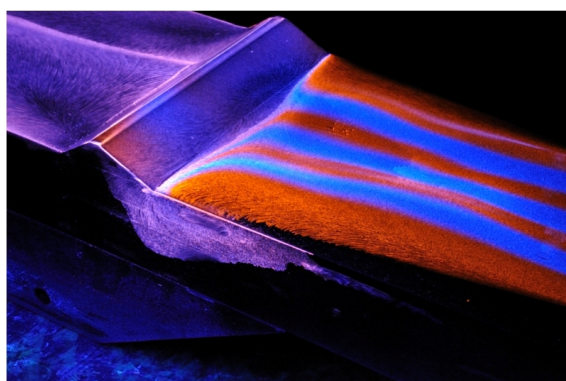
(b)

Figure 4.8. Surface flow test results of *5 Degree 70 MVG* (a) Near view (b) Downstream view.

penetrate the separated region. As indicated by the surface flow pattern in Fig. 4.10(a) the vortices generated are diverted with the rest of the flow. What also is worth mentioning is that while the flow separation is severe, the vortices do seem to maintain their structure. Also comparing Fig 4.9(a) and Fig. 4.10, the MVGs does have some effect on the separated region, but is not strong enough to eliminate. This supports the conclusion by Holden and Babinsky in Section 1.



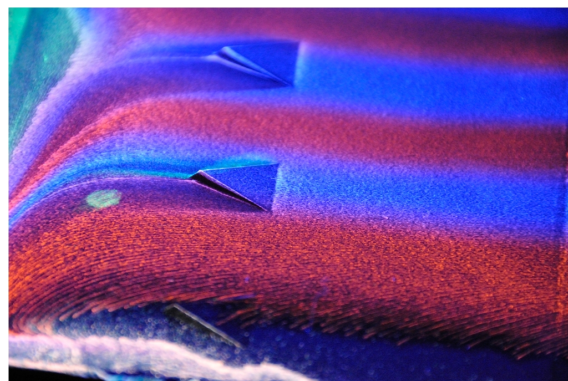
(a)



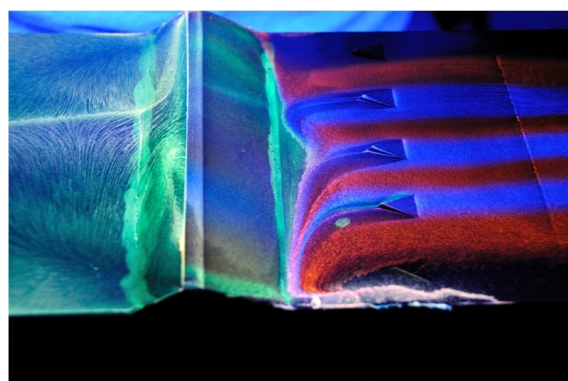
(b)

Figure 4.9. Surface flow test results of *25 Degree No MVG* (a) Top view (b) Side view.

The second additional visualization conducted was with a cylinder. This provided a unique opportunity to understand the effects that MVGs have on a three-dimensional, bow shock/boundary-layer interaction. Figure 4.11(a) is the result of the flat plate cylinder test with no MVGs. For supersonic flow at Mach 2.5, the cylinder displays a well-observed separation line. The large separation zone ahead of the cylinder is clearly seen.



(a)

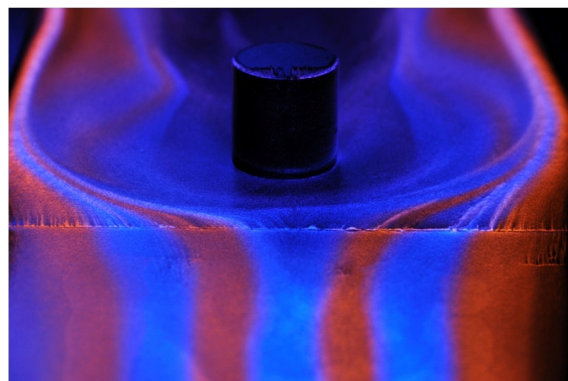


(b)

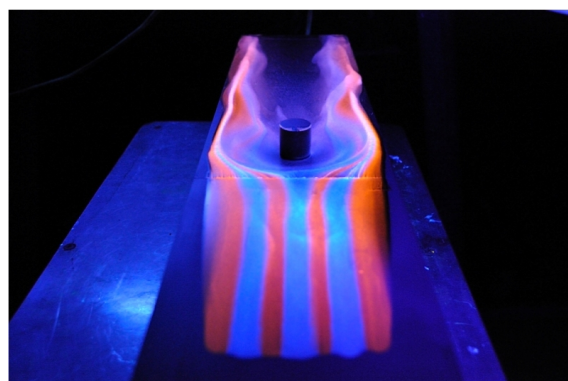
Figure 4.10. Surface flow test results of *25 Degree 45 MVG* (a) Near view (b) Downstream view.

Figure 4.11(b) clearly shows the long-term downstream effect of the cylinder. The surface paint initially approached the cylinder uniformly similar to the flat plate configuration until it encounters the separation region. The surface flow then is deflected toward the outer edges of the flat plate toward the test section walls.

Similar to the other configurations, MVGs were placed ahead of the cylinder in order to understand their effective on the separated region. The center vortex generator in Fig. 4.12(a) shows that the effects of the MVG on the separated region



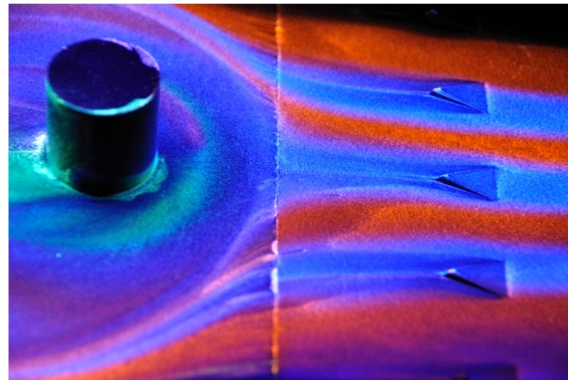
(a)



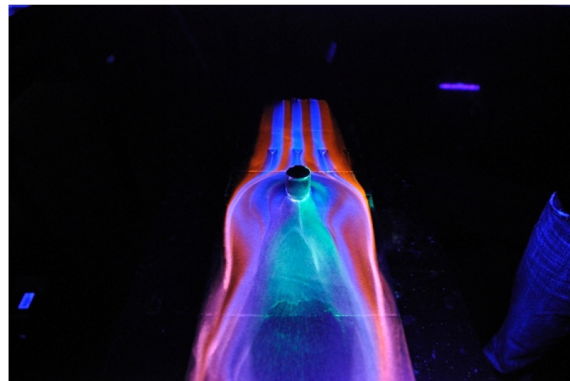
(b)

Figure 4.11. Surface flow test results of *Cyl No MVG* (a) Top view (b) Downstream view.

is minimal. No significant improvements using MVGs were detected. As the central vortices approach the location of the separation line, the surface lines that reveal vortex patterns seem to fade indicating the possibility of instability within the vortex structure. This result is much different than the results concluded with the 25 degree unstart condition. The vortices produced by the outer edge generators show evidence of stability indicated by the trailing center line as it approaches the separated region. Although their effectiveness is similar to the central vortices, unlike the central



(a)

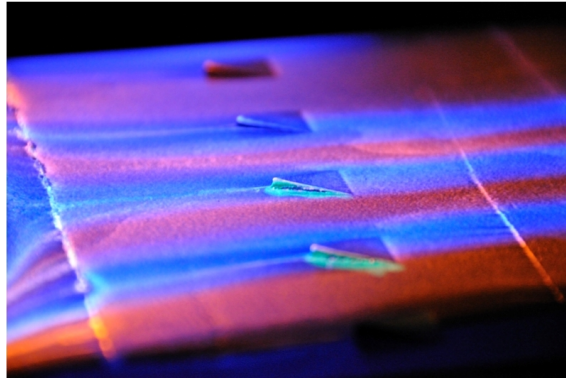


(b)

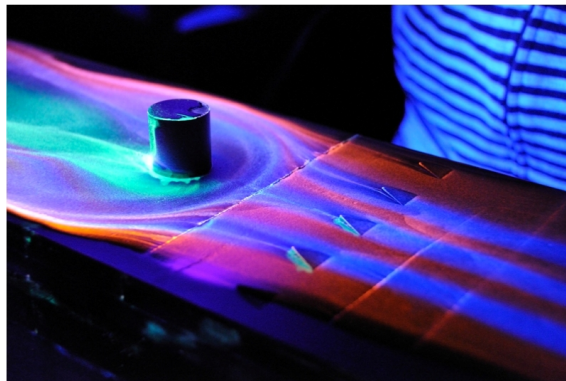
Figure 4.12. Surface flow test results of *Cyl 45 MVG* (a) Near view (b) Downstream view.

vortices, the outer vortices show evidence of following the fluid's path around the separated region similar to the results with the 25 degree ramp.

For this particular MVG configuration, green and red fluorescent paint were added to the region originally left alone by the initial *Cylinder No MVG* configuration. The paints were applied along the intersection of the cylinder and the surface of the plate. The results seen in Fig. 4.12(b), 4.12(a), and 4.13(b) agree well with results of known flow characteristics around a cylinder. Such regions of noticeable



(a)



(b)

Figure 4.13. Surface flow test results of *Cyl 70 MVG* (a) Near view (b) Downstream view.

characteristics include separation seen on the side of the cylinder in Fig. 4.12(a), stagnation line where the two flows merge behind the cylinder, and noticeable vortex filament generated near the back of the cylinder.

Similar to the MVG45 design, comparing the MVG70 configuration to LES results reveals an interesting conclusion. A closer look at the trailing edge of the MVG reveals a similar pattern to the MVG 45 configuration. The swirling pattern in Fig. 4.14(a) indicates that this is a possible location where a vortex filament might

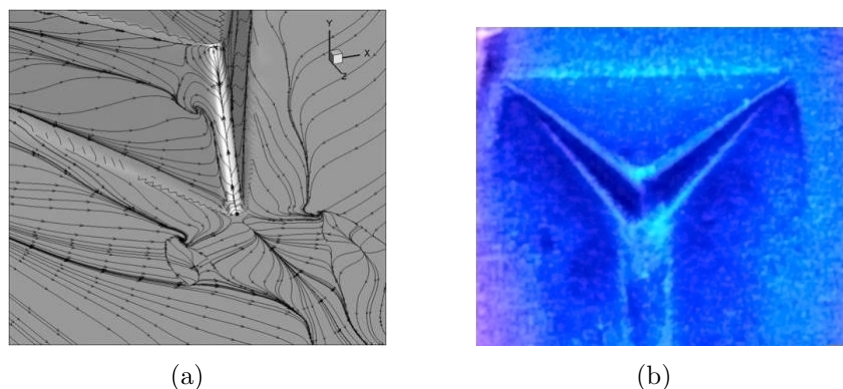


Figure 4.14. MVG 70 surface flow results (a) LES (b) Experimental.

be present. A comparison of the LES results to the experimental one shown in Fig. 4.14(b) shows agreement.

Further, similar to the comparison taken in the MVG45 configuration, a comparison was performed for the MVG70 configuration. Figure 4.15 shows the LES and experimental visualizations. In Fig. 4.15(b) the green color is seen traveling downstream along a line separating the two trailing vortices. While the exact existence of the vortex flow cannot be determined, either side of the green paint indicate the expected vortex flow. A comparison with the LES results show some similarities and differences. The differences were attributed to the low Reynolds number of the LES.

4.1.1.3 Image Manipulation

Further image processing was performed using the DaVis software from LaVision. The video captured from the Nikon camera was imported into DaVis and split

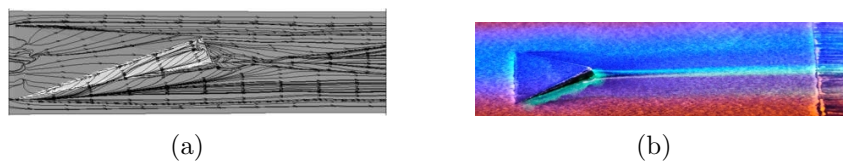


Figure 4.15. MVG70 Top Comparison results (a) LES (b) Experimental.

into individual frames. The number of frames was determined by the software. Once importing was complete, an image manipulation technique was applied. The task involved passing the imported images through a concentration filter. The concentration filter analyzes each individual pixel, finds the local maximum based on the intensity value and concentrates all pixels towards the local maximum [4]. The images were then put through a “non-linear subtract sliding minimum filter.” An example of this image manipulation process is shown in Fig. 4.16.

Comparing the results of Fig. 4.16(b) to Fig. 4.16(a) clearly shows surface flow features not readily detectable in the original image. One example is the line running vertical indicating the point of flow separation which is clearly visible and not affected by the multiple colors. A second example is the recirculating flow pattern directly behind the ramp indicated by the straight vertical line. While the pattern is visible in the original image, the manipulated image shows greater detail. This image manipulation technique was applied to both MVG configuration and compared with LES results.

The first comparison is with the MVG45 ramp shown in Fig. 4.17. The comparison between the three images reveals structures not initially seen. The leading

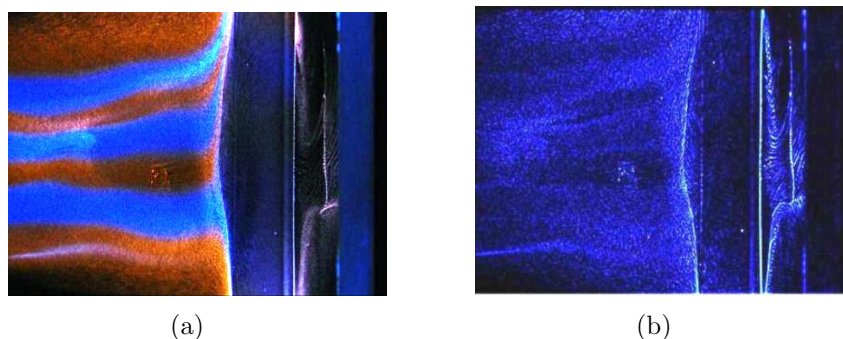


Figure 4.16. Image result after manipulation by the DaVis software (a) Raw image (b) Manipulated.

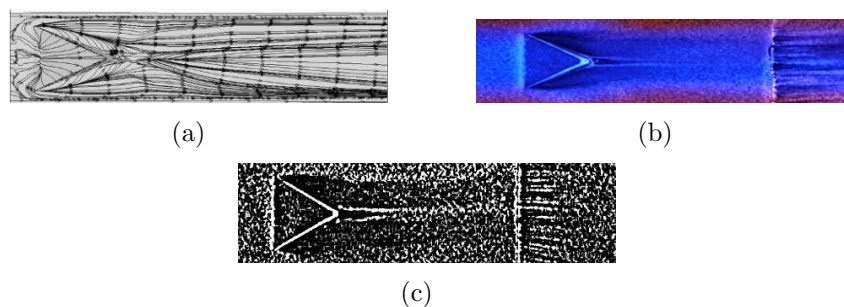


Figure 4.17. Top view comparison of MVG45 (a) LES (b) Raw (c) Manipulated.

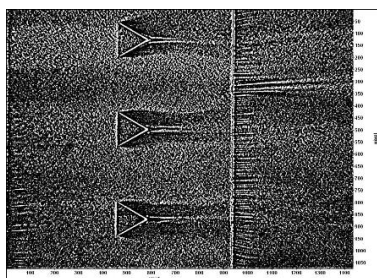


Figure 4.18. Complete top view of manipulated image for MVG45.

edge flow separation is clearly shown in both Fig. 4.17(b) and Fig.4.17(c). The horse-shoe vortex pattern in the surface wake of the MVG are similar. Directly after the ramp in Fig. 4.17(a), there is a small area cone shaped that appears to be the result of a vortex flow impacting the surface. This same area is seen in Fig. 4.17(b) and is located just beyond the trailing edge of the vortex generator. As described previously, LES results revealed what appears to be a possible vertical vortex filament near the trailing edge. After image manipulation, the results clear show to support the existence of such a flow feature.

The large view of the results of the image manipulation technique shown in Fig. 4.20 further support the conclusions stated in the previous paragraph. The consistency with the effect on all vortex generators producing the same features would support the existence of the flow.

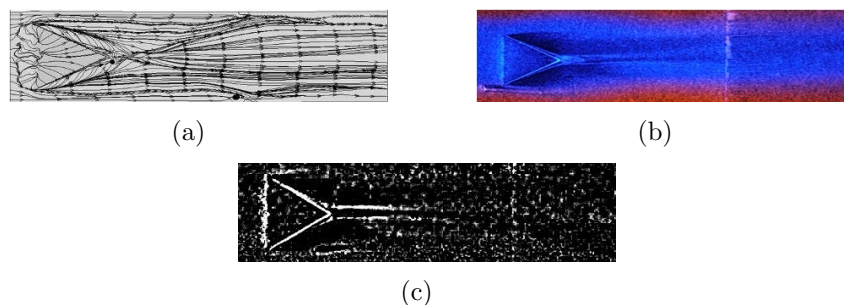


Figure 4.19. Top view comparison of (a) LES (b) Raw (c) Manipulated.

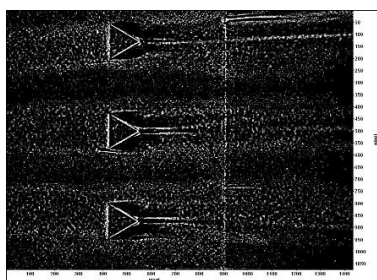


Figure 4.20. Complete top view of manipulated image for MVG70.

The MVG70 configuration revealed similar features after image manipulation was applied. A comparison is shown in Fig. 4.19. Flow features discussed earlier such as leading edge separation, wing-shaped wake features, and areas of high velocity. Closely comparing Fig. 4.19(a) and Fig.4.19(c) indicated the possible existence of vertical vortex filaments. One can conclude that these vortex filaments are inherent with the geometry of the vortex generator and not the trailing ramp angle.

Similar to the process taken with the MVG45 configuration, a wider view reveals that the flows are similar indicated the patterns are repetitive and are a characteristic of the vortex generator. The image manipulation process further supports the findings in the initial comparison of the original images. Flow separation along the leading edge, areas of high flow velocity indicated by the dark colors, the possible existence of vertical vortex filaments all have been shown to exist in LES simulations and experimental surface flow visualizations.

4.2 Particle Image Velocimetry

Particle image velocimetry proceeded according to the test schedule listed in table 4.2.

Table 4.2. PIV Test Schedule

Test	Configuration	MVG	Images to Acquire
1	No	No	≈ 120 Images
4	No	45	≈ 120 Images
7	No	70	≈ 120 Images
13	5° Ramp	No	≈ 120 Images
16	5° Ramp	45	≈ 120 Images
19	5° Ramp	70	≈ 120 Images

4.2.1 Acetone Seeding

During initial testing calcium carbonate was initially used as the seed particle, several images revealed turbulent boundary layer characteristics that are noticeably similar compared to LES results [1]. Most noticeable was the wake of the MVG appeared to show large hump-like structures, see Fig. 4.21(a). However, the PIV system could not reveal any information about this structure.

It was decided that using acetone as the seed may reveal more detail about the turbulent structures. The reference pressure port located on the flat plate upstream from the vortex generators was used to insert the acetone seed into the boundary layer. Since the static pressure inside the test section is sub-atmospheric, the acetone was naturally aspirated into the test section. The acetone droplets were considered to be less than 1 μm in diameter. The actual size of the acetone droplets were not determined, but comparison with the known size of calcium carbonate determined by

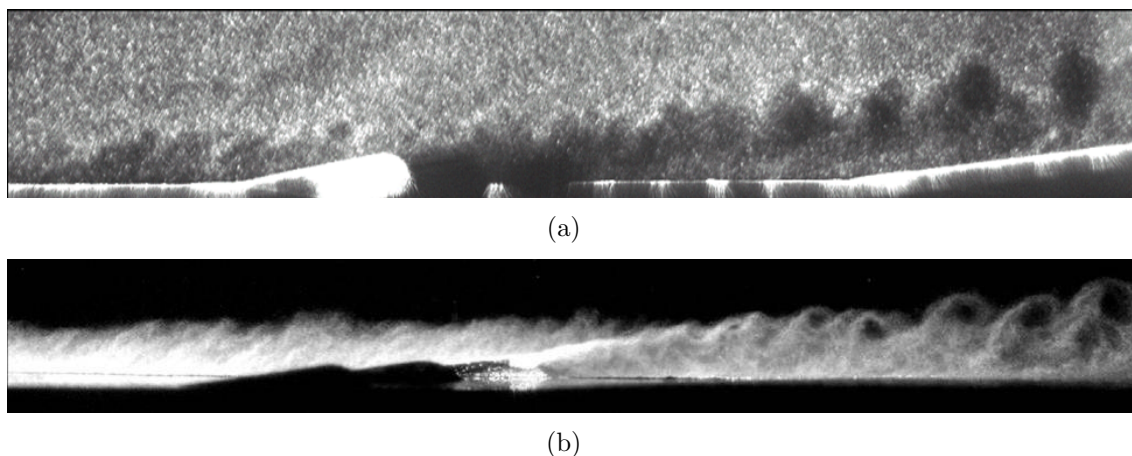


Figure 4.21. Boundary layer visualization with (a) Calcium carbonate, (b) Acetone.

the manufacturer led to this conclusion. Visualizations of the calcium carbonate and acetone seeding are shown in Fig. 4.21.

It is clearly evident that the acetone reveals much more of the flow structure behind the MVG than the calcium carbonate. This is mainly due to the local acetone seeding which provides a high density of scattering particles along with a lower particle relaxation time. Acetone was not seeded in the freestream flow as time constraints prevented the required wind tunnel modification. Therefore, calcium carbonate powder was used to seed the freestream and acetone was used to seed the boundary layer.

4.2.2 Flat Plate

For the purpose of clarification, the images in Appendix B show the average velocity vector image and the ensemble average image profile for the flat plate configuration calculated by DaVis 7.1 software. The averages are calculated by ensembling the average intensity value of each pixel. While the scale is not visible in Fig. A.1(a), the scale is the same as in Fig. A.1(b), therefore the scale in the velocity vector can be used as a reference. An inspection of Fig. A.1(a) shows that the boundary layer is

approximately 5 mm in height. As stated in Section 3.5 the ensemble average profiles upstream of the vortex generators was taken every 5 mm starting with $x = -5\text{mm}$.

Comparing Fig. 4.22 with Fig. 3.18 it appears that the wake region deviates from the law of the wall around $y^+ = 500$ when theory deviate around $y^+ = 300$. Even though the profile deviates at this location, the calculated profiles do in fact converge onto each other as expected. Further analysis given in Table 4.3 show that the boundary layer thickness profile agree well with observations. One noticeable difference between the *Flat Plate No MVG* configuration and other configuration is the frictional velocity. The values for the friction velocity were particularly higher in this configuration. The exact cause of this result is unknown at this time.

For configurations *Flat Plate 45 MVG* and *Flat Plate 70 MVG*, the results agree well with theory and also agree converges onto each other as expected. Good agreement with theory and convergence of the profile signify reliable data technique. Agreement of profiles also verifies the flow is turbulent. This was further verified

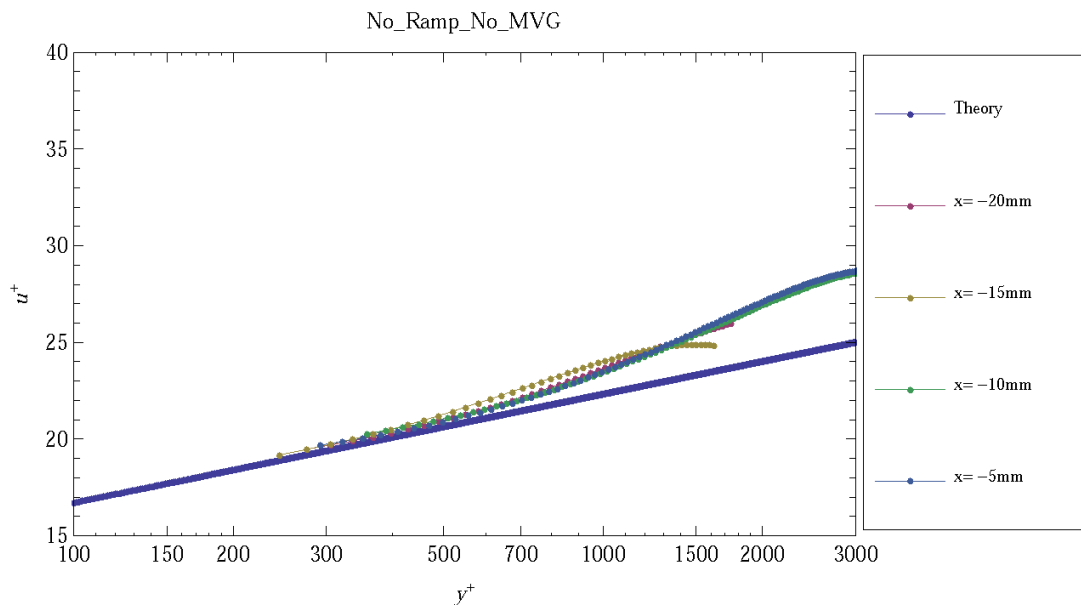


Figure 4.22. Turbulent boundary layer profile for *No Ramp No MVG* configuration.

Table 4.3. Calculation Results for *Flat Plate No MVG*

x (mm)	u_τ (m/s)	δ (mm) ^c	Π	C_f	θ (m)	$Re_{\theta 2_{aw}}$	δ^* (m)	Re_{δ^*}
-20	17.4	3.2	0.56	0.0020	0.00033	5445	0.00068	11042
-15	17.4	3.2	0.56	0.0020	0.00031	5127	0.00076	12373
-10	17	4.9	0.56	0.0019	0.00061	10045	0.00083	13595
-5	16.6	4.9	0.56	0.0018	0.00066	10829	0.00113	18468

Table 4.4. Calculation Results for *Flat Plate 45 MVG*

x (mm)	u_τ (m/s)	δ (mm) ^c	Π	C_f	θ (m)	$Re_{\theta 2_{aw}}$	δ^* (m)	Re_{δ^*}
-15	14.7	5.0	0.56	0.0014	0.00064	10568	0.00094	15654
-10	15.2	4.8	0.56	0.0015	0.00056	9384	0.00070	11652
-5	14.9	4.3	0.56	0.0014	0.00057	9493	0.0087	14389

by the PIV images collected. Upon the flow reaching the ramp, it is expected that an oblique shock will form. However, it appears that no oblique shock is present in any of the PIV images thus indicating the oblique shock is weak. As the flow passes the ramp of the vortex generator an expansion wave is created and can be seen in Fig.A.2(a) and A.3(a). Further downstream the boundary layer thickness appears to increase to a range of 7 mm to 8 mm. Although the thickening of the boundary layer is a direct cause of the influence of the MVG, the evidence of vortices cannot be determined. If the boundary layer profile is indeed increasing, then changes in the boundary layer properties such a density will be affected. Schlieren testing will detect such changes as well as verify the thickness increase.

4.3 5 Degree Ramp

The 5 degree ramp results is shown in Fig. 4.25. For the *5 Deg No MVG* configuration, the boundary layer analysis was performed on a total of five profile locations. This reason for this modification was mainly due to the uncertainty of the zero x location. For the other 5 degree configurations the zero x location is defined

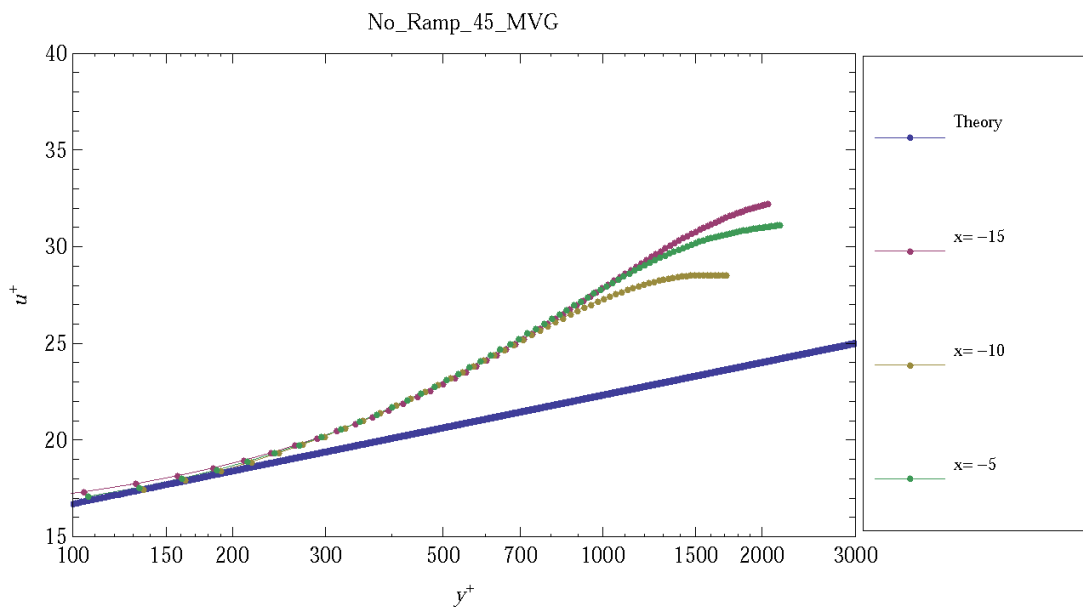


Figure 4.23. Turbulent boundary layer profile for *No Ramp MVG 45* configuration.

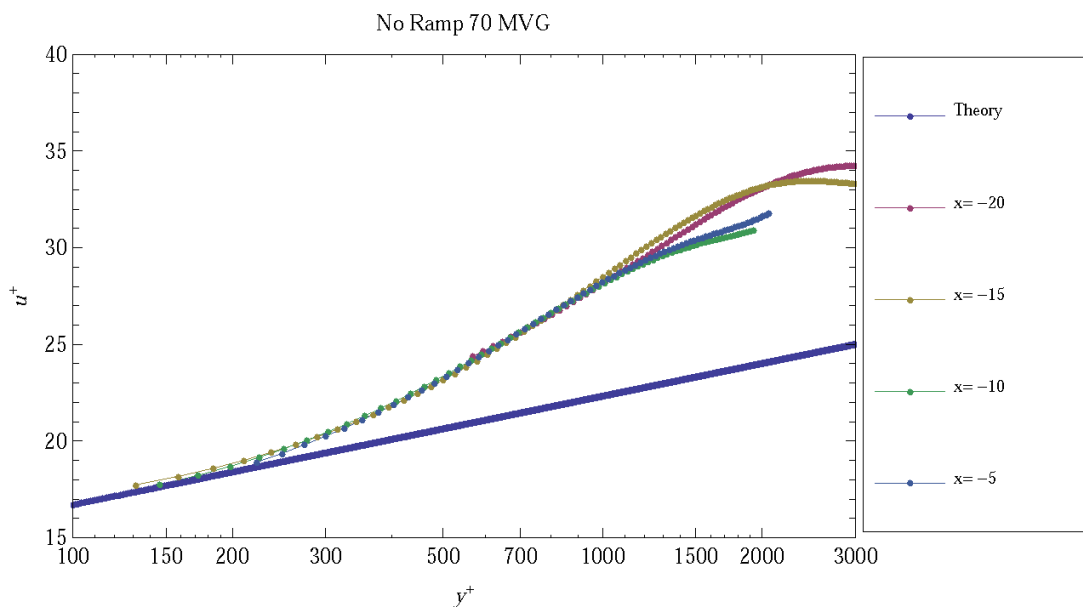


Figure 4.24. Turbulent boundary layer profile for *No Ramp 70 MVG* configuration.

by the leading edge of the MVG ramp. For the *Flat Plate 5 Degree* configuration, no such location can be verified. Therefore taking more profiles than normal would

Table 4.5. Calculation Results for *Flat Plate 70 MVG*

x (mm)	u_τ (m/s)	δ (mm) ^c	Π	C_f	θ (m)	$Re_{\theta_{2aw}}$	δ^* (m)	Re_{δ^*}
-20	14.5	5.0	0.56	0.0013	0.00058	9710	0.00061	10162
-15	14.7	5.0	0.56	0.0014	0.00066	10983	0.00061	10058
-10	14.6	4.0	0.56	0.0014	0.00051	8533	0.00073	12081
-5	14.5	4.2	0.56	0.0013	0.00048	7933	0.00062	10365

ensure a reliable conclusion over a larger range. The results of the analysis is given in Fig. 4.25 and Table 4.6. For the results listed in Table 4.3, the average frictional velocity was calculated to be 14.7 m/s, average boundary layer height was is 3.8 mm, and average coefficient of friction was 0.0015. The momentum thickness and displacement thickness maintained similar results with some minor exceptions.

For the MVG45 and MVG70 configurations, the results are given in Fig. A.5 and Fig. A.6. The calculation results are given in Tables 4.7 and Table 4.8. Similar

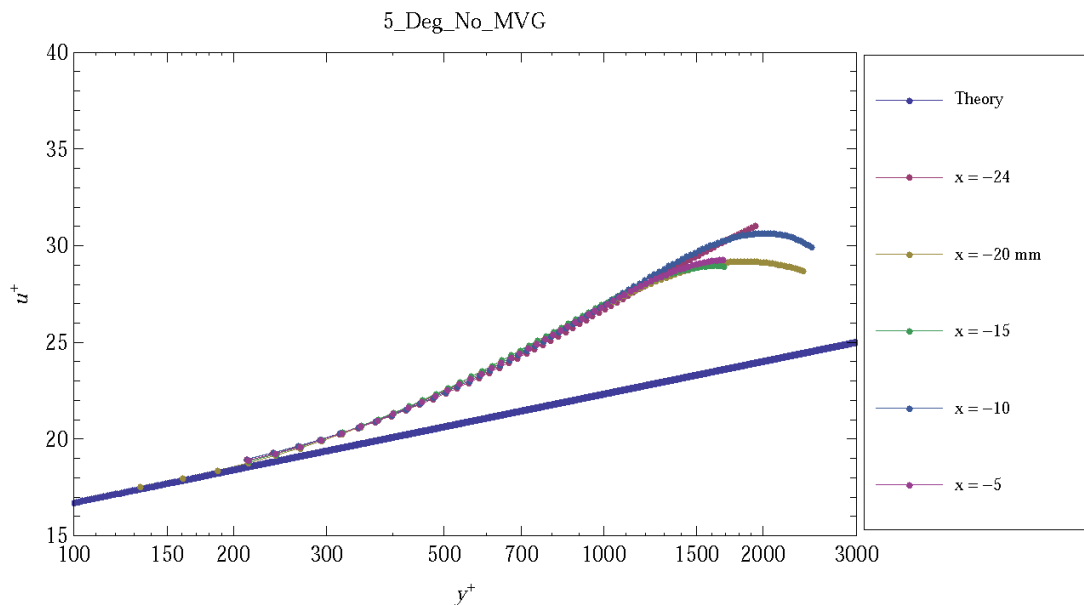
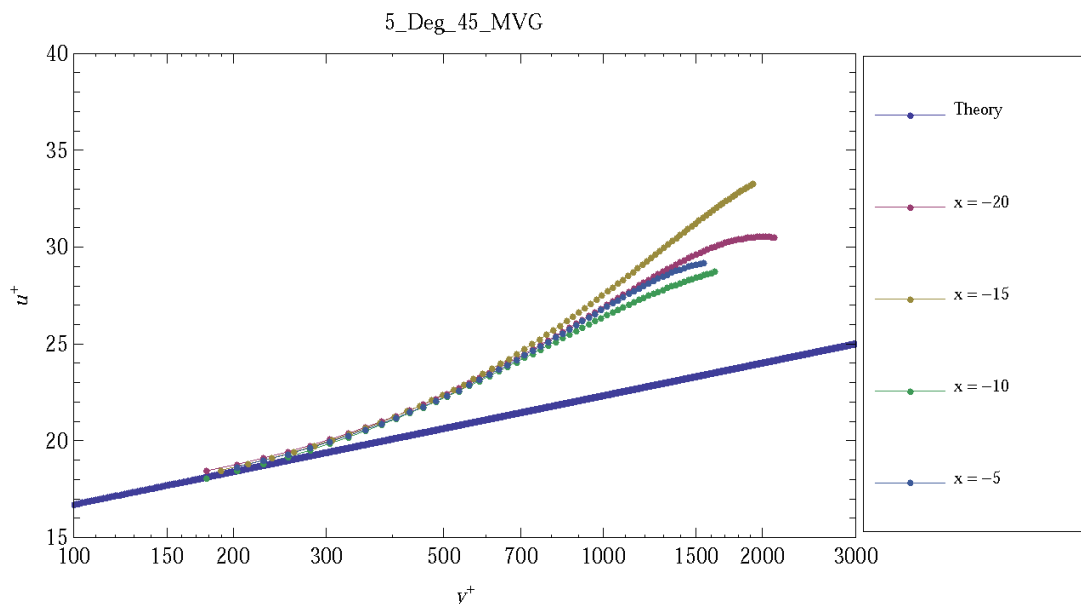


Figure 4.25. Turbulent boundary layer profile for *5 Degree Ramp No MVG* configuration.

Table 4.6. Calculation Results for *5 Deg No MVG*

x (mm)	u_τ (m/s)	δ (mm) ^c	Π	C_f	θ (m)	$Re_{\theta_{2\alpha w}}$	δ^* (m)	Re_{δ^*}
-24s	14.6	4.4	0.56	0.0014	0.00048	8077	0.00039	6676
-20	14.7	3.7	0.56	0.0014	0.00051	855	0.0013	21989
-15	14.8	3.5	0.56	0.0014	0.00042	7078	0.0010	17500
-10	14.6	3.9	0.56	0.0014	0.00049	8315	0.0010	17867
-5	14.7	3.5	0.56	0.0014	0.00044	7517	0.0010	18279

Figure 4.26. Turbulent boundary layer profile for the *5 Degree Ramp 45 MVG* configuration.

the results of the *5 Deg No MVG* configuration, the average frictional velocity for the *5 Deg 45 MVG* configuration was 14.75 m/s, the average boundary layer height was 3.7 mm, the average coefficient of friction was 0.0014. The results of the *5 Deg 70 MVG* configuration calculated an average frictional velocity of 14.7 m/s, average boundary layer height of 3.2 mm, and average coefficient of friction of 0.0014. All three configurations agree well with each other with the exception of the momentum and displacement thicknesses which may be due to uncertainty error.

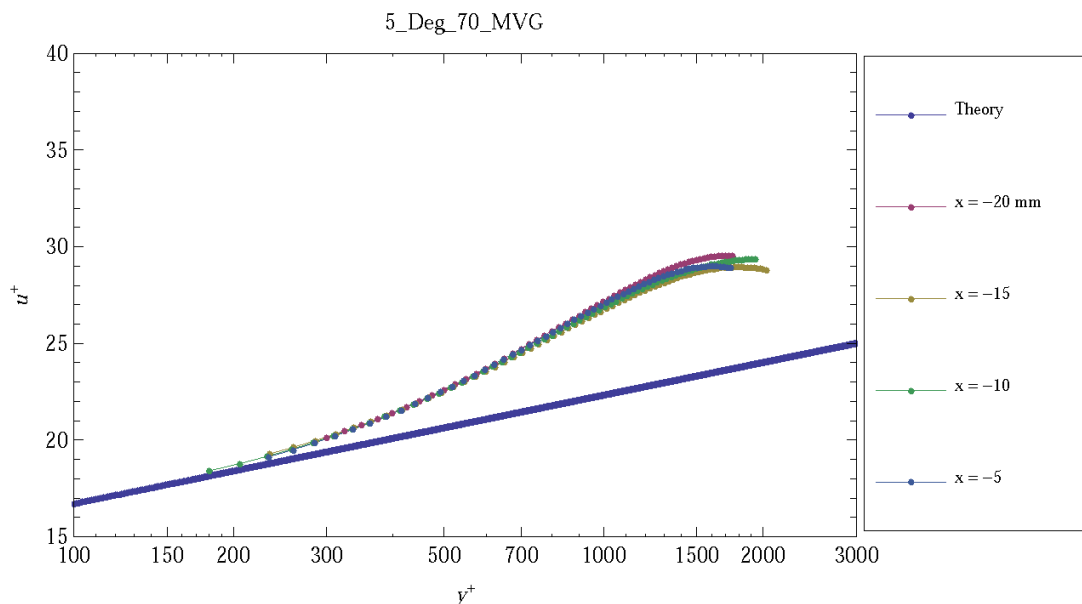


Figure 4.27. Turbulent boundary layer profile for the *5 Degree Ramp 70 MVG* configuration.

Table 4.7. Calculation Results for the *5 Deg 45 MVG* configuration.

x (mm)	u_τ (m/s)	δ (mm) ^c	Π	C_f	θ (m)	$Re_{\theta 2_{aw}}$	δ^* (m)	Re_{δ^*}
-20	15	3.5	0.56	0.0014	0.00050	7471	0.0010	15858
-15	14	4.3	0.56	0.0013	0.00054	8568	0.0007	11530
-10	15	3.2	0.56	0.0014	0.00052	8136	0.0012	19623
-5	15	3.8	0.56	0.0014	0.0043	6854	0.0010	15910

Table 4.8. Calculation Results for the *5 Deg 70 MVG* configuration.

x (mm)	u_τ (m/s)	δ (mm) ^c	Π	C_f	θ (m)	$Re_{\theta 2_{aw}}$	δ^* (m)	Re_{δ^*}
-20	14	3.2	0.56	0.0013	0.00046	7454	0.0011	18402
-15	14	3.33	0.56	0.0014	0.00047	7636	0.0011	18544
-10	14	3.21	0.56	0.0014	0.00053	8652	0.0013	21365
-5	14	3.2	0.56	0.0014	0.00041	6757	0.0010	16174

For the calculated results, the boundary layer profiles only extend down to $y^+ = 200$. Unfortunately, the data collected by the PIV system was not reliable

below this value for most cases. The cause for this was the unintentional side-effect of aspirating acetone into the test section. When acetone entered into the test section it entered as a liquid. At the surface the acetone concentration was high. This was evident by the stripping of the paint at the surface. This unfortunate side effect at the surface led to inaccuracies in the boundary layer calculation proceeding toward the inner variables. This source of error in the calculation was determined to originate with the kinematic viscosity. For the inner layer calculations the u^+ and y^+ are calculated according to Eqs.(3.6) and (3.7). When u^+ and y^+ were calculated using the kinematic viscosity of air, the values did not agree well with theory, however, the resulting profile did reveal the linear characteristic seen in theory. Replacing the kinematic viscosity of air with that of acetone, the results again did not agree with theory, but were more accurate than the results with air. Taking the average of the kinematic viscosity between air and acetone, the results were found to agree with theory. While performing the inner variables with this value is not practical, the conclusion would suggest that data taken at the area very near the surface was either over saturated with acetone seed or was corrupted by the stripping of the paint. As a result, values below $y^+ = 200$ were disregarded and were not considered reliable in most cases.

4.4 Schlieren Imaging

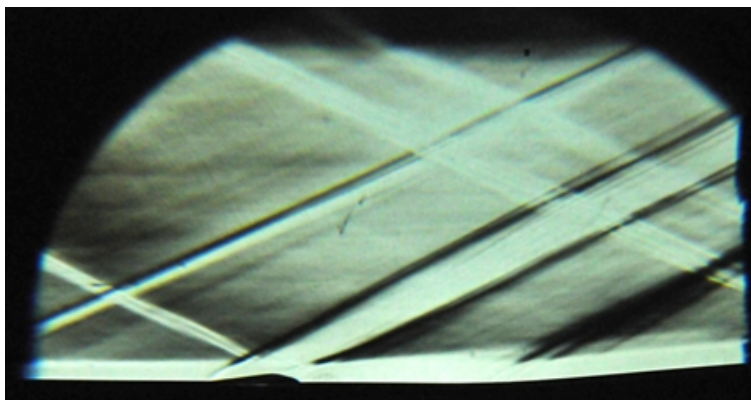
The third type of test conducted in this study involved schlieren imaging, which can provide details about flow characteristics including shock and expansion waves, density gradients, verification of test section start conditions, and the overall effect of MVGs on the boundary layer. Schlieren images conducted in this study will help verify the data and results conducted by the other experiments conducted in this study.

Table 4.9. Schlieren Test Schedule

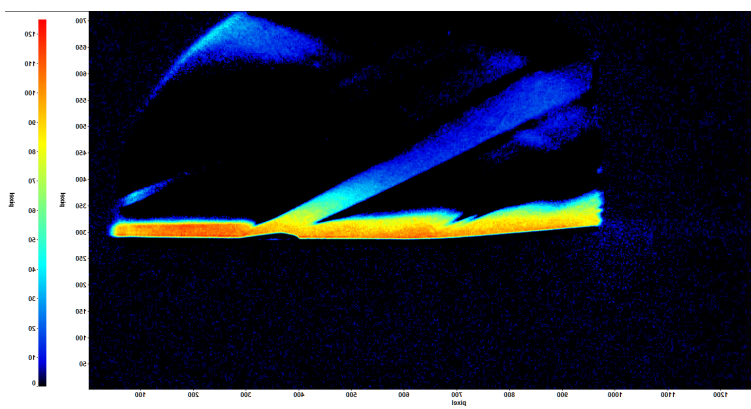
Test	Configuration	MVG	Data to Collect
2a	Flat	Flat	Video
2a	Flat	Flat	Image
6a	Flat	45	Video
6b	Flat	45	Image
9a	Flat	70	Video
9a	Flat	70	Image
14a	5° Ramp	Flat	Video
14b	5° Ramp	Flat	Image
18a	5° Ramp	45	Video
18b	5° Ramp	45	Image
21a	5° Ramp	70	Video
21b	5° Ramp	70	Image

Image subtraction was performed on the video using the DaVis software. The videos collected were first imported in the same manner as the surface flow visualization videos. The video was split automatically by the DaVis software into individual frames. One video frame before the run was selected as the reference frame. This frame was then subtracted from all other frames collected. Performing image subtraction allowed optical distortions in the optical path to be removed as well as sharpened density gradients as a result of flow properties. The value of the density gradient itself could not be determined. However, the severity of the density gradients are determined by the intensity contrast of each pixel and the image subtraction intensities value of each pixel from the reference frame. The results of the calculations were then color-coded on a max-min color scale.

Figures 4.28(a) and 4.28(b) show the results of the image subtraction process compared to the original. Flow direction in the images is from left to right. One important piece of information obtained from schlieren image is the Mach number verification. Using isentropic relationships the Mach number can be found based on



(a)



(b)

Figure 4.28. Typical results for image subtraction using DaVis 7.1 (a) Schlieren (b) Image subtraction.

the Mach angle. For a Mach number of 2.4–2.5, the Mach angle should be approximately 24.6° to 23.5° . Figure 4.29 shows the *5 Degree 45 MVG* configuration with the Mach angle measured to be 24.62° and 27.81° with a ramp angle of 5° . This confirms the freestream Mach number is approximately 2.4. While the nozzle of the wind tunnel was configured with a throat to area ratio for Mach 2.5, it is important to note that the calculations do not take into consideration viscous losses. Therefore,

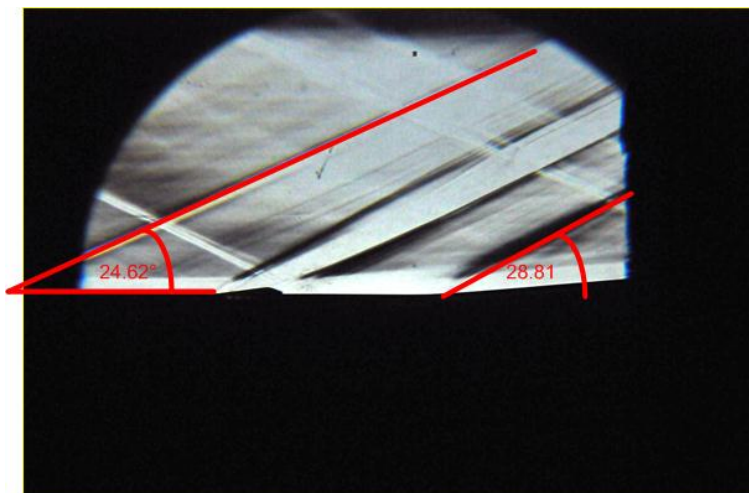


Figure 4.29. Results of the measure Mach angle.

the Mach number of 2.4 for the testing conducted is a reasonable result considering the type of wind tunnel used. Image results for schlieren testing can be found in Appendix B.

4.4.1 Flat Plate

The first test conducted was the *No Ramp No MVG* configuration. Figure A.7 show the results of the schlieren test and Davis image. Due to the lack of coordinate scaling, an exact estimate of the boundary layer height is difficult to obtain from Fig. A.7. However, a reference height can be taken from Fig. A.8 where the height of the MVG is measured to be 2 mm (0.078 in.). Using this to determine rough estimate of the boundary layer thickness, the density gradient seen in Fig. A.7(a) approximately 4 mm (0.15 in.). This confirms the result collected from the PIV ensemble average profile. As stated earlier, the data collected for the *Flat Plate No MVG* configuration did not include a reference image. As a result the image subtraction could not be performed for this configuration. The DaVis 7.1 software can still take the images and apply a color scale. This will result in software manipulated color schlieren. Choosing the right color scale clarifies the intensity of the density gradient. Figure A.7(b) is

the result of Fig. A.7(a) converting the color scale to a scale defined by the user. The image is a good example of color Schieren through software manipulation.

Analysis of the *No Ramp 45 MVG* and *No Ramp 70 MVG* configurations yielded different results from the simple flat plate configuration. Figure A.8(a) shows the existence of an oblique shock generated by the MVG. The results of this image further confirms the conclusion from Section 4.2 that an oblique shock is being produced by the leading edge and is considered to be a weak shock. Review of the ensemble average image and comparing to the schlieren image also confirms the expansion generated by the MVG. Further downstream of the MVG's, both the schlieren image and image subtraction show an increase in the boundary layer thickness from 4 mm to 7.5 mm. The density gradient increase in the boundary layer does not seem as strong as the original boundary layer, but this could be the result of the image being the total sum of density gradients that occur across the surface of the flat plate. The 70 degree MVG configuration seen in Fig. A.9(a) revealed similar results as the 45 MVG configuration.

4.4.2 5 Degree Ramp

The images collected from the 5 degree ramp configuration show a well-defined boundary layer. Figure A.10 reveals the results of the schlieren image and the image subtraction. Similar to the flat plate configuration, the boundary layer height is approximately 4 mm. As expected with a 5 degree ramp, an oblique shock is generated from the leading edge. Closer analysis of the ramp concludes that the shock created is also a weak shock. No separation is detected at the edge of the ramp angle. This conclusion is supported by the surface flow analysis performed in Section 4.1 where small separation is visible. The image subtraction results for this configuration yield expected results for a smooth boundary layer with a 5 degree ramp.

For the MVG 45 and 70 with 5 degree configurations, the MVGs do influence the boundary layer height. Comparing the results with the flat plate configuration, the 5 degree ramp appears to have no affect on the stability of the flow influenced by the MVG. This could be a good indication suggesting the vortices generated by the MVGs are stable. It is worth mentioning that even though the shock generated by the 5 degree ramp is weak, the disturbance generated by the MVGs seem not to be affected by the ramps influence. Comparing the results to the image subtraction, the intensity of the density gradients yields similar values before and after the ramp concluding that the ramp has little effect on the disturbance the MVG causes. It must be mentioned that the color scale is set by the intensity of pixel. While the scale may not change from configuration to configuration, there is a possibility that the images collected may have minor differences in pixel value from the original images.

CHAPTER 5

CONCLUSION

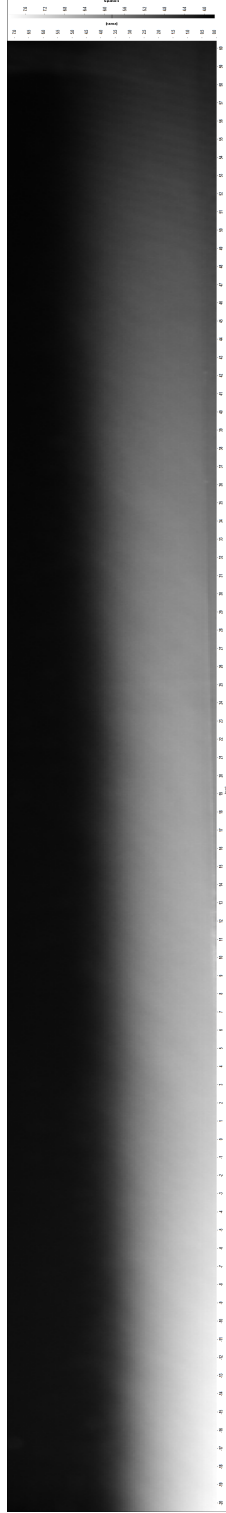
For the surface flow analysis the technique of introducing the combination ultraviolet light surface flow paint and surface preparation proved to be a valuable technique providing more detailed information about the surface flow characteristic than conventional surface flow methods. The result of the test concluded the addition of the MVGs yield similar surface characteristics seen in the LES results. Areas of high velocity flows, flow separation, and vortex filaments were detected and confirmed by both experiments. The 25 degree ramp and the cylinder test provide an unique opportunity to understand the effects of MVG on unstart conditions and on different geometrical shapes. For the 5 degree ramp the results agree well with the LES results. Importing the result into the DaVis 7.1 software and performing image manipulation revealed more detail about the surface flow characteristics than the original images. This was mainly due to the filter and manipulation process performed by the software. The results further supported these conclusion.

PIV testing was able to reveal not just a quantitative analysis, but was able to reveal the complex flow structures downstream of the MVGs. The PIV data collected provide the opportunity for boundary layer analysis to be performed on the incoming boundary layer profile. Unfortunately the data collected close to the surface could not be considered reliable due to the combination of acetone seeding and surface paint interaction. Therefore the data collected below y^+ was considered questionable. For the analysis performed the incoming profile agree well with theory with the exception

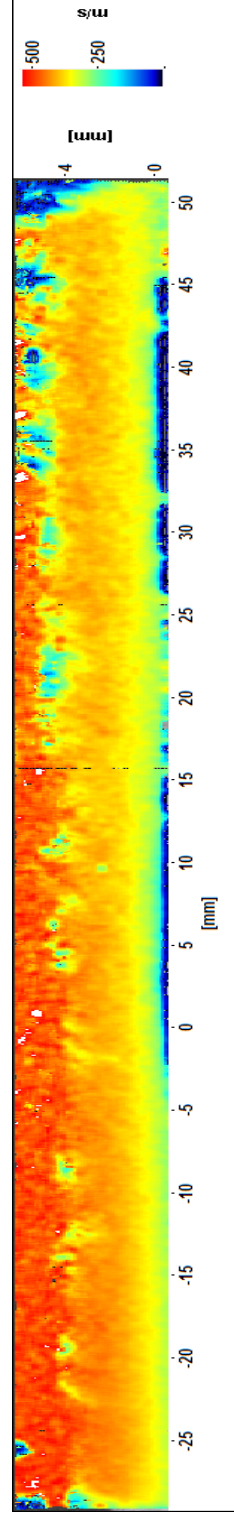
of the flat plate configuration. While the data reveal a wake deviation at $y^+ 500$, the profiles collected did converge onto itself.

The schlieren technique proved to be beneficial in data verification and analysis. The data obtain verified the boundary layer thickness seen in the PIV images, verified the Mach number of the test section, and concluded the MVG effect the boundary layer in both height and density. The *No Ramp 5 Degree* configuration provide a well define boundary layer to compare to the effects of the MVGs. The *5 Degree* ramp image subtraction provide evidence that the disturbances caused by the MVG will hold against weak shock. While this may not be very significant, it does prove that the vortex generated has some stability to it as it is not affected by the weak shock or the ramp itself.

APPENDIX A
PIV AND SCHLIEREN RESULTS



(a)



(b)

Figure A.1. *No Ramp No MVG* configuration: (a) Average PIV Image, (b) calculated average vector field.

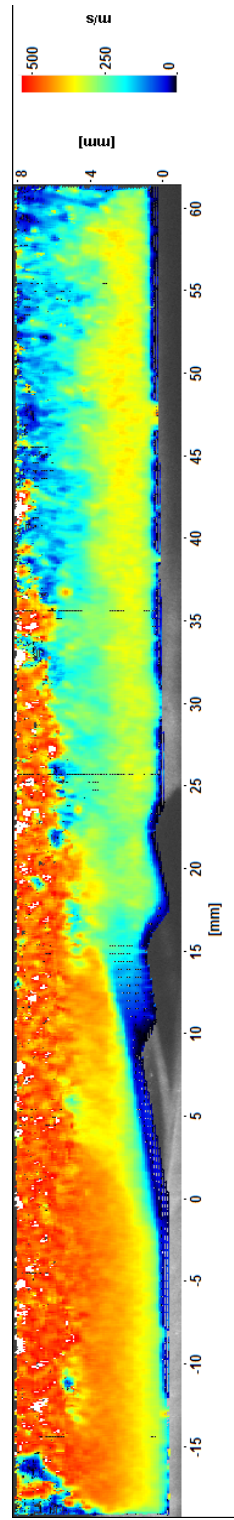
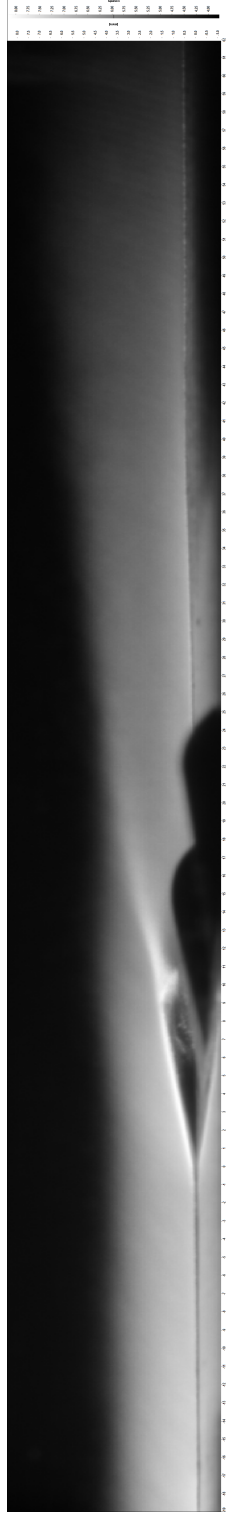


Figure A.2. *No Ramp 4.5 MVG* configuration. (a) Average PIV Image, (b) Calculated average vector field.

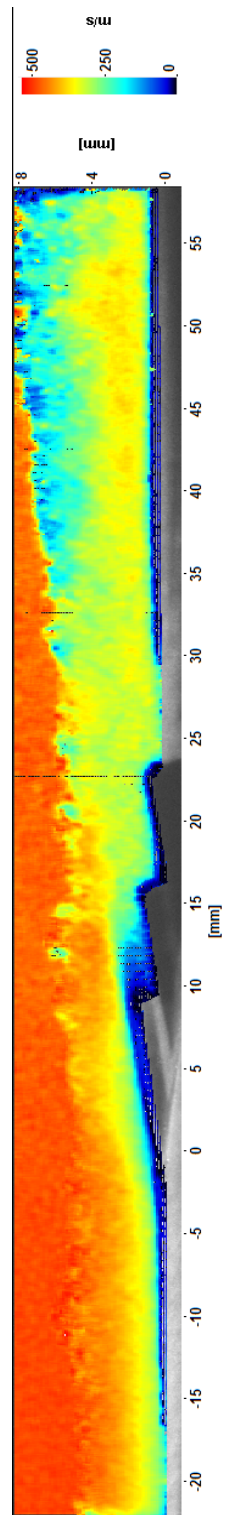
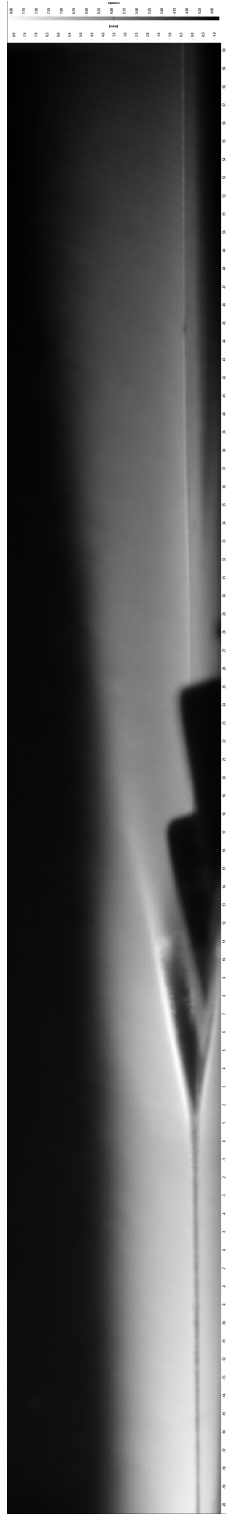
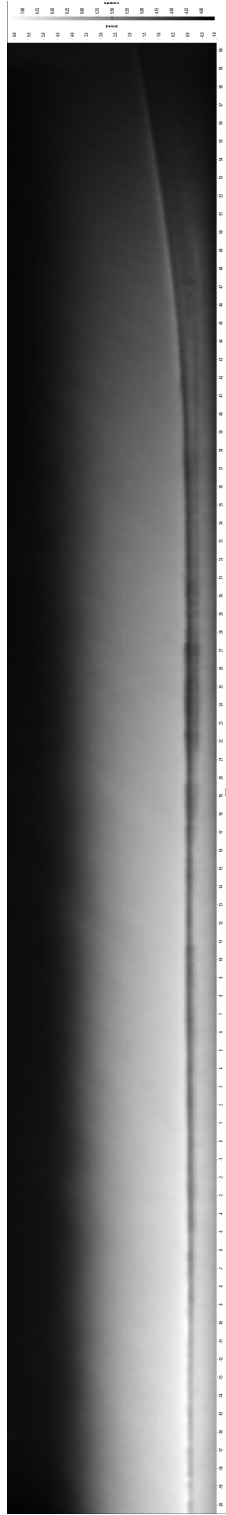
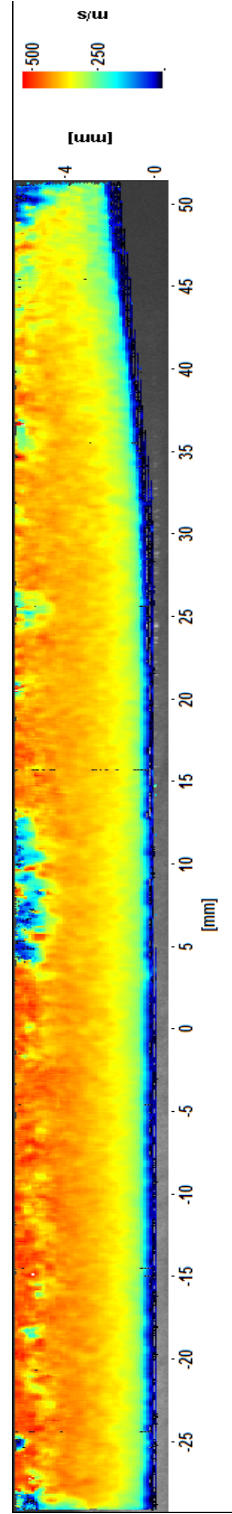


Figure A.3. *No Ramp 70 MVG* configuration. (a) Average PIV Image, (b) Calculated average vector field

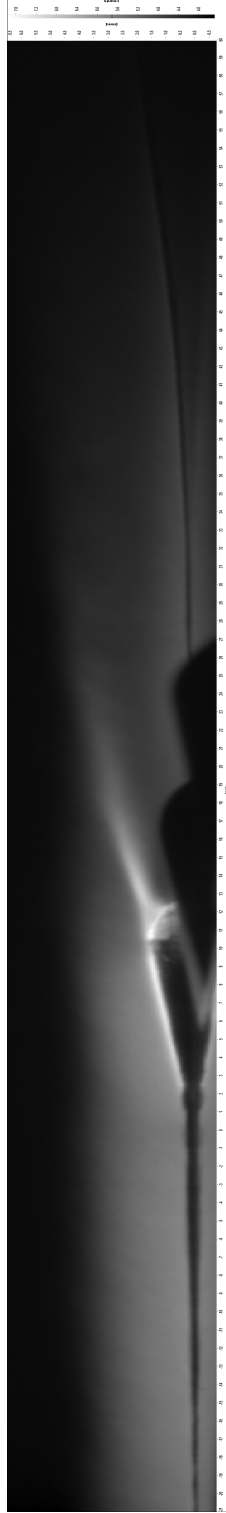


(a)

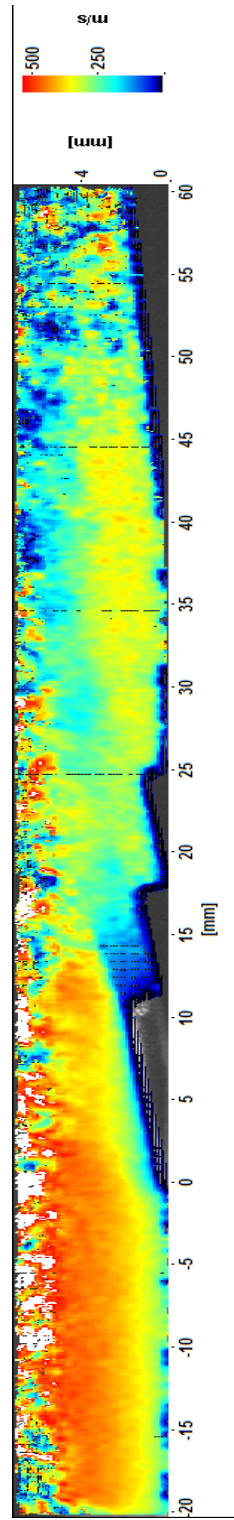


(b)

Figure A.4. 5 Deg No MVG configuration (a) Average PIV Image, (b) Calculated average vector field

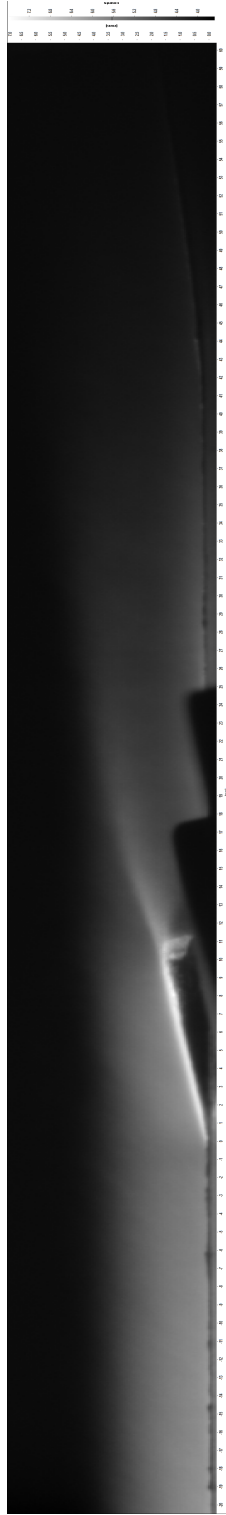


(a)

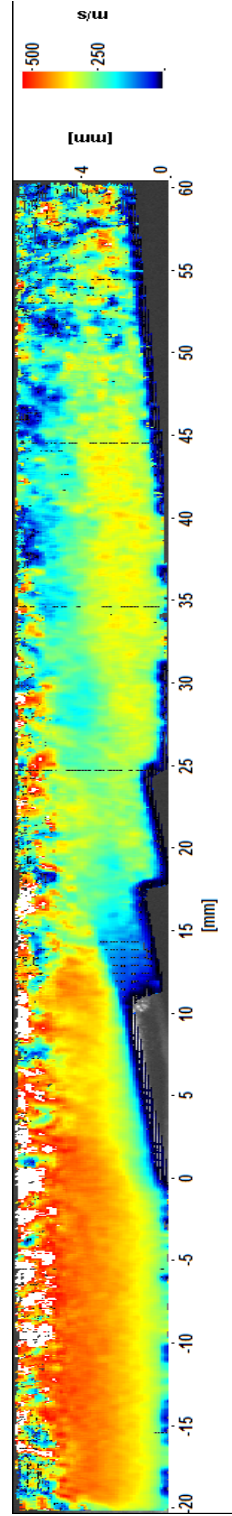


(b)

Figure A.5. 5 Deg 45 MVG configuration (a) Average PIV Image, (b) Calculated average vector field

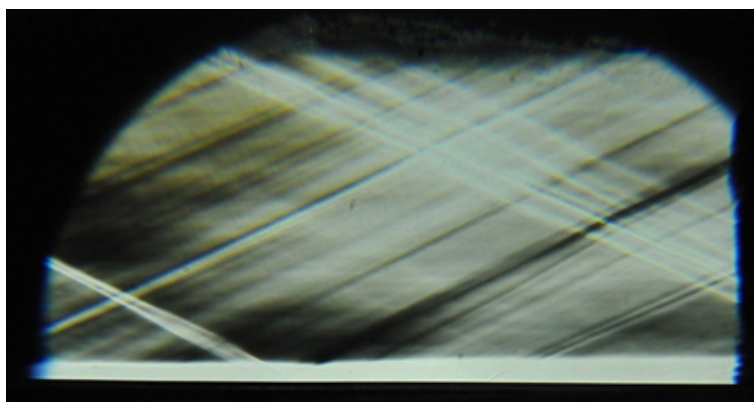


(a)

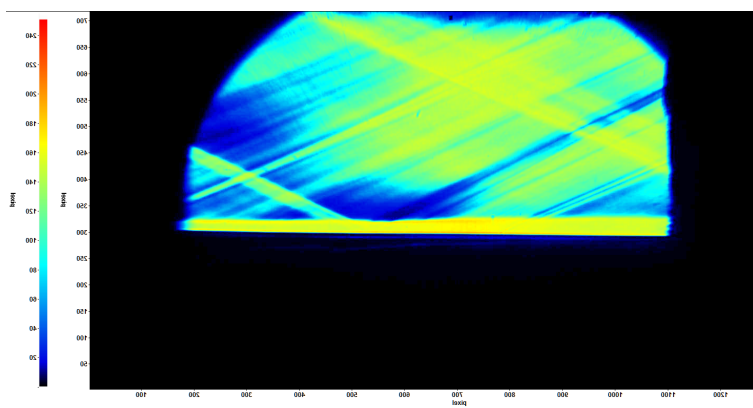


(b)

Figure A.6. 5 Deg 70 MVG configuration (a) Average PIV Image, (b) Calculated average vector field.

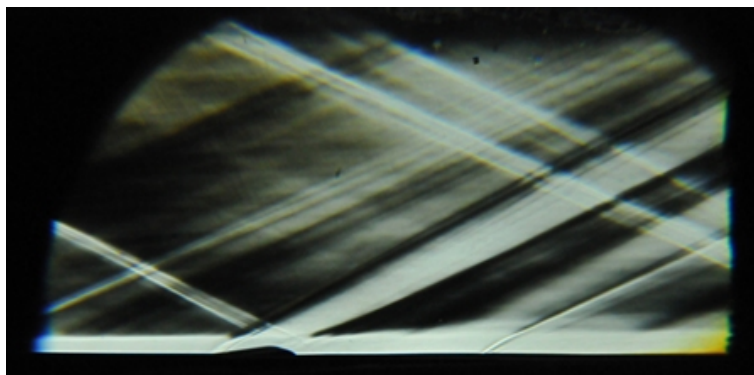


(a)

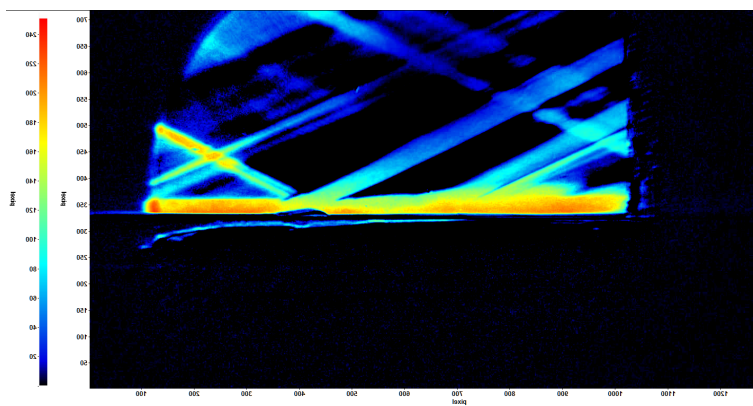


(b)

Figure A.7. *No Ramp No MVG* configuration for (a) Schlieren and (b) Color schlieren image.

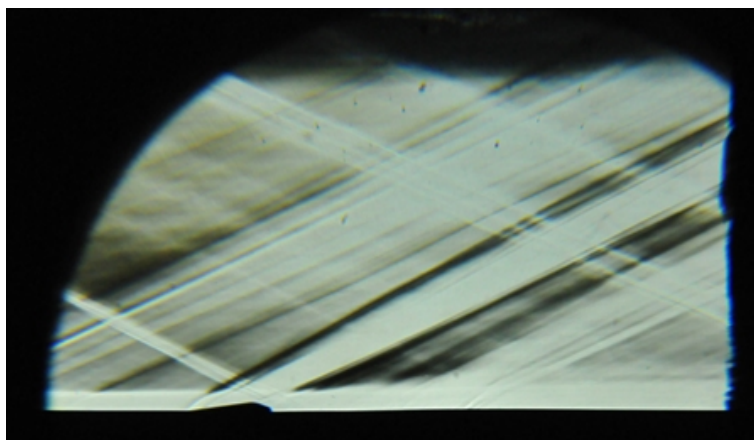


(a)

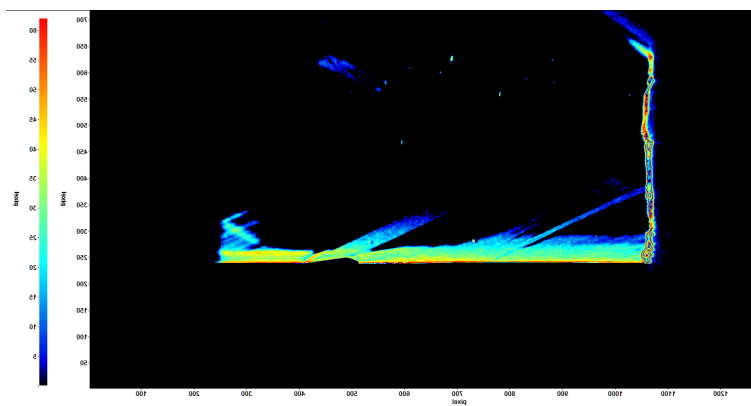


(b)

Figure A.8. *No Ramp 45 MVG* configuration for (a) Schlieren and (b) Image Subtraction.

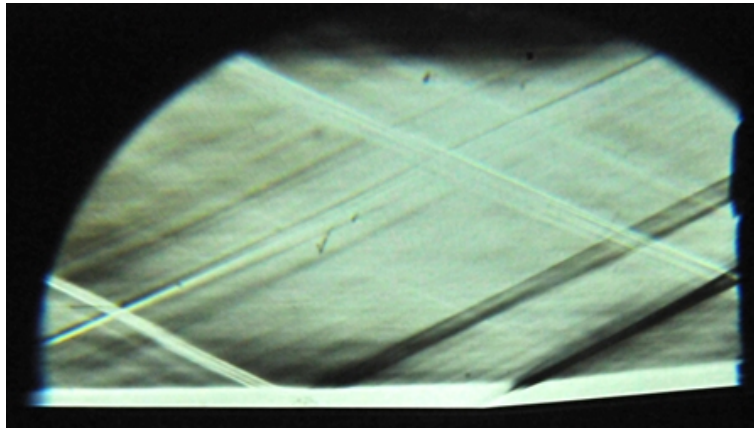


(a)

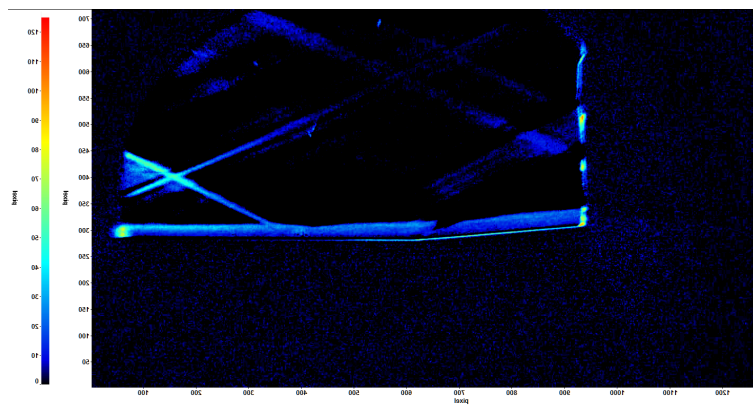


(b)

Figure A.9. *No Ramp 70 MVG* configuration for (a) Schlieren and (b) Image Subtraction.

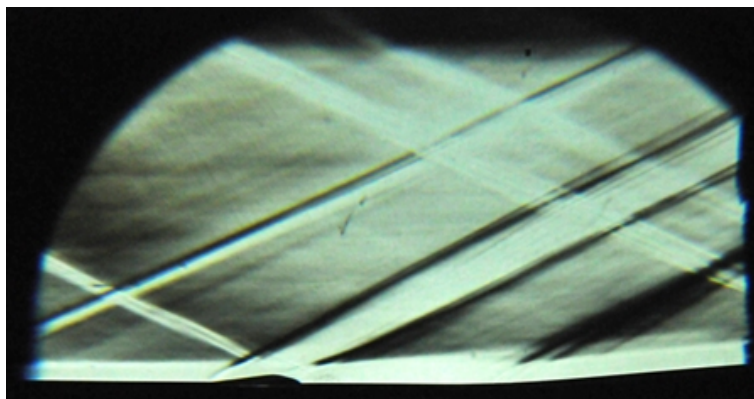


(a)

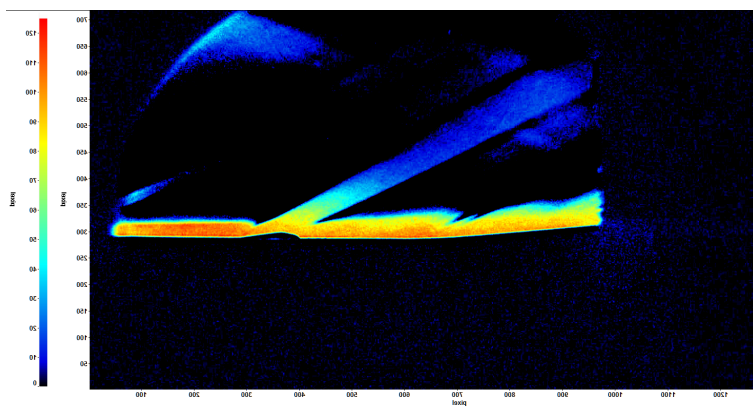


(b)

Figure A.10. *5 Deg No MVG* configuration for (a) Schlieren and (b) Image Subtraction.

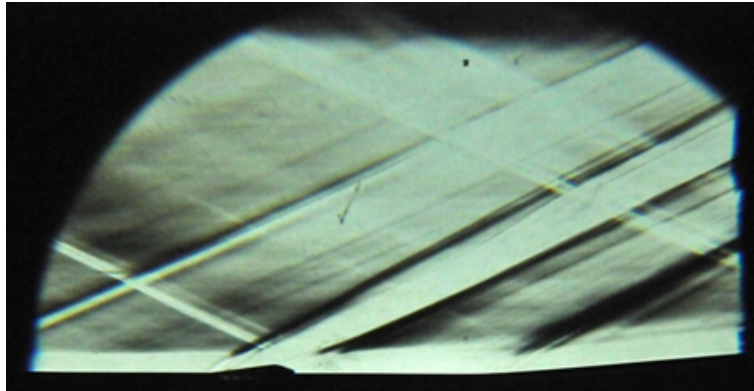


(a)

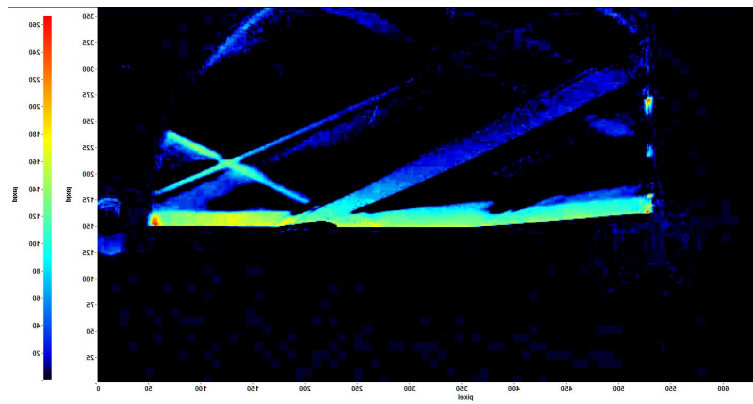


(b)

Figure A.11. *5 Deg 45 MVG* configuration for (a) Schlieren and (b) Image Subtraction.



(a)



(b)

Figure A.12. *5 Deg 70 MVG* configuration for (a) Schlieren and (b) Image Subtraction.

APPENDIX B
VALVE CONTROLLER PROGRAM

This focus of this Appendix is on the Supersonic Windtunnel Controller for the purpose of establishing a manual in which the controller written for the current study is described. This appendix is split into three sections. The first section will discuss a brief concept of the governing equation and the previous controller design and its complications. The second section will discuss in detail the setup and configuration of the redesigned windtunnel controller. The third and final section will establish operational procedures and control gains for known conditions obtained from experimental results conducted during this experimental study. The controller and its components listed in this appendix are specifically design for use with the current study utilizing the Supersonic Windtunnel at the Aerodynamic Research Center. For information regarding fundamentals of control theory and practical application methods the reader is directed to reference [20].

B.1 Previous Design

The first SSWT controller design was written using the LabVIEW 8.0 software. The method of controlling the pneumatic valve using LabVIEW software is based on a method by Fung, Y.T.[21] and the reader is referred to this paper for detailed discussion of the simulated controlled process. Only the main points will be discussed here. In his paper, Fung develops a control simulator for a supersonic windtunnel and determines that the change in valve angle is according to Eqs. B.1.

$$\frac{d\Theta(t)}{dt} = -K_p \frac{dP_o(t)}{dt} + \frac{K_p}{K_i} (P_d - P_o(t)) \quad (\text{B.1})$$

In Eqs. B.1 $dP_o(t)/dt$ represents the change in plenum chamber pressure, K_p and K_i are respected proportional and integral gains, P_d is the desired plenum chamber pressure, and $P_o(t)$ is the current plenum chamber pressure at time (t). For

practical application, the pressure data of the plenum chamber is recorded with respect to time. Eqs. B.1 is the governing equation of the windtunnel controller.

The first attempt at designing a SSWT controller program contained three major deficiencies that made it unreliable for practical application. The first deficiency is the inability for the controller to repeat the controlled process based on the same initial conditions. In many test conducted the first attempt to run the windtunnel was controlled successfully, however the second test and following test thereafter, the controller produced large pressure oscillation in the plenum chamber and was unable to control the fluctuations or maintain a constant plenum chamber pressure. Even under less severe conditions (i.e. lower plenum chamber pressure) the test conducted after the initial test produce the same results as previous situations. The initial conclusion to these results were thought to be inaccurate K_p and K_i gain settings, however after modifying the K_p and K_i gains, the oscillations in the plenum chamber continued to occur. Further investigation and testing concluded the problem was in the program design. It was discovered that when the controller was stopped after the 1st initial run, the ending values of P_1 , P_2 , and valve angle were recycled by the program and became the initial values by default. When the controller was started again, the program assumed these were the initial values and tried to compensate, thus leading to large plenum chamber oscillations. In order for the controller to work correctly, the controller had to be completely shut down and restarted.

The second deficiency in the first version was the inability to combine P_1 supply pressure readings during fill operations and P_1 supply pressure readings during SSWT control operations under one program meaning two programs were needed to be used. One program was used to monitor the supply tank pressure during fill operations and the other program was design monitor the pressure during wind tunnel operation. The problem with this configuration lies in the inability for the Data Acquisition

(DAQ) card to handle two VI programs running at the same time. If two programs run at the same time, an error message appears and all control of the valve would be lost and if the valve was opened before the error was given, it would remain open. Once the program failed, the only way to close the valve was to turn off the power supply to the valve. When power is restored to the valve, the valve would reopen to its earlier position that it was when the power was turned off. This imposed a major safety issue.

The third deficiency was the inability for the operator to shut the valve at will during controller operation. When the stop button was pressed on the controller only the control program stopped. If the valve was open during at the moment the program was stopped, the valve would remain open and air would continue to flow. The program was designed automatically closed the valve when the air supply dropped below a certain pressure. While this is sufficient for long operational times, this is inefficient for short operational times. This deficiency developed into not only a control issue, but as well safety issue. As with the second deficiency, the only means of shutting the valve during operations is to turn off power to the valve. The pneumatic valve designed such that it relies on a signal 4 - 20mA to open the valve, if no signal is present, then the valve is set to close. The safety issue arises when power is restored to the valve. In order to close the valve for the next run, the valve had to be reset using a controlled simulation. Since the valve also relied on air for control, the air supply to the valve had to be shut off before the control simulation could be conducted. These deficiencies proved that the previous controller was both inefficient and not reliable. With these key deficiencies known, it was decided that a new LabVIEW VI controller needed to be designed with certain required objectives.

Table B.1. New controller design parameters

Item	Operational Requirement
1	Controller program needs to repeat operation without closing program
2	Combine fill operations and testing into one program
3	Set practical data sampling in real time
4	Conduct safety test of maximum plenum pressure setting
5	Have the ability to stop run at will
6	Three fail safes to prevent over pressurizing the plenum chamber

B.2 New Controller Design

The LabVIEW VI Valve controller used during this experimental study is still based on the paper written by Fung, Y.T., however, the deficiencies learned from the previous design had to be reconciled in order to make the controller and thus the supersonic windtunnel more efficient, practical, and safe. To resolve these issues, operational requirements listed in Table B.1 were developed.

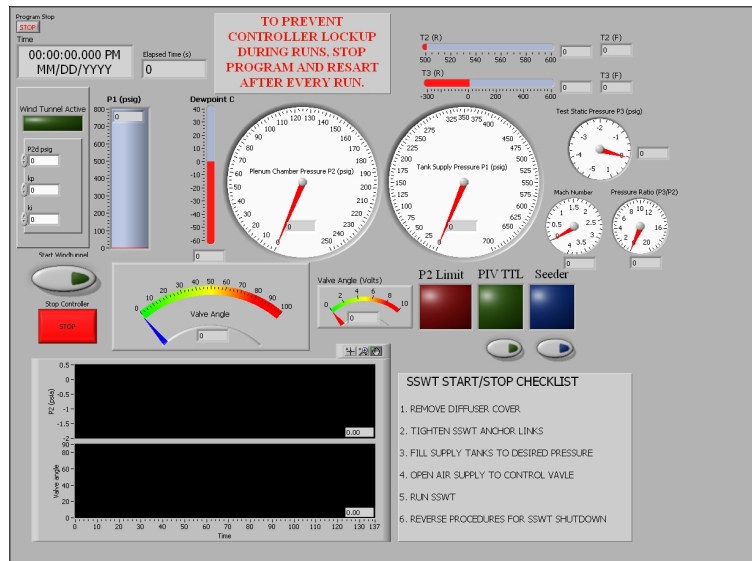
Similar to the first controller design, a simulator was built to simulate the control process and evaluate the valve's response. The simulator is also useful in acting as a tool for the operator to first modify or add on to the controller's design and test the valves reaction to the modification before it is implemented to the operating controller.

B.2.1 Controller Layout

The SSWT controller has two parts to its operation, the front panel and the block diagram. The front panel is the operational panel where the operator will operate the program seen in Fig. B.2. The block seen in Fig. B.2(a) is where the programming occurs. Each LabView program will have one front panel and one block diagram for which each are connected under one VI file. Further description of each



(a) Block diagram



(b) Front Panel

Figure B.2. Layout of current controller design. (a) Block diagram (b) Front Panel.

function of the front panel are given with its respect placement withing the block diagram.

B.2.2 Data Input

In order for the LabVIEW to process the calculations needed to control the valve angle, the data generated by the pressure transducers, the dewpoint meter, and the thermocouple must first be imported into the program. Connecting and installation of each measurement device depends on the requirements of the device itself and the reader is referred the device manual for installation and description. The signal from the measurement devices are connected through the CB-68LPR junction block seen

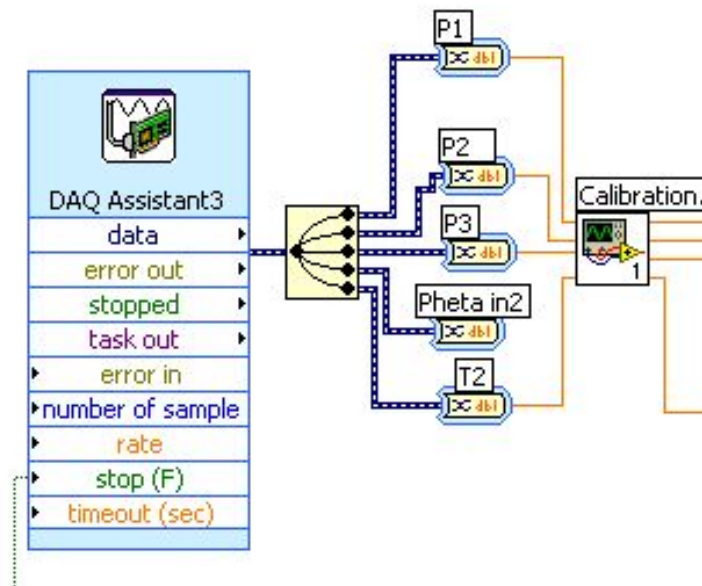


Figure B.3. Layout of DAQ assistant where signals from the measurement devices are imported into the program and divided into single data lines.

in Fig. B.4. Each connection port on the junction block represents a specific channel on the DAQ card located inside the computer. The DAQ card determines what port on the junction block represent.

The representation and activation of the channels located on the DAQ is accomplished using the Measurement and Automation manager software that is initially

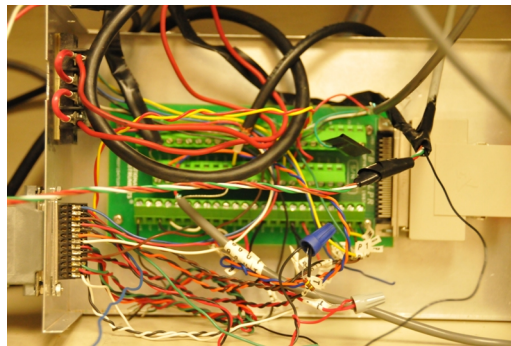


Figure B.4. CB-68LPR connector block for DAQ.

installed when the LabView software is installed on the computer. After installation, the DAQ assistant links the device channel to the program seen in Fig. B.3. Further information about the DAQ assistant and its functions can be found using the help files within the LabVIEW program. All the data collected by the DAQ assistant is brought into the program as a single dynamic data wire type. A signal splitter is used to separate the data into individual data wires. The order determining which data is represented by which wire listed in the DAQ Assistant. The individual signals are then converted from a dynamic signal to a 64-bit real data type in order to perform the necessary calculations. The data then goes into the Calibration VI where the pressure and temperature signals are converted from their original voltage signal value to their unit of measurement value based on using the equations previously discussed in Section 3. The resulting data exits the Calibration VI and is directed to other location for further processing.

B.2.3 Block Diagram Gauges and Mach Calculation

Displayed on the front panel in Fig B.2(b) several gauges displaying different types of information. These gauges are represented on the block diagram, see Fig. B.5. Starting from the left side of the figure, the data exiting the calibration VI is

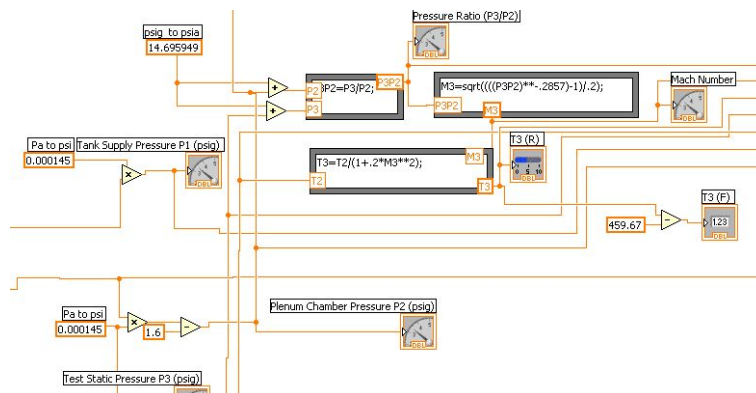


Figure B.5. Image of Mach number, Test section temperature, and gages are represented.

wired to their respected icons that represent the guages on the front panel. Some of the data is split and is used to calculat Mach number, plenum chamber pressure the test section ratio, and test section temperature. The equations used for calculating the Mach number and temperature are calculated according to Eqs.(B.2) and Eqs.(B.3). The data leaving the calculated blocks are sent to be labeled and saved.

$$\frac{P_3}{P_2} = \left(1 + \frac{\gamma - 1}{2} M^2\right)^{\frac{-\gamma}{\gamma - 1}} \tag{B.2}$$

$$T_3 = T_2 \left(\frac{P_3}{P_2}\right)^{\frac{\gamma - 1}{\gamma}} \tag{B.3}$$

B.2.4 PI Controller Equation

The governing equation for the controller is given according to Fung and is shown in Fig. B.6. Starting from the left side of the equation, the change in the angle (dtheta) is equal to the negative value of the proportional gain (kp) times the

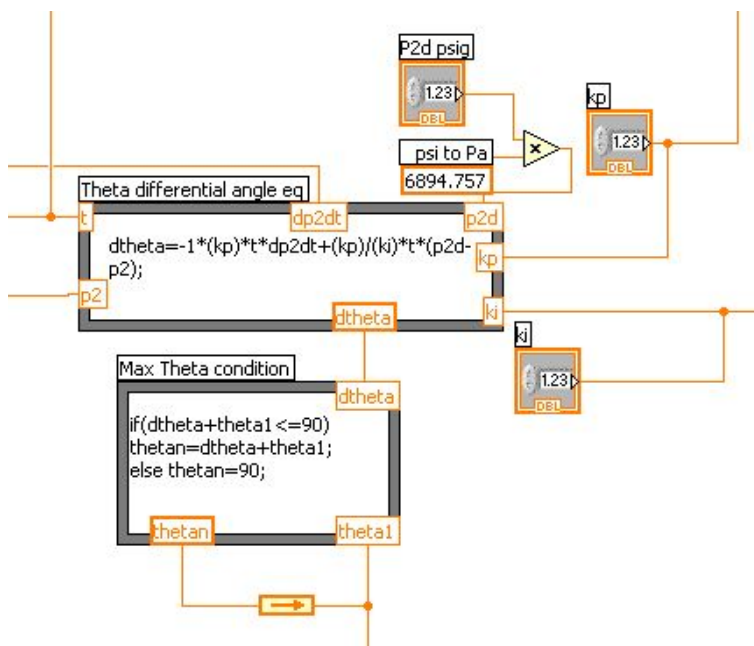


Figure B.6. PI Controller governing equation with max theta test.

sampling time (t) in Hz times the change in the plenum pressure ($dp2dt$) plus the proportional gain (kp) divided by the integral gain (ki) time the sampling time times the desired plenum pressure ($p2d$) minus the measured plenum pressure ($p2$). This is the direct representation of Eqs. B.1

Once the change in angle has been calculated the value is sent to the max theta angle condition block. Here the change in the angle is added to the previous calculated angle (θ_1) and is tested to see whether the new value is less than 90° . If the value is greater than 90° , than a value of 90 is sent. If the value is less than 90° then the new angle (θ_{new}) is split sending the signal to the valve and the other is recycled (θ_1) and used in the next calculation cycle. The arrow seen in the figure signifies that the data is looped and therefor requires an initial condition not shown in the figure. The initial condition for this loop is set to zero. The other blocks ($p2d$, kp , ki) are the controlled input values determined by the operator on the front panel as seen in Fig. B.2(b).

B.2.5 Data Labeling

Labeling the correct name and attaching said name to the data proved to be challenging during initial development of the controller program. The output file generated by the controller contained the data collected from both the windtunnel pressure transducers and the calculations performed within the program and are written in .dat format. The columns not automatically labeled by the program. The process for labeling the data is shown in Fig. B.7. As seen in the figure the data, incoming from the left, is first converted from a double 64-bit real data type to a waveform double data type. As of the current version, this was the only way known to the author to name the data before writing the file. After the data was converted, it was sent to the waveform attribute block. This block allows the user to input the desired name into the waveform. The "NI ChannelName" determines what the values

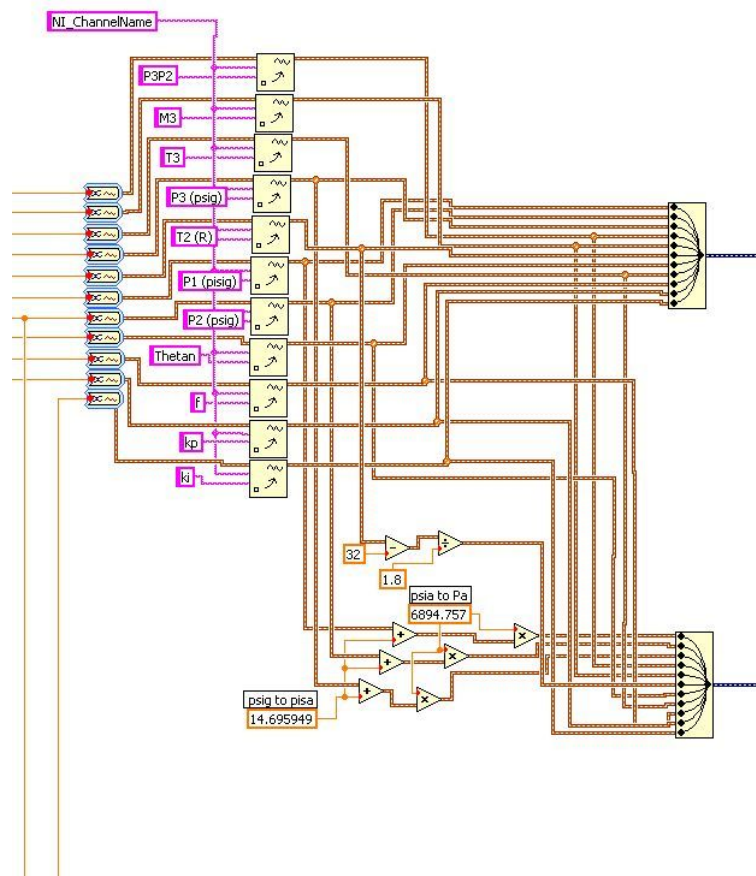


Figure B.7. Data labeling process.

name being written is (ie. P2P3, M3, T3, ect...). The waveforms are then merged back into a single data wire. The resulting wire is converted to a dynamic data type wire. From here the dynamic data is sent to a file were it is to be written and saved in a desired location on the computer. As seen in the figure, a second set of data is diverted, modified, and written in the same manner as the other set. This has been done so that the operator has the option to choose between SI or English units. This section has been developed strictly for convince. The data output file for SI will show to have English units as labeled, however, the values are expressed in SI. The user must take note of this error when viewing the SI data. A future modification may be

needed, but is not critical to the overall operation or the results of the operation of the controller.

B.2.6 Valve Signal Output

Before the calculated valve angle is sent from the program to the Rosemount 950, the signal passes through two safety features. These safety features are designed to prevent from overpressuring the plenum chamber and prevent rupturing the safety diaphragm on the plenum chamber. For the first safety feature refer to Section B.2.9. The second of two safety features is the relay switch shown in Fig. B.8. The function of the relay switch is to automatically shut off the valve when the pressure reading from the plenum chamber reaches or is above 220 psig. The relay is operated by a boolean value seen entering the left hand side in Fig. B.8 and remains connected if the statement is true. If the boolean value becomes false, the relay is disconnected and output signal from the relay becomes zero signaling the valve to close. The boolean value is determine by the first safety feature in Section B.2.9.

After leaving the relay, the signal is directed to two outputs. The first output is sent to a DAQ Assistant2 where a voltage signal is sent to the Fisher-Rosemount DPR950 Controller and the other is sent to the valve guage on the block diagram.

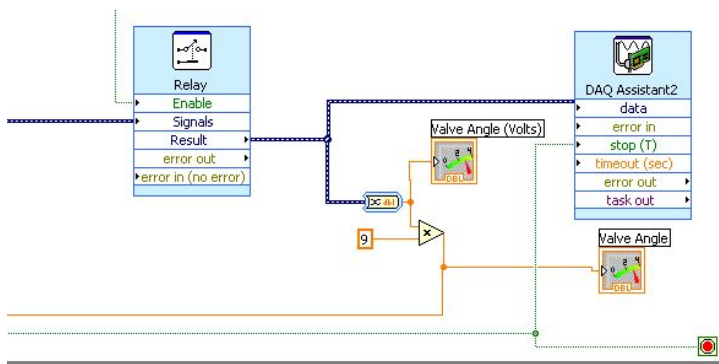


Figure B.8. Signal relay and signal output location.

The Fisher-Rosemount DPR950 controller converts the signal from a 0 - 9 voltage into a 4 - 20ma signal which is then sent to the control valve. The boolean value wired to the stop icon on the DAQ and also to the stop sign located at the bottom of the loop required by the LabVIEW software. This boolean value is also wired to the start wind tunnel controller button not shown in the figure. The second dynamic signal output leaving the relay is wired to a valve angle gauge icon in terms of volts and a valve angle gauge icon in terms of degrees. These are the gauges displayed on the front panel as shown in Fig. B.2(b).

B.2.7 Fill Operations

A true and false statement is added to the while loop controlling the program. This true and false loop gives the ability for the controller to be controlled by a boolean value to start and stop the SSWT operation. When the button is depressed operation under the true statement commence when the button is released false statement commences.

Beginning on the left side of Fig. B.9 and following the direction of the wire, the first icon is input channel description. Here the channel input refers to the channel located on the CB-68LPR junction block. The next icon creates the channel based on the physical channel itself. This is needed strictly for the programing purposes.

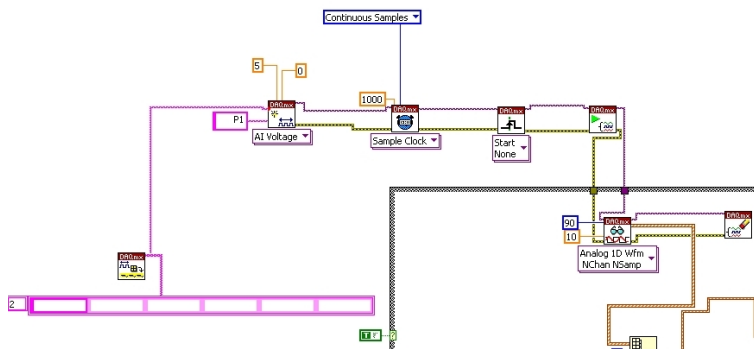


Figure B.9. P1 input for pressure taken fill operations.

The next icon is the sample rate clock which determines the sampling rate. The wire then pass through the trigger and the start task icons. The wire must then passes through a another true and false loop to the read icon where the voltage signal is read into the program. In this particular case the signal is an analog 1D Wfm. The clear task icon is the means for LabVIEW to clear the task after it has been read. Like the dynamic signal with the DAQ assistant the data is split and read.

For this particular section, the data passes through a similar calibration VI and converts the voltage to the desired value. The measurements are then connected to their respected gauge which are displayed on the front panel. This is the reason there are two guages for the P_1 air supply. Finally only the dewpoint data is is recorded and stored in the same manner as described in Section B.2.5.

B.2.8 Controller Reset

As mentioned previously, the previous controller was unable to reset the P_1 and P_2 values which in turned cause the controller to use the ending values on the previous run as the initial conditions for the second run. This made the controller unstable.

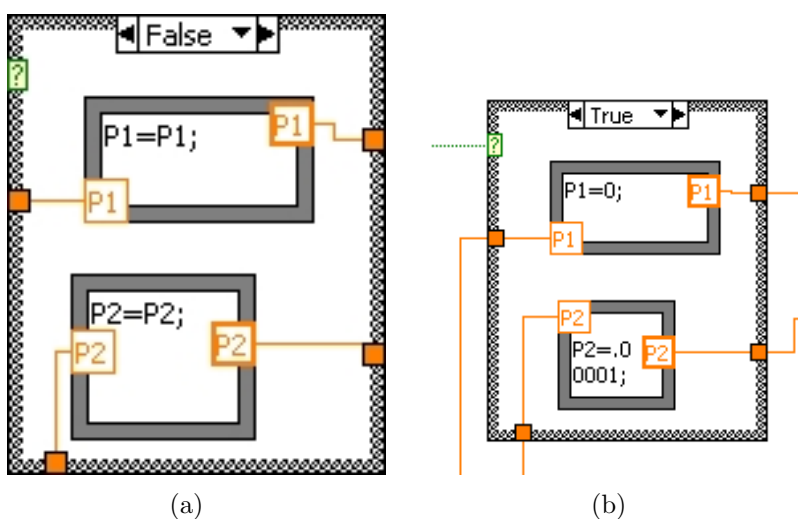


Figure B.10. Control statement designed to reset P_1 and P_2 values to zero.

The solution for this problem is shown in Fig. B.10. Here a true and false loop is drawn for which boolean value determines which statement is to be expressed. The P_1 and P_2 values come directly from the calibration VI shown in Fig. B.3. If the boolean value is false, the values of P_1 and P_2 do not change and are passed on through the loop, shown in Fig. B.10(a). This condition occurs when the controller is in operation. The true statement, Fig. B.10(b) occurs when the value of the boolean becomes true. This condition will occur when the controller is commanded to close the valve either manually or by the one of two safety triggers. For P_2 the value cannot be zero else the controller will automatically shut off due to the safety condition expressed by section B.2.9. The small value of P_2 does not effect the controllers performance.

The boolean value attached to the true and false loop in the figure is connected to a boolean zero test statement not shown in the figure. This zero statement determined by the relay switch shown in Fig. B.8 in Section B.2.6

B.2.9 P_2 Limit

The first of two safety features developed for the valve controller monitors the readings in the plenum chamber pressure and overrides the valve signal if the pressure reaches a desired maximum value. This is process is shown as seen in Fig. B.12.

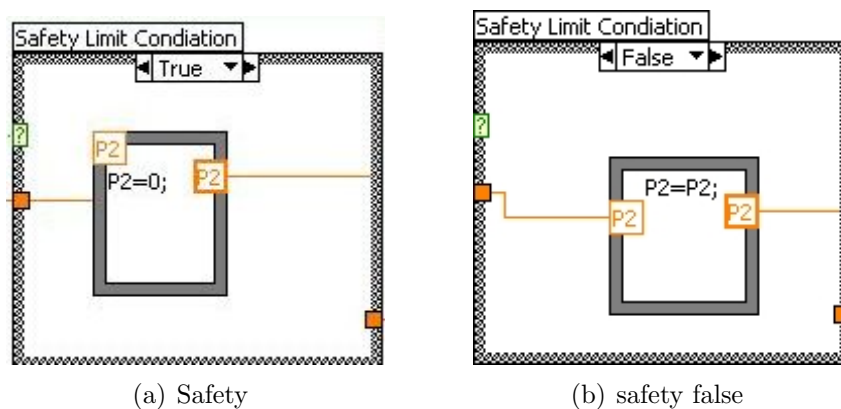


Figure B.11. Control statement for max P_2 detection.

as it is originally designed to do. When the measured pressure dropped below the max value, the condition would reverse itself and the controller would tell the valve to open. The (or) statement prevents this situation from occurring. In order for a false statement to exist, both inputs in the (or) statement must be false. When the true statement has been sent, the resulting zero signal will remain until the initial condition is activated. To activate the initial condition, the controller program must be stopped and restarted. A light indicator is place to inform the operator that the safety feature has been activated and that the controller must be reset inorder to function.

The maximum allowable pressure in the plenum chamber is 1.55 MPa (225 psig). If the pressure becomes greater than 1.55 MPa (225 psig), the safety diaphragm on the plenum chamber will rupture. Spare diaphragms are currently located in the SSWT cabinet located underneath the stairs in Rm 109. Because the rupture pressure is set for 1.55 MPa (225 psig), the max pressure on the controller is set to 1.51 MPa (220 psig). The green arrow in Fig. B.11 indicates that the value is in a loop and must have an initial condition. The initial condition is set to false. The value of the zero condition test is also sent to the relay switch located in Fig. B.8.

B.3 SSWT Operational Procedures

Upon completing the development of and testing of the Super Sonic Wind Tunnel controller, a step by step instructional procedure was developed the controller and wind tunnel operation. The following steps should be undertaken before operating the SSWT on the first run of each day.

SSWT Controller Calibration Procedures

1. Ensure the air supply to the pneumatic control valve is in the closed position and blue gate valve that feeds air to the plenum chamber with air is closed.

2. Turn on 175 psig compressor and turn on SSWT controller computer.
3. Turn on the power switch that powers the Rosemount 950 and transducers.
4. Plug in valvelink modem and start valvelink software and controller simulator.
5. Once the valvelink software has started, click the satellite icon and press start.
The program is now monitoring the valve response.
6. Right click the valve icon and select trend. A graph should appear which will show the valve data in real time.
7. Input desired settings into the controller simulator and turn the air supply to the pneumatic valve to the open position. Example: $p1 = 150\text{psig}$, $p2 = 50\text{psig}$, $p2max = 60\text{psig}$, $kp = .00012$, $ki = 50$
8. Press the hand button on the Rosemount Controller to place it in tacking mode.
9. Perform valve operation test. Listen to reaction of the valve while monitoring the valvelink software and determine if the valve oscillates during test. If the valve oscillates, calibration is required. Perform calibration using the valvlink software. If calibration is not required, proceed to step 16 for SSWT operation.
10. On the left hand side right click on the valve and select "Instrument mode" to set the instrument to "out of service".
11. Under the calibration tab, select "auto travel". This will automatically calibrate the valve.
12. After valve has been calibrated, select "step test".
13. Using the conditions from the previous test, perform step test.
14. After test has been performed, compare the two results. The red line is the valve response and the blue line is the valve signal. If the valve response is inline with the valve signal, the valve is calibrated. Note: some oscillations can be tolerated, but only in the down stroke.
15. Once calibrated, set the valve back to operational mode ramp condition.

16. Repeat step 9 and test the valve with the controller to ensure the valve will operate as desired. If the valve operates as desired, exit the valvelink software and disconnect the USB modem from valve connectors.
17. Exit the SSWT controller simulator and open the SSWT Controller.
18. Press the hand button on the Rousemount controller to remove it from tracking mode.
19. Close the air supply to the control valve.

SSWT Wind Tunnel Operating Procedures

1. Ensure that the air supply to the control valve is in the off position and the blue supply gate valve close.
2. Secure the Wind tunnel by tightening the three anchor links.
3. Turn on the power supply to the Rosemount controller and open the wind tunnel controller program.
4. If valve has not been calibrated, perform calibration procedures, if already calibrated, proceed to the next step.
5. Open the gate valve that supplies the SSWT tank with air from the 2000 psig compressor and fill tanks to desired pressure.
6. Open the gate valve on the SSWT that feeds air to the plenum chamber.
7. Turn on laser safety light, lock doors to Rm 109, and hang the "Danger Test in Progress" sign on the exit door of Rm 109.
8. Recheck anchor links and test equipment for readiness.
9. For safety reasons only the controller operator will perform steps 9 thru 14. Arm the wind tunnel by SLOWLY opening the air supply to the control valve.
10. Press the hand icon on the Rousemount controller to place it in tracking mode.
11. Set the desire plenum chamber pressure value, k_p , and k_i values into the program. Press the program start button to start the program.
12. Press the green start button the controller program to operate windtunnel. The operator must monitor the plenum chamber pressure to ensure proper operation.
13. Upon completion of the test, stop the controller and press the hand icon on the Rousemount controller to place the system off tracking mode.
14. Immediately turn off the air supply to the control valve. The windtunnel is now disarmed.
15. If more test are needed, repeat 9–14, else proceed to the next step.

16. Close the blue gate valve that feeds air to the plenum chamber.
17. Loosen the anchor links to allow windtunnel to flex during hot and cold temperatures.
18. Close the the gate valve that supplies the wind tunnel air from the compressor tanks.

It is necessary to perform the Calibration procedures and SSWT Operational Procedures to ensure proper functioning of the equipment and prevent any unnecessary failures from occurring. If the emergency arises to which the valve needs to be shut off immediately and/or the program becomes inoperable, turning off power to the Rosemount controller will cause the valve to close. Before restoring power to the valve, ensure that the blue gate valve that supplies air to the plenum chamber is close. Once power is restored to the Rosemount controller, the valve will open to it position when the power was terminated.

REFERENCES

- [1] Q. Li and C. Liu, “LES for Supersonic Ramp Control Flow Using MVG at M=2,” in *48th AIAA Aerospace Sciences Meeting*, Orlando, Florida, 2010.
- [2] S. Morris, “Boeing 777-236/ER,” Gatwick, London, p. Airlines.net, 2006. [Online]. Available: <http://www.airliners.net/photo/British-Airways/Boeing-777-236-ER/1091105/&sid=27e72c33d5b82e2adb78a232662bd3f8>
- [3] H. Holden and H. Babinsky, “Effect of Microvortex Generators on Separated Normal Shock/Boundary Layer Interactions,” *Journal of Aircraft*, vol. 44, no. 1, pp. 170–174, 2007.
- [4] LaVision, “DaVis FlowMaster Software Manual for DaVis 7.1,” Ypsilanti, MI, 2006.
- [5] Merriam-Webster, “Vortex - Definition and More from the Free Merriam-Webster Dictionary.” [Online]. Available: <http://www.merriam-webster.com/dictionary/vortex>
- [6] H. Schlichting and K. Gersten, *Boundary-Layer Theory*, 8th ed. Springer, 2000.
- [7] J. Dussauge, H. Fernholz, R. Smith, P. J. Finley, A. Smits, and E. Spina, *Turbulent Boundary Layers in Subsonic and Supersonic Flow*, W. Saric, Ed. Neuilly-Sur-Seine, France: AGARD, 1996.
- [8] D. G. Mabey, “Experimental Studies of the Boundary Layer on a Flat Plate at Mach Numbers from 2 . 5 to 4 . 5,” R.A.E., Bedford, 1976.
- [9] A. Valdivia, K. B. Yuceil, J. L. Wagner, N. T. Clemens, D. S. Dolling, and R. Number, “Active Control of Supersonic Inlet Unstart Using Vortex Generator

- Jets,” in *39th AIAA Fluid Dynamics Conference*, no. June. San Antonio, Texas: AIAA, 2009, pp. 1–14.
- [10] J. Matsumoto, “Design and Testing of a Subscale Supersonic Aeropropulsion Wind Tunnel,” Ph.D. dissertation, University of Texas at Arlington, 2000.
- [11] E. M. Braun, F. K. Lu, P. K. Panicker, R. R. Mitchell, D. R. Wilson, and J. C. Dutton, “Supersonic Blowdown Wind Tunnel Control Using LabVIEW,” in *46th AIAA Aerospace Sciences Meeting and Exhibit*, no. January, Reno, Nevada, 2008, pp. 1–14.
- [12] A. J. Pierce, F. K. Lu, D. S. Bryant, and Y. Shih, “New Developments in Surface Oil Flow Visualization,” in *27th AIAA Aerodynamic Measurement Technology and Ground Testing Conference*, no. July, Chicago, Illinois, 2010, pp. 1–11.
- [13] G. Tedeschi, H. Gouin, and M. Elena, “Motion of tracer particles in supersonic flows,” *Experiments in Fluids*, vol. 26, pp. 288–296, 1999.
- [14] F. Scarano, *Overview of PIV in Supersonic Flow*. Dordrecht: Springer, 2008, pp. 445–463.
- [15] M. F. Reeder, J. W. Crafton, J. Estevadeordal, J. DeLapp, C. McNiel, D. Peltier, and T. Reynolds, “Clean seeding for flow visualization and velocimetry measurements,” *Experiments in Fluids*, vol. 48, no. 5, pp. 889–900, Nov. 2009. [Online]. Available: <http://www.springerlink.com/index/10.1007/s00348-009-0784-5>
- [16] “DDBST: Saturated Vapor Pressure,” 2010. [Online]. Available: http://www.ddbst.com/en/online/Online_Calc_vap_Form.php
- [17] F. White, *Viscous Fluid Flow*, 3rd ed. McGraw-Hill Science/Engineering/Math, 2005.
- [18] G. S. Settles, *Schleiren and Shadowgraph Techniques*, corrected ed. Springer, 2001.

- [19] B. Anderson, J. Tinapple, and L. Surber, "Optimal Control of Shock Wave Turbulent Boundary Layer Interactions Using Micro-Array Actuation," in *3rd AIAA Flow Control Conference*, San Francisco, California, 2006.
- [20] D. Cooper, A. Houtz, and B. Rice, "Practical Process Control." [Online]. Available: <http://www.controlguru.com/>
- [21] Y. Fung and G. S. Settles, "Microprocessor Control of High Speed Wind Tunnel Stagnation Pressure," in *AIAA Aerodynamic Testing Conference*, San Diego, California, 1988.
- [22] D. Coles, "Measurements in the Boundary Layer on a Smooth Flat Plate In Supersonic Flow," Ph.D. dissertation, California Institute of Technology, 1953.
- [23] R. K. V. D. Draai, R. V. Schinkel, and A. Telesca, "Application of PIV in (local) Supersonic Flows in DNW Wind tunnels," in *41st AIAA/ASME/SAE/ASEE Joint Propulsion Conference and Exhibit*, no. July, Tucson, Arizona, 2005, pp. 1–13.
- [24] G. C. Herring and M. E. Hillard, "Flow Visualization by Elastic Light Scattering in the Boundary Layer of a Supersonic Flow," Hampton, VA, p. 24, 2000.
- [25] R. A. Humble, F. Scarano, and B. W. V. Oudheusden, "Experimental Study of an Incident Shock Wave/Turbulent Boundary Layer Interaction Using PIV," in *36th AIAA Fluid Dynamics Conference and Exhibit*, no. June, San Francisco, California, 2006, pp. 1–16.
- [26] C. Horsman and F. Owen, "Turbulent Properties of a Compressible Boundary Layer," *AIAA Journal*, vol. 10, no. 11, pp. 1418–1424, 1972.
- [27] LaVision, "DaVis FlowMaster Software," Ypsilanti, MI, p. 184, 2005.
- [28] S. Lee, E. Loth, N. J. Georgiadis, and J. R. Debonis, "Effect of Mach number on Flow Past Micro-Ramps," in *39th AIAA Fluid Dynamics Conference*, no. June. San Antonio, Texas: American Institute of Aeronautics and Astronautics, 2009.

- [29] D. Mathews and M. Childs, “Use of Coles’ Universal Wake Function for Compressible Turbulent Boundary Layers,” *Journal of Aircraft*, vol. 7, no. 2, pp. 137–140, 1970.
- [30] A. Melling, “Tracer particles and seeding for particle image velocimetry,” *Measurements of Science and Technology*, vol. 8, pp. 1406–1416, 1997.
- [31] P. Ford, C.w, and H. Babinsky, “Micro-Ramp Control for Oblique Shock Wave/Boundary Layer Interactions,” in *37th AIAA Fluid Dynamics Conference and Exhibit*, Miami,Fl, 2007, pp. 1–14.
- [32] E. K. Lu and G. S. Settles, “Color surface-flow visualization of fin-generated shock wave boundary-layer interactions,” *Experiments in Fluids*, vol. 8, no. 1990, pp. 352–354, 1990.
- [33] V. Mosharov, A. Orlov, and V. Radchenko, “New Approach to Surface Oil-Flow Visualization,” Zhukovsky, Russia, pp. 176–180.
- [34] S. Depardon, J. Lasserre, J. Boueilh, L. Brizzi, and J. Boree, “Skin friction pattern analysis using near-wall PIV,” *Experiments in Fluids*, vol. 39, pp. 805–818, 2005.
- [35] Y. Ikeda, N. Kuratani, T. Nakajima, S. Tomioka, and T. Mitani, “M2.5 Supersonic PIV Measurement in Step-back Flow with the Normal Injection,” in *40th Aerospace Sciences Meeting and Exhibit*, no. January, Reno,Nevada, 2002.
- [36] H. A. Holden and H. Babinsky, “Vortex Generators Near Shock / Boundary Layer Interactions,” in *42nd AIAA Aerospace Science Meeting and Exhibit*, no. January, Reno,Nevada, 2004.
- [37] Y. X. Hou, N. T. Clemens, and D. S. Dolling, “Development of a Multi-Camera PIV Imaging System for Studies of Shock / Boundary Layer Interactions,” in *22nd AIAA Aerodynamic Measurement Technology and Ground Testing Conference*, no. June, St. Louis, Missouri, 2002.

- [38] P. L. Blinde, R. A. Humble, B. W. V. Oudheusden, and F. Scarano, “Effects of micro-ramps on a shock wave / turbulent boundary layer interaction,” *Shock Waves*, no. 19, pp. 507–520, 2009.
- [39] M. C. Galbraith, P. D. Orkwis, J. A. Benek, E. Mechanics, A. V. Directorate, A. Force, and W. Patterson, “Multi-Row Micro-Ramp Actuators for Shock Wave Boundary-Layer Interaction Control,” in *47th AIAA Aerospace Science Meeting*, no. January, Orlando, Florida, 2009, pp. 1–30.
- [40] R. D. Keane and R. J. Adrian, “Optimization of particle image velocimeters . Part I : Double pulsed systems,” *Measurements of Science and Technology*, pp. 1202–1215, 1990.
- [41] M. Casper, C. Kahler, and R. Radespiel, “Generator Jet Arrays,” in *4th Flow Control Congerence*, no. June, Seattle, Washington, 2008, pp. 1–11.
- [42] A. Z. Shahneh and F. Motallebi, “Effect of Submerged Vortex Generators on Shock-Induced Separation in Transonic Flow,” *Journal of Aircraft*, vol. 46, no. 3, pp. 856–863, 2009.
- [43] J. Haertig, M. Havermann, C. Rey, and A. George, “Particle Image Velocimetry in Mach 3.5 and 4.5 Shock-Tunnel Flows,” *AIAA Journal*, vol. 40, no. 6, pp. 1056–1060, 2002.
- [44] T. Herges, E. Kroeker, G. Elliott, and C. Dutton, “Micro-Ramp Flow Control of Normal Shock/Boundary Layer Interactions,” in *47th AIAA Aerospace Science Meeting*, no. January, Orlando, Florida, 2009, pp. 1–22.
- [45] H. Babinsky, N. J. Makinson, and C. E. Morgan, “Micro-Vortex Generator Flow Control for Supersonic Engine Inlets,” in *45th AIAA Aerospace Sciences Meeting and Exhibit*, no. January, Reno, Nevada, 2007, pp. 1–8.
- [46] O. Lögberg, J. H. M. Fransson, and P. H. Alfredsson, “Streamwise evolution of longitudinal vortices in a turbulent boundary layer,” *Journal*

- of *Fluid Mechanics*, vol. 623, pp. 27–58, Mar. 2009. [Online]. Available: http://www.journals.cambridge.org/abstract_S0022112008004825
- [47] Q. Li and C. Liu, “Numerical Investigations on the Effects of the Declining Angle of the Trailing-Edge of MVG,” in *48th AIAA Aerospace Sciences Meeting*, no. January, Orlando, Florida, 2010, pp. 1–14.
- [48] H. Moet, F. Laporte, G. Chevalier, and T. Poinso, “Wave propagation in vortices and vortex bursting,” *Physics of Fluids*, vol. 17, no. 5, 2005. [Online]. Available: <http://link.aip.org/link/PHFLE6/v17/i5/p054109/s1&Agg=doi>
- [49] C.-C. Sun and M. E. Childs, “A modified wall wake velocity profile for turbulent compressible boundary layers.” *Journal of Aircraft*, vol. 10, no. 6, pp. 381–383, June 1973. [Online]. Available: <http://doi.aiaa.org/10.2514/3.44376>
- [50] L. Jacquin, “On trailing vortices: A short review,” *International Journal of Heat and Fluid Flow*, vol. 26, no. 6, pp. 843–854, Dec. 2005. [Online]. Available: <http://linkinghub.elsevier.com/retrieve/pii/S0142727X0500086X>
- [51] C.-C. Sun and M. E. Childs, “Wall-Wake Velocity Profile for Compressible Nonadiabatic Flows,” *AIAA Journal*, vol. 14, no. 6, pp. 820–822, 1976.
- [52] J. Lin, “Review of research on low-profile vortex generators to control boundary-layer separation,” *Progress in Aerospace Sciences*, vol. 38, no. 4-5, pp. 389–420, May 2002. [Online]. Available: <http://linkinghub.elsevier.com/retrieve/pii/S0376042102000106>
- [53] W. Rose, “The Behavior of a Compressible Turbulent Boundary Layer In A Shock-Wave-Induced Adverse Pressure Gradient,” Moffett Field, California, pp. 1–236, 1973.
- [54] R. a. Humble, F. Scarano, and B. W. Oudheusden, “Particle image velocimetry measurements of a shock wave/turbulent boundary layer interaction,”

- Experiments in Fluids*, vol. 43, no. 2-3, pp. 173–183, June 2007. [Online]. Available: <http://www.springerlink.com/index/10.1007/s00348-007-0337-8>
- [55] J. M. Osterlund and A. V. Johansson, “Measurements in a Flat Plate Turbulent Boundary Layer,” Stockholm, Sweden, pp. 2–7, 1998.
- [56] P. Bradshaw and G. P. Huang, “The Law of the Wall in Turbulent Flow,” *Proceedings of the Royal Society A: Mathematical, Physical and Engineering Sciences*, vol. 451, no. 1941, pp. 165–188, Oct. 1995. [Online]. Available: <http://rspa.royalsocietypublishing.org/cgi/doi/10.1098/rspa.1995.0122>
- [57] D. a. Dickmann and F. K. Lu, “Shock/Boundary-Layer Interaction Effects on Transverse Jets in Crossflow over a Flat Plate,” *Journal of Spacecraft and Rockets*, vol. 46, no. 6, pp. 1132–1141, Nov. 2009. [Online]. Available: <http://doi.aiaa.org/10.2514/1.39297>
- [58] A. Jirasek, “Vortex-Generator Model and Its Application to Flow Control,” *Journal of Aircraft*, vol. 42, no. 6, pp. 1486–1491, Nov. 2005. [Online]. Available: <http://doi.aiaa.org/10.2514/1.12220>
- [59] D. Coles, “The law of the wake in the turbulent boundary layer,” *Journal of Fluid Mechanics*, vol. 1, no. 02, p. 191, Mar. 2006. [Online]. Available: http://www.journals.cambridge.org/abstract_S0022112056000135
- [60] R. Örlü, J. H. Fransson, and P. Henrik Alfredsson, “On near wall measurements of wall bounded flows The necessity of an accurate determination of the wall position,” *Progress in Aerospace Sciences*, vol. 46, no. 8, pp. 353–387, Nov. 2010. [Online]. Available: <http://linkinghub.elsevier.com/retrieve/pii/S0376042110000370>
- [61] J. K. Watterson, M. Leslie, W. McEwan, E. Benard, and J. Cole, “Influence of Sub-Boundary Layer Vortex Generators on Wall Shear Stress,” in *Fluid Dynamics Conference and Exhibit*, no. June, Toronto, Ontario Canada, 2005, pp. 1–8.

BIOGRAPHICAL STATEMENT

Adam J. Pierce was born in Garland, Texas in 1977. After graduating from Irving High School in Irving, Texas in 1996 he enlisted in the United States Marine Corps and served with the 1st Battalion 4th Marine Regiment and 2nd Battalion 5th Marine Regiment until August 2000. Withdrawing from honorable active service he enrolled in college in January 2001 and received his B.S. degree in Aerospace Engineering from the University of Texas at Arlington in Fall of 2007. From there he continued on for his M.S. Degree in Aerospace Engineering. He has worked at the Aerodynamics Research Center since 2005 and has been involved in numerous projects including explosive detection portal, schlieren imagery, pulse detonation engine, and micro-vortex generators for which is the topic of this thesis.